REPORT DOCUMENTATION PAGE

Public reporting burden for this collection of information is estimated to average 1 hour per response, including the time for reviewing ir data needed, and completing and reviewing this collection of information. Send comments regarding this burden estimate or any other this burden to Department of Defense, Washington Headquarters Services, Directorate for Information Operations and Reports (0704-0 4302. Respondents should be aware that notwithstanding any other provision of law, no person shall be subject to any penalty for failing to comply with a collection of information if it does not display a currently valid OMB control number. **PLEASE DO NOT RETURN YOUR FORM TO THE ABOVE ADDRESS.**

1. REPORT DATE *(DD-MM-YYYY)* 14-06-2006	2. REPORT TYPE Final Performance Report	3. DATES COVERED *(From - To)* 15-07-2002 – 14-03-2006

4. TITLE AND SUBTITLE	5a. CONTRACT NUMBER
Optoelectronic Devices Based on Novel Semiconductor Structures	
	5b. GRANT NUMBER F49620-02-1-0352
	5c. PROGRAM ELEMENT NUMBER

6. AUTHOR(S)	5d. PROJECT NUMBER
Yujie J. Ding	
	5e. TASK NUMBER
	5f. WORK UNIT NUMBER

7. PERFORMING ORGANIZATION NAME(S) AND ADDRESS(ES)	8. PERFORMING ORGANIZATION REPORT NUMBER
Lehigh University 27 Memorial Drive West Bethlehem, PA 18015	

9. SPONSORING / MONITORING AGENCY NAME(S) AND ADDRESS(ES)	10. SPONSOR/MONITOR'S ACRONYM(S)
Air Force Office of Scientific Research Directorate of Physics and Electronics 875 North Randolph Street Suite 325 Arlington, VA 22203-1768	AFOSR/NE
	11. SPONSOR/MONITOR'S REPORT NUMBER(S)

12. DISTRIBUTION / AVAILABILITY STATEMENT
Use AFOSR-mandated availability statements. There is neither additional limitation/restriction nor special marking indicated.

Distribution Statement A: unlimited

13. SUPPLEMENTARY NOTES
None

14. ABSTRACT

During the funding period (July 15, 2002 – March 14, 2006, i.e. the total of 44 months including 36 months plus 8 months for no-cost extension), we had made great progress on a series of the research projects in order to achieve the objectives set for this grant, i.e. investigations of nanostructures and nanodevices based on novel structures and efficient THz generation and detection based on novel schemes. In this report, we have highlighted our accomplishments made on these projects. All the new results obtained under the support of this grant have made significant contributions to the long-term mission of the U.S. Air Force.

15. SUBJECT TERMS
Terahertz devices, spectrometers, and systems; nanostructures and nanodevices

16. SECURITY CLASSIFICATION OF:			17. LIMITATION OF ABSTRACT	18. NUMBER OF PAGES	19a. NAME OF RESPONSIBLE PERSON Yujie J. Ding
a. REPORT UNCLASSIFIED	b. ABSTRACT UNCLASSIFIED	c. THIS PAGE UNCLASSIFIED	SAR	84	19b. TELEPHONE NUMBER *(include area code)* (610) 758-4582

Standard Form 298 (Rev. 8-98)
Prescribed by ANSI Std. Z39.18

20060727326

**Final Performance Report on
AFOSR Grant F49620-02-1-0352**

Optoelectronic Devices Based on Novel Semiconductor Structures

Period of July 15, 2002 – March 14, 2006

Program Manager: Dr. Gernot S. Pomrenke

Principal Investigator: Dr. Yujie J. Ding

Professor of Electrical Engineering

Department of Electrical and Computer Engineering
Lehigh University
19 Memorial Drive West
Bethlehem, PA 18015

Phone: (610) 758-4582

Fax: (610) 758-6279

Email: yud2@lehigh.edu

June 14, 2006

Status of effort

During the funding period (July 15, 2002 – March 14, 2006, i.e. the total of 44 months including 36 months plus 8 months for no-cost extension), we have made great progress on a series of the research projects in order to achieve the objectives set for this grant, i.e. investigations of nanostructures and nanodevices based on novel structures and efficient THz generation and detection based on novel schemes. In the following, we have tabulated our accomplishments made within such a period:

1. Efficient generation of widely-tunable THz waves based on difference-frequency generation in GaSe
2. Design, growth, and characterization of quantum-well dots.
3. Phonon-assisted up-transfer of electrons in GaAs/AlAs superlattices
4. TEM study and band-filling effects in quantum-well dots
5. Improvements on tuning ranges and output powers for widely-tunable THz sources based on difference-frequency generation in GaSe
6. Observation of THz generation in $ZnGeP_2$
7. Measurement of absorption spectrum for air in THz
8. Design, fabrication, and characterization of photonic bandgap crystals in THz.
9. First observation of backward-propagating THz waves
10. Efficient generation of THz waves in a cubic crystal
11. Optimization, fabrication, and characterization of THz Bragg reflectors
12. Measurement of spectrum of two-photon absorption for $ZnGeP_2$
13. Observation of stimulated emission in short-period quasi-indirect type-II GaAs/AlAs superlattices
14. Evidence on coupling between InAs quantum dots and strained InGaAs/GaAs coupled quantum wells.
15. First observation of parametric upconversion
16. Efficient generation of quasi-single-cycle THz pulses
17. Improvement of tuning range and output powers for the efficient generation of backward THz waves
18. Observation of anomalously large band-filling effects in InAs/GaSb type-II superlattices
19. Introduction of a novel approach to UV emitters
20. Widely-tunable monochromatic THz waves using a 47-mm GaSe crystal.
21. Dramatically improved detection limit for upconversion detection system
22. Investigated carrier dynamics for dot-in-well structure using novel pump-probe PL technique
23. Observed peculiar behavior on PL vs. pump intensity for InAs/GaSb type-II superlattices (evidenced laser-induced cooling of superlattices).

All the new results obtained under the support of this grant have made significant contributions to the long-term mission of the U.S. Air Force. THz waves can be used to identify toxic chemicals and to obtain images of objects, and to study DNA's. Being able to achieve the efficient THz output in a cubic crystal is very important for the implementation of a THz spectrometer which covers a wide range. This is due to the fact for a cubic crystal rotation is no longer required. Our results on the optimization of the Bragg reflectors make us one step closer to the possible utilization of these unique structures in cavity mirrors and filter arrays for chemical sensors as well as to enhance the sensitivity for chemical-sensor arrays. Therefore, the

miniaturization of our THz sources, detectors, and spectrometers would be feasible. Using the world-record-long GaSe crystal the output wavelengths have already been extended to the microwave and millimeter region. Furthermore, the tuning range, peak output powers, and conversion efficiency achieved by us so far represent the widest and highest values using the tabletop pump lasers commercially available.

Our theory on the efficient generation of quasi-single-cycle THz pulses will play a very important role in scaling up the peak powers for the THz pulses (see our reports on the new AFOSR grant). Our observation of the backward THz waves can be a gateway to the backward parametric oscillation which has several advantages compared with the forward counterpart. After improving the tuning range and peak powers of the backward THz waves, we have shown that a few configurations for the backward THz parametric oscillation can be implemented. Our measurement of the spectrum of two-photon absorption is essential to our understanding of the fundamental limit to the output powers of the THz sources by using a $ZnGeP_2$ crystal.

Our observation of the parametric upconversion can lead to the development of a very efficient THz detector working at room temperature.

Quantum-well dots are demonstrated to have greatly-improved optical properties, and therefore, they can be modified as efficient THz emitters and detectors as well as other device functions. Our observation of stimulated emission represents an early demonstration on how to manipulate type-II nanostructures for more efficient amplification of light. Based on our study on the coupling between the quantum dots (0 D) and coupled quantum wells (2 D) we have gained much deeper understanding of the strains created between the 0 D and 2 D nanostructures. Our results on the InAs/GaSb type-II superlattices have re-defined the linear response range for mid-IR detectors and output powers for the mid-IR emitters.

Our initial results on the UV generation can be used as a guide for optimizing the multilayer structure producing the efficient UV light which has important applications in the detections of bioagents and lighting.

Accomplishments/New Findings

In the separate sections below, we highlight our accomplishments made on these projects (#1-20):

1. An efficient, tunable, and coherent 0.18–5.27 THz source based on GaSe crystal

THz waves, in the frequency range of 0.1–10 THz with the corresponding wavelength range of 30–3000 μm, fill the gap between the microwave and infrared bands. During the past decade, THz pulses, generated by subpicosecond laser pulses based on photoconduction and optical rectification with a broad bandwidth, have found many applications, such as THz imaging, THz spectroscopy for studies of carrier dynamics and intermolecular dynamics in liquids, and dielectric responses of molecules, polymers and semiconductors [1-7].

On the other hand, a tunable and coherent THz source is one of the key elements for applications such as chemical identification, biomedical diagnostics, and THz spectroscopy [7,8]. For example, THz-probing technology exhibits a unique potential for the label-free detection of DNA binding state [8]. Furthermore, it has most recently been demonstrated that CW THz waves can be used to detect cancer. To realize these important applications and therefore to create a new era for THz science and technology, compact, efficient and coherent THz source is essential. However, so far there has been no hope for such a source that has wide tunability in the wavelength range of 30–3000 μm except for the costly free-electron lasers (FEL) [7]. Ideally, new-generation THz sources should be compact, broadly tunable, simply aligned, and stable in terms of output. CW THz radiation generated by utilizing optical-heterodyne (photo) mixing technique faces an unbreakable barrier of a low output power (~ μW) [9,10]. Another technique is based on nonlinear difference-frequency mixing in nonlinear optical (NLO) crystals [11]. For example, 4-dimethylamino-N-methyl-4-stilbazolium-tosylate (DAST) was recently used to generate coherent THz waves tunable from 120 to 160 μm, however with the highest output energy of only 52 fJ/pulse (average power of 52 pW) through difference-frequency generation (DFG) [12]. A THz optical parametric oscillator (OPO) was recently investigated by using LiNbO₃ [13]. However, large absorption coefficients of LiNbO₃ and DAST in the THz domain result in the low efficiencies and limited tunability [12,13]. Coherent THz emission based on intersubband transitions has not yet been implemented [14-16].

In our recent study on coherent THz radiation, among the many NLO crystals such as LiNbO₃, LiTaO₃, ZnGeP₂, GaSe, DAST, CdSe, GaP, and GaAs, we have shown that GaSe has the lowest absorption coefficients in the THz wavelength region [17-19]. Such a low absorption coefficient is extremely important for the coherent THz generation since the overall conversion efficiency is limited by the effective absorption length. Furthermore, this material has very large birefringence. Consequently, phase matching can be achieved in an ultrabroad wavelength range. Even though GaSe has potential to reach THz OPO with a single pump beam [18], DFG offers relative compactness, simplicity for tuning, straightforward alignment, much lower pump intensities, and stable THz output. Indeed, unlike OPO, DFG does not require a complicated alignment procedure even if the wavelength tuning is required. The high second-order NLO coefficient (d_{22} = 54 pm/V) and large figure of merit d_{eff}^2/n^3 for GaSe make it the most superior material for the efficient THz generation. Combined with the absorption coefficient in the THz, we can actually define a new figure of merit: $d_{eff}^2/n^3\alpha^2$. It turns out that its value for GaSe is a factor of about 9×10⁴ larger than that for bulk LiNbO₃ at about 200 μm [17-19].
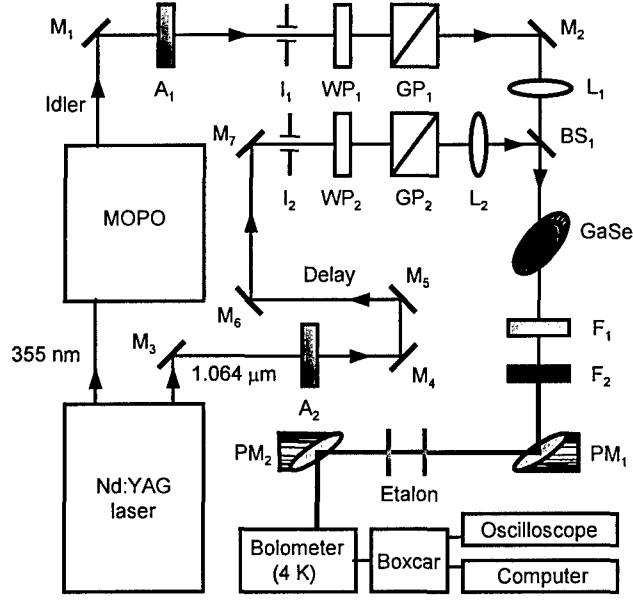
Fig. 1. Experimental setup for THz radiation based on DFG in a GaSe crystal. M_1-M_7, Mirrors; A_1-A_2, attenuators; I_1-I_2, irises; WP_1-WP_2, $\lambda/2$ Wave Plates; GP_1-GP_2, Glan Polarizers; BS_1, 50/50 Beamsplitter, L_1-L_2, convex lenses with f = 10 and 20 cm, respectively; PM_1-PM_2, parabolic mirrors; F_1-F_2, Germanium and black polyethylene filters, respectively. Etalon is made from two parallel germanium plates mounted on two mirror mounts on two separate translation stages.

An experimental setup is shown in Fig. 1. As a DFG pump source we have used a Nd:YAG laser (duration of 10 ns, pulse energy of up to 6 mJ, repetition rate of 10 Hz). As a second (tunable source) we have used an output of a BBO (β-BaB_2O_4)-based OPO pumped by the third harmonic of the same laser with the following parameters: duration of 5 ns, pulse energy of up to 3 mJ, and repetition rate of 10Hz. The peak intensity for the Nd:YAG pump beam is about 17 MW/cm^2, which is below the optical damage threshold 30 MW/cm^2 in GaSe at similar pulse durations [17]. This pump intensity was ~ 30 times lower than that used for achieving the THz OPO in $LiNbO_3$ [13]. The THz wave generated from the GaSe crystal was collimated and then focused into a Si bolometer by two off-axis parabolic metal mirrors. We first used a 15-mm-long z-cut GaSe crystal, with a 35 × 20 mm elliptical aperture, and no antireflection coatings. For type-oee phase-matching (PM) interaction (o and e indicate the polarization of the beams inside the GaSe crystal), the effective NLO coefficients for GaSe depend on the PM (θ) and azimuthal (φ) angles as $d_{eff} = d_{22} \cos^2\theta \, \cos3\varphi$ [17]. To optimize d_{eff}, azimuthal angles of $\varphi = 0°$, ± 60°, ± 120°, and ± 180° can be chosen such that $|\cos 3\varphi| = 1$, which were confirmed in our experiment.

Fig. 2 shows the external PM angular tuning curves for the type-oee collinear DFG THz radiation. We have observed the phase-matching peaks by varying three parameters: θ, φ, and pump wavelength λ (dots in Fig. 2). Tunable and coherent THz output radiation in the extremely-wide range of 56.8–1618 μm (0.18–5.27 THz) have been achieved, see inset of Fig. 2. The short-wavelength cutoff for the THz output is due to the presence of the narrow lattice absorption band for GaSe, which peaks at 40 μm [20]. On the other hand, the long-wavelength end is limited by the measurable THz signal since it decreases as the output wavelength increases [21]. Obviously, the signal-to-noise ratio for the bolometer determines the cut-off on this side. Fig. 3 shows the dependences of the THz wavelength on the OPO idler wavelength. Based on
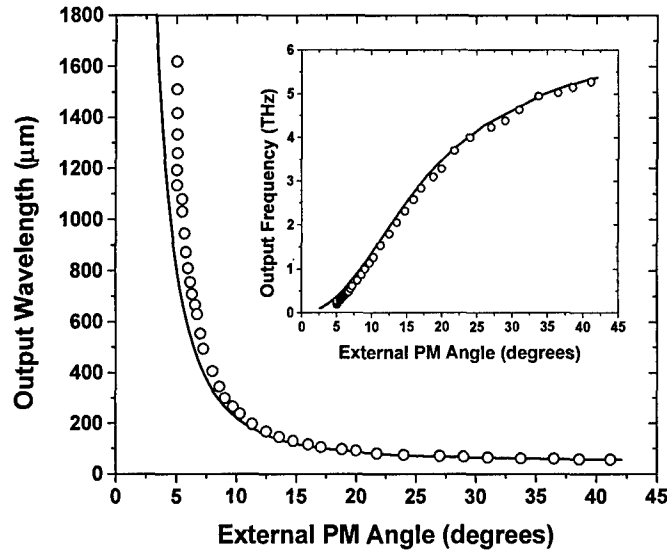
Fig. 2. Output wavelength vs. external PM angle. Inset: output frequency vs. external PM angle. Open circles and solid curves correspond to experimental and calculated results using refractive-index dispersion relations for GaSe in Ref. [22], respectively.

Fig. 2 and 3 we conclude that the theoretical (based on Ref. [22]) and experimental PM curves are in an excellent agreement over the entire range of the output wavelengths. The wavelength of the monochromatic THz wave was easily verified by using a scanning etalon made of two Ge wafers (a finesse of about 4) in Fig. 1. The inset in Fig. 3 shows an example for measuring one THz wavelength (668 μm) by using the scanning Ge etalon. Each of the measured THz wavelengths was consistent with that determined from the wavelengths of two incident pump beams used for the DFG.
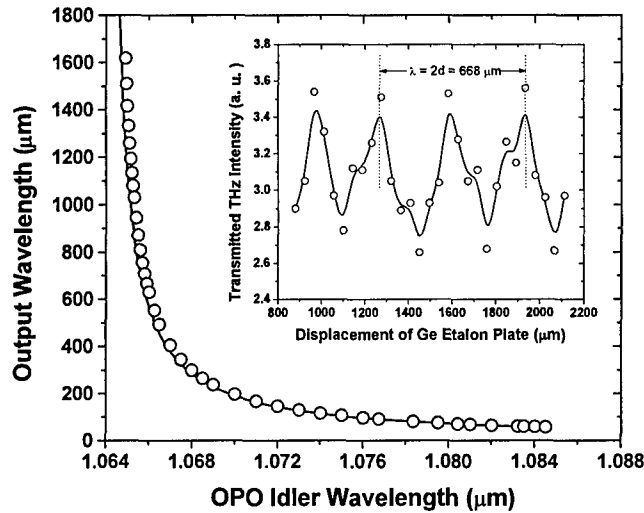

Fig. 3. Output wavelength vs. OPO idler wavelength based on DFG. Open circles and solid curve correspond to experimental and calculated results using refractive-index dispersion relations for GaSe in Ref. [22], respectively. Inset: measurement of THz wavelength (668 μm) by scanning Ge etalon. Open circles correspond to experimental results and solid curve is B-Splined result from data.
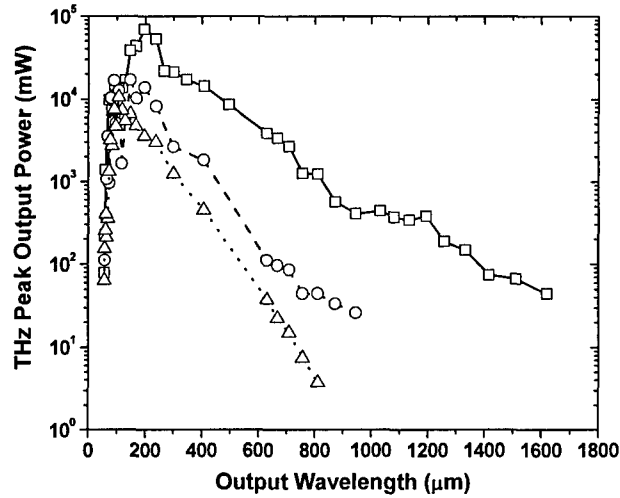
Fig. 4. Peak output power vs. output wavelength for three pure GaSe crystals with thickness (along z axis) of 4 mm (triangles), 7 mm (open circles) and 15 mm (squares), respectively.

The above THz radiation had the pulse duration of 5 ns and a repetition rate of 10 Hz. The measured THz peak output powers for the 15-mm-thick GaSe crystal at different THz output wavelengths are shown in Fig. 4 (squares). We have also plotted the measured THz peak output powers vs. the output wavelength for two other GaSe crystals with the length (along z axis) of 4 mm (triangles) and 7 mm (circles) in Fig. 4. One can see that the three GaSe crystals have different THz tuning ranges: 56.8-810 μm for 4 mm; 56.8-944 μm for 7 mm; 56.8-1618 μm for 15 mm. They also have different maximum THz peak output powers with different corresponding peak wavelengths: 4 mm, 10.5 W at 106 μm; 7 mm, 17.0 W at 146 μm; 15 mm, 69.4 W at 196 μm. Three maximum THz peak output powers correspond to the conversion efficiencies of 1.77×10^{-5}, 4.5×10^{-5} and 1.8×10^{-4}, with the corresponding photon conversion efficiencies of 0.18%, 0.62%, and 3.3%, respectively. Obviously the highest THz peak output powers are determined by the effective absorption lengths of the GaSe crystal in the THz domain, which are larger than 15 mm. Considering the collinear PM DFG, the power conversion efficiency can be calculated by using Ref. [21]

$$\frac{P_1}{P_2} = \frac{1}{2}\left(\frac{\mu_0}{\varepsilon_0}\right)^{3/2} \frac{\omega_1^2 d_{eff}^2 L^2}{n_1 n_2 n_3} \left(\frac{P_3}{\pi w^2}\right) T_1 T_2 T_3 \exp(-\alpha_1 L)\left(\frac{1 - \exp(-\Delta\alpha L / 2)}{\Delta\alpha L / 2}\right)^2,$$

where $T_j = 4n_j/(n_j+1)^2$ is the Fresnel transmission coefficient for each facet, the subscripts $j = 1$, 2, 3 correspond to the THz wave and two pump waves, respectively, $\Delta\alpha = |\alpha_2 + \alpha_3 - \alpha_1|$, and w is the beam size for the pump. Typically, w is measured to be about 1 mm. The theoretical conversion efficiencies, corresponding to the above three maximum output powers, are calculated to be 3.1×10^{-5}, 9.6×10^{-5} and 4.4×10^{-4}, respectively.

To make the THz source much more compact, intracavity DFG can be employed: an antireflection-coated GaSe crystal can be placed inside a cavity for an OPO based on a BBO. The entire system can be directly pumped by a Nd:YAG laser. By using such a configuration, the size of the system can be reduced to one third of the entire system employed in our experiment. A synchronously-pumped THz OPO can also be implemented based on a GaSe crystal.

All these future studies may make huge impact on the U.S. Air Force. In particular, a system based on a coherent and compact THz source can be used for the identification of chemicals and DNA's with greatly-improved sensitivities. In the future it is conceivable for us to implement a THz imaging system that may partially see through the sand storms.

The results summarized here were published in Opt. Lett. (2002) and Optics in 2002.

1. B. B. Hu and M. C. Nuss, Opt. Lett. **20**, 1716 (1995); Q.Chen, Z. Jiang, G. X. Xu, and X.-C. Zhang, Opt. Lett. **25**, 1122 (2000).
2. J. L. Johnson, T. D. Dorney, and D. M. Mittleman, Appl. Phys. Lett. **78**, 835 (2001).
3. M. Schall and P. U. Jepsen, Opt. Lett. **25**, 13 (2000).
4. C. Rønne, P. Åstrand, and S. R. Keiding, Phys. Rev. Lett. **82**, 2888 (1999).
5. T. I. Jeon, D. Grischkowsky, A. K. Mukherjee, and R. Menon, Appl. Phys. Lett. **77**, 2452 (2000).
6. Y. S. Lee, R. Meade, T. B. Norris, and A. Galvanauskas, Appl. Phys. Lett. **78**, 3583 (2001).
7. P. G. O'Shea and H. P. Freund, Science **292**, 1853 (2001).
8. M. Nagel, P. H. Bolivar, M. Brucherseifer, H. Kurz, A. Bosserhoff, and R. Büttner, Appl. Phys. Lett. **80**, 154 (2002).
9. E. R. Brown, F. W. Smish, and K. A. McIntosh, J. Appl. Phys. **73**, 1480 (1993).
10. S. Matsuura, G. A. Blake, R. A. Wyss, J. C. Pearson, C. Kadow, A. W. Jackson, and A. C. Gossard, Appl. Phys. Lett. **74**, 2872 (1999).
11. F. Zernike, Jr., and P. R. Berman, Phys. Rev. Lett. **15**, 999 (1965).
12. K. Kawase, T. Hatanaka, H. Takahashi, K. Nakamura, T. Taniuchi, and H. Ito, Opt. Lett. **25**, 1714 (2000).
13. K. Imai, K. Kawase, J. –I. Shikata, H. Minamide, and H. Ito, Appl. Phys. Lett. **78**, 1026 (2001).
14. L. Friedman, G. Sun, and R. A. Soref, Appl. Phys. Lett. **78**, 401 (2001).
15. R. Köhler, A. Tredicucci, F. Beltram, H. E. Beere, E. H. Linfield, A. G. Davies, and D. A. Ritchie, Appl. Phys. Lett. **80**, 1867 (2002).
16. I. Vurgaftman and J. R. Meyer, Appl. Phys. Lett. **75**, 899 (1999).
17. V. G. Dmitriev, G. G. Gurzadyan, and D. N. Nikogosyan, *Handbook of Nonlinear Crystals* (Springer, Berlin, 1999), pp. 119-125; pp. 166-169.
18. Y. J. Ding and I. B. Zotova, Opt. Quant. Electron. **32**, 531 (2000).
19. Y. J. Ding and J. B. Khurgin, Opt. Commun. **148**, 105 (1998).
20. E. D. Palik, *Handbook of optical Constants of Solid* (Academic, New York, Vol. III, 1998).
21. A. Yariv, *Quantum Electronics* (Wiley, New York, 1988), p. 401.
22. K. L. Vodopyanov and L. A. Kulevskii, Opt. Commun. **118**, 375 (1995).

2. Quantum-well dots formed by a single InGaAs/GaAs quantum well strained by an array of InAs quantum dots

Semiconductor quantum dots (QD's) are expected to dramatically improve the performance of optoelectronic devices. So far, two methods are mainly used for fabricating QD structures. One method utilizes the complicated lithography, etching, and then regrowth processes [1]. Due to the limitation imposed by the current lithographic techniques, the QD's fabricated by this method usually have a larger size and lower density than the desirable values. Furthermore, the QD's are easy to be contaminated during the etching process and they may contain many defects. Another method takes advantage of a phase transition from a deposited layer of a few monolayers thick on a buffer layer to 2-D islands due to lattice mismatch between the two layers. For example, InAs QD's can be easily formed on the top of a GaAs buffer layer [2]. Such a type of the QD's can be incorporated into many optoelectronic devices with greatly-imrpoved performances. For example, a laser diode based on the QD's exhibits a much lower threshold [3]. This simple method has an obvious advantage of reaching a small size and high density. However, as a result of self-assembling process the size of the QD's usually fluctuates within ±10% [4]. Recently, strain-induced quantum-well (QW) nanostructures, i.e. quantum-well dots (QWD's), have attracted more and more attention since such structures can be defect-free [5-12].

So far, most of QWD's are observed in the InGaAs and InGaP QW's strained by the InP QD's [7-12]. In addition, these InP QD's are not capped for the most of the work in the past. Since the QW thickness can be controlled within a subatomic layer, the size fluctuation of the strain-induced QWD's is expected to be substantially reduced. Moreover, the interface and surface recombination rates can be significantly reduced. Furthermore, since the QWD's are formed inside the QW layer, the capture rate for photogenerated carriers can also be improved. However, all these predicted improvements have not been systematically confirmed.

In this report, we demonstrate that the measurements of photoluminescence (PL) spectrum can be an effective technique to investigate the QWD's with $In_{0.26}Ga_{0.74}As$/GaAs as a single QW and InAs QD's as stressors, capped by a GaAs layer. In particular, we have compared our results with those for the InAs QD's without the QW layer. Our direct comparison shows the PL peak of the InAs:$In_{0.26}Ga_{0.74}As$/GaAs QWD's has narrower linewidths and higher intensities than the self-assembled InAs QD's. Furthermore, the spatial inhomogeneities of dot size reflected by the PL peak energies and linewidths are also significantly reduced for the $In_{0.26}Ga_{0.74}As$/GaAs QWD's. It is important for us to note that the differences between our results and those obtained previously lie in the presence of a GaAs cap layer, InAs islands, and a sharp PL peak.

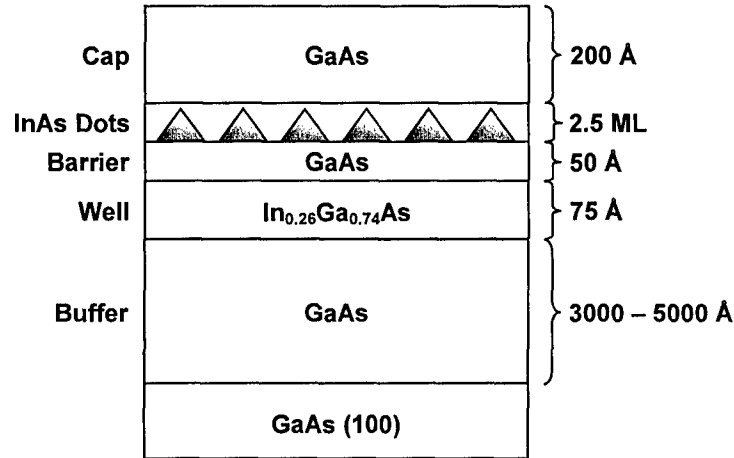| Cap | GaAs | 200 Å |
InAs Dots	△ △ △ △ △ △	2.5 ML
Barrier	GaAs	50 Å
Well	$In_{0.26}Ga_{0.74}As$	75 Å
Buffer	GaAs	3000 – 5000 Å
	GaAs (100)	

Fig. 1. Structure of quantum-well dots.

The QWD shown in Fig. 1 is grown on a GaAs (100) substrate in a Riber 32 MBE system at the temperature of 500°C and growth rates of 0.23, 0.28 and 0.1 ML/s for GaAs, InGaAs, and InAs layers, respectively. It consists of a 300 nm-thick GaAs buffer layer, 26 ML-thick $In_{0.26}Ga_{0.74}As$ well, 18 ML-thick GaAs barrier, 2.5 ML-thick InAs, and a 20 nm-thick GaAs cap layer. Due to the large lattice mismatch (7%) between InAs and GaAs, the 2.5 ML-thick InAs layer actually breaks into the self-assembled QD's with an average diameter and height of ~10 nm and ~5 nm, respectively, from a typical TEM picture. Similar to the InGaAs and InGaP QWD's strained by the InP QD's studied in Refs. [7-12], each InAs QD applies a 2-D potential to the QW layer within the lateral plane beneath it. Therefore, the strain-induced QWD's are formed where the electrons and holes carriers are quantum-confined due to the 2-D potential in additional to the 1-D QW potential. In order to compare the experimental results between the QWD's and the self-assembled QD's, two additional samples are grown, one of which only has the self-assembled InAs QD's and the second one just has an $In_{0.26}Ga_{0.74}As$/GaAs QW. For the

results presented here, we have grown two sets of the QWD and QD samples labeled as Sample Sets #1 and #2.
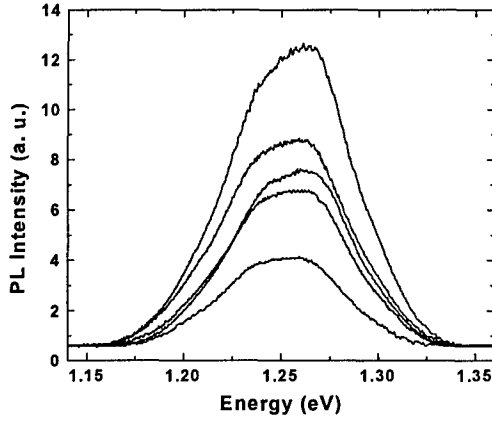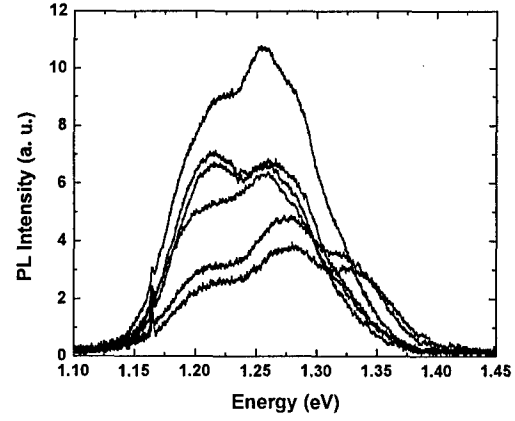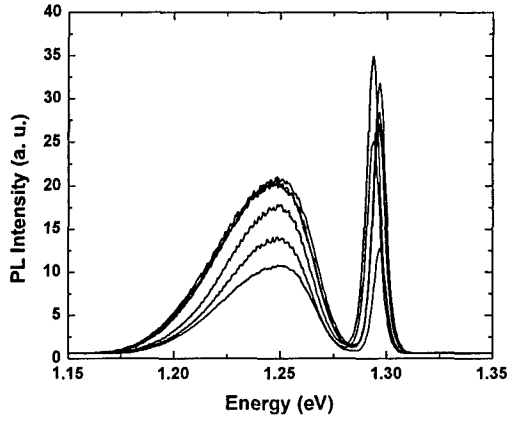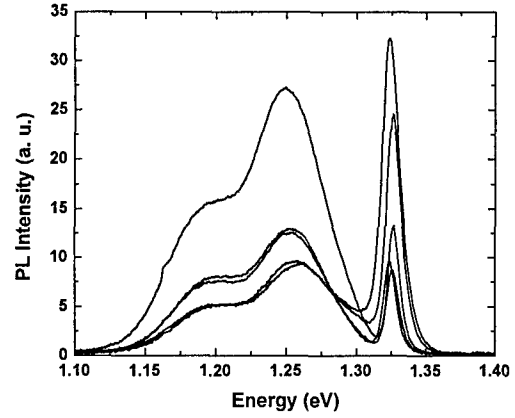

Fig. 2(a)

Fig. 2(b)

Fig. 2(c)

Fig. 2 (d)

Fig. 2. PL spectra for Sample Set #1: (a) QD's and (b) QWD's; Sample Set #2: (c) QD's and (d) QWD's, from location to location, within the lateral plane, measured at 4.3 K with a pump intensity of 435 W/cm^2.

A Ti:Sapphire laser with the typical wavelength of 800 nm is used as a pump source in all the PL measurements. Fig. 2(a)-(d) show the PL spectra of the QWD's and the self-assembled QD's for Sample Sets #1 and #2 measured at different lateral positions. The focal area for the laser beam where the PL measurements are made is about 0.5 cm^2 for each sample. One can see from Fig. 2 that the two sets of the samples have produced completely different PL spectra. Specifically, for Sample Set #2 [Fig. 2(c)] we have observed three PL peaks. The peak energies of the three peaks and the separations among them are similar with those in Ref. [13]. This indicates that the average dot size (more precisely volume) of the self-assembled InAs dots for Sample Set #2 is about the same as that in Ref. [13]. However, for Sample Set #1 [Fig. 2(a)] we have only observed a single PL peak. What is more, the peak energy is higher than the ground transition energy for Sample Set # 2. We believe this is because the InAs dots in Sample Set #1 have a smaller average size than those in Sample Set #2. As a result, the self-assembled InAs dots in Sample Set #1 only have one ground electron state in the conduction band. It is worth

noting that in all the QWD samples we have studied there is a 20-nm GaAs layer to cap the self-assembled InAs dots in our QWD samples. Therefore, the self-assembled QD's and the QWD's are actually coupled with each other due to the thin barrier layer between them. The PL peaks observed by us correspond to the recombination between the electrons and holes in these coupled structures. Such a configuration is quite different from that studied in all the previous work.

Table 1. Comparison of PL characteristics between self-assembled QD's and QWD's. PL peak energy, linewidth, and integrated intensity correspond to average values over a laser-focal area of 0.5 cm^2 measured at 4.3 K with pump intensity of 435 W/cm^2.

Sample	QD's #1	QWD's #1	QD's #2	QWD's #2
Average PL peak energy (E_{max}-E_{min})	1.261 eV (3 meV)	1.249 eV (1.3 meV)	1.265 eV (25 meV)	1.255 eV (11 meV)
Peak energy fluctuation (E_{max}-E_{min})/(E_{max}+E_{min})	0,0024	0.0010	0.0198	0.0088
Average linewidth	78 meV	49 meV	141 meV	106 meV
Average integrated PL intensity	28890	38189	7324	13514
PL intensity fluctuation (I_{max}-I_{min})/(I_{max}+I_{min})	0.44	0.31	0.39	0.36

Based on the comparisons of the PL spectra shown in Fig. 2, one can see that the optical properties of the QWD samples are obviously improved. In Table 1 we have listed the average PL peak energy, peak linewidth, integrated PL intensity, and fluctuations of the peak energy and PL intensity for each sample within the laser focal area. One can see that the average PL peak linewidth for the QWD's is narrower than that for the InAs QD's by 29 meV and 35 meV for Sample Sets #1 and #2, respectively. Fig. 3 summarizes the dependences of the PL peak linewidths on the pump intensity for the QWD's and InAs QD's of Sample Set # 1 measured at a randomly-chosen lateral position. One can see from Fig. 3 that the linewidth difference between the InAs QD's and QWD's is almost a constant within the entire range of the pump intensities. These results represent significant differences between the two structures, indeed. We believe that the linewidth broadenings for the both structures are inhomogeneous in nature and caused by the size fluctuations.

Another important parameter is the spatial uniformity of the QWD's within the lateral plane. By comparing the spectra in Fig. 2, we can see that the peak energies for the QWD's more or less stay the same while those for the QD's shift quite a lot. As a matter of fact, the shift of the PL peak energy from one position to the next within the lateral plane in the self-assembled InAs QD samples can be as high as 3 meV and 25 meV for Sample Sets #1 and #2, respectively. On the other hand, in the QWD's, the corresponding fluctuations are both significantly reduced by 56% (i.e. 1.3 meV and 11 meV, respectively). These results indicate that the QWD's are much more uniform than the self-assembled QD's within the lateral plane. Typically, the size for the self-assembled QDs fluctuates within ±10% [4]. In fact, since the height for each QD is much smaller than the diameter (about a factor of 2 in our samples), the PL peak energy and linewidth are strongly dependent on the spatial distribution of the height within the lateral plane. However, in the QWD's the well width can be controlled within a subatomic layer. Therefore, the carriers staying within the QWD's are primarily affected by the lateral sizes (diameters) of the QWD's. This explains the reason why the QWD's are much more uniform than the QD's. However, as

one can see from Table 1 the amount of the PL-intensity fluctuation from one location to the next is slightly improved for the QWD samples. If we assume that the PL intensities are primarily determined by the densities of the QWD's and QD's, we conclude that every single InAs QD must have produced the corresponding QWD. In this case, the slight improvement in the PL-intensity fluctuation could be explained by the fact that in the QD samples there is also a non-uniform distribution of the nonradiative recombination rate.
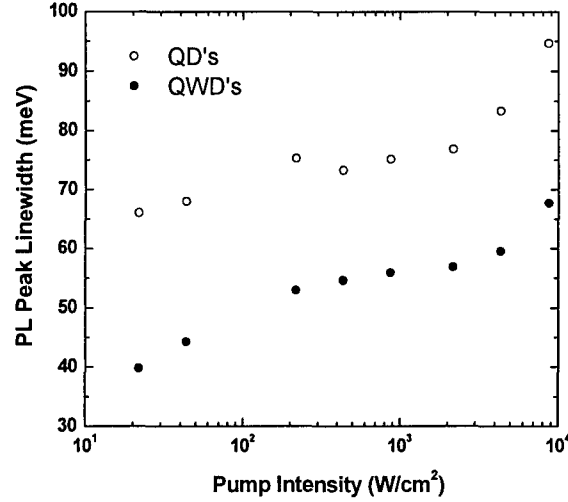

Fig. 3. PL peak linewidth as a function of pump intensity for InAs QD's and $In_{0.26}Ga_{0.74}As/GaAs$ QWD's measured at 4.3 K.
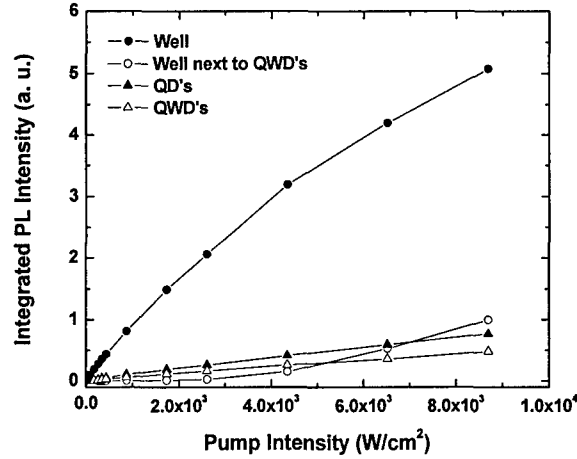

Fig. 4. Average integrated PL intensity as a function of pump intensity measured in QWD, QD and QW samples of Sample Set #2 at 4.3 K.

Besides the issues of the linewidth broadenings and spatial homogeneity, we have also investigated the dependences of the wavelength-integrated PL intensities on the pump intensity for the self-assembled QD's and strain-induced QWD's. From Table 1 one can see that the PL intensity of the QWD's is actually enhanced relative to the InAs QD's. For example, the average integrated PL intensity measured in the QWD's of Sample Set #2 at 435 W/cm^2 is 1.85 times higher than that for the InAs QD's. This PL enhancement on the QWD's can be partially attributed to the fact that the QW is more efficient to capture the photogenerated carriers than the

QD's [14,15]. In fact, in the QWD structure the carriers captured by the $In_{0.26}Ga_{0.74}As/GaAs$ QW readily diffuse into the QWD regions to enhance the PL intensity from the QWD's. As a result, the PL from the QW region in the QWD structure is reduced as shown in Fig. 4. In addition, the interface and surface recombination is also reduced in the QWD structure. These two factors are the main mechanisms for the enhanced PL emission from the QWD regions.

We have made a very important step in eventually utilizing these novel nanostructures for variety of applications that are important to the U.S. Air Force. THz domain has been neglected in the past. It turns that this spectrum region has very rich applications. However, the only THz detectors available now are the bolometers operating at cryogenic temperatures. A structure modification from the quantum-well dots can be used for detecting and emitting THz waves at room temperature. Therefore, we can eventually implement compact THz systems for variety of applications.

The results reported here were published in Laser Phys. Lett. (2005).

1. Y. Sugiyama, Y. Sakuma, S. Muto, and N. Yokoyama, Appl. Phys. Lett. **67**, 256 (1995).
2. A. Madhukar, Q. Xie, P. Chen, and A. Konkar, Appl. Phys. Lett. **64**, 2727 (1994).
3. P. G. Eliseev, H. Li, G. T. Liu, A. Stintz, T. C. Newell, L. F. Lester, and K. J. Malloy, IEEE J. Quantum Electron. **7**, 135 (2001).
4. Y. Masumoto and T. Takagahara, *Semiconductor Quantum Dots*, Springer, NY (2002).
5. K. Kash, B. P. Van der Gaag, Derek D. Mahoney, A. S. Gozdz, L. T. Flore, and J. P. Harbison, Phys. Rev. Lett. **67**, 1326 (1991).
6. Z. Xu and P. M. Petroff, J. Appl. Phys. **69**, 6564 (1991).
7. I-Hsing Tan, M. Y. He, J. C. Yi, E. Hu, and N. Dagli, J. Appl. Phys. **72**, 546 (1992).
8. J. Tulkki and A. Heinämäki, Phys. Rev. B**52**, 8239 (1995).
9. H. Lipsanen, M. Sopanen, and J. Ahopelto, Phys. Rev. B**51**, 13868 (1995).
10. M. Sopanen, H. Lipsanen, and J. Ahopelto, Appl. Phys. Lett. **66**, 2364 (1995).
11. M. Sopanen, M. Taskinen, H. Lipsanen, and J. Ahopelto, Appl. Phys. Lett. **69**, 3393 (1996).
12. M. Braskén, M. Lindberg, M. Sopanen, H. Lipsanen, and J. Tulkki, Phys. Rev. B**58**, 15993 (1998).
13. N. Perret, D. Morris, L. Franchomme-Fossé, R. Côté, S. Fafard, V. Aimez, and J. Beauvais, Phys. Rev. B**62**, 5092 (2000).
14. C. Lingk, W. Helfer, G. von Plessen, J. Feldmann, K. Stock, M. W. Feise, D. S. Citrin, H. Lipsanen, M. Sopanen, R. Virkkala, J. Tulkki, and J. Ahopelto, Phys. Rev. B **62**, 13588 (2000).
15. G. Walter, N. Holonyak, Jr., J. H. Ryou, and R. D. Dupuis, Appl. Phys. Lett. **79**, 1956 (2001).

3. Observation of strong phonon-assisted resonant intervalley up-transfer for electrons in type-II GaAs/AlAs superlattices

Semiconductor superlattices (SL's) usually have high luminescence efficiencies [1,2]. However, for short-period GaAs/AlAs SL's with the thickness of the alternating layers less than ~12 monolayers (ML's), the X-states of AlAs mix with the Γ-states of GaAs. As a result, the lowest electronic state in the conduction band becomes a quasi-X state (type-II SL's). In this case, the type-II SL's have effective indirect-gaps [3-9]. In all the previous experiments on the type-II GaAs/AlAs SL's, a typical photoluminescence (PL) spectrum is dominated by a strong quasi-indirect transition peak with an extremely-weak quasi-direct emission peak appearing as a shoulder in the spectrum [1,3-9]. Recently, it was demonstrated that the PL intensity for the quasi-direct peak could be slightly increased (less than a factor of 2) by raising the temperature of the type-II $(GaAs)_{10}/(AlAs)_{10}$ SL's to 180 K [6]. Such a slight increase in the PL intensity was attributed to the fact that the electrons started to thermally populate the quasi-Γ-states from the quasi-X states as the temperature increased [6]. Obviously, such a mechanism dominates only when the lowest quasi-Γ state is close to the lowest quasi-X state by the thermal energy, k_BT.

In this section, we summarize our results that the quasi-direct emission intensity in short-period type-II GaAs/AlAs SL's can be dramatically enhanced by raising the SL temperature or pump power even if the energy difference between the lowest quasi-Γ state and quasi-X state is much larger than the thermal energy. Furthermore, we have found that the enhanced quasi-direct PL intensity exhibits a quadratic dependence on the pump intensity for the type-II SL's. We argue that our experimental results cannot simply be explained by the mechanism of thermal transfer proposed in Ref. [6]. Instead, we propose a new mechanism of phonon-assisted resonant up-transfer of electrons from the quasi-X state to the quasi-Γ state. Based on this mechanism, we have derived the quasi-direct emission rate and compared it with our experimental results.

Table 1. Short-period GaAs/AlAs SLs used in this experiment. All the energies are measured at 4.3 K at pump intensity of 87.0 W/cm^2. The decay time is measured by 9 ns-laser pulses at pump energy of 3.4 μJ and temperature of 4.3 K.

No.	Thickness (ML) GaAs/AlAs	E_Γ (eV)	E_X (eV)	$\Delta E_{\Gamma X}$(meV)	$\hbar\omega_{p1}$ (meV)	$\hbar\omega_{p2}$ (meV)	τ(ns)
1	17.9/19.3	1.671	-	-	-	-	-
2	12/12	1.801	1.757	44	28	48	500
3	10.5/11.3	1.832	1.767	65	27	48	800
4	10.7/11	1.850	1.776	74	27	48	800
5	8/7	1.975	1.854	121	30	49	1300

Each of the five samples of the short-period GaAs/AlAs SL's studied here (see Table 1) consists of 40 periods of GaAs and AlAs layers grown by molecular-beam epitaxy at 580 °C on a (100) semi-insulating GaAs substrate. The growth rate is 1 ML/s for both GaAs and AlAs layers. The layer thicknesses for samples #1, #3 and #4 and samples #2 and #5 were measured by X-ray diffraction and reflection high-energy electron diffraction, respectively. During the PL measurements, each sample is mounted inside a cryostat and pumped by a 532-nm laser beam.
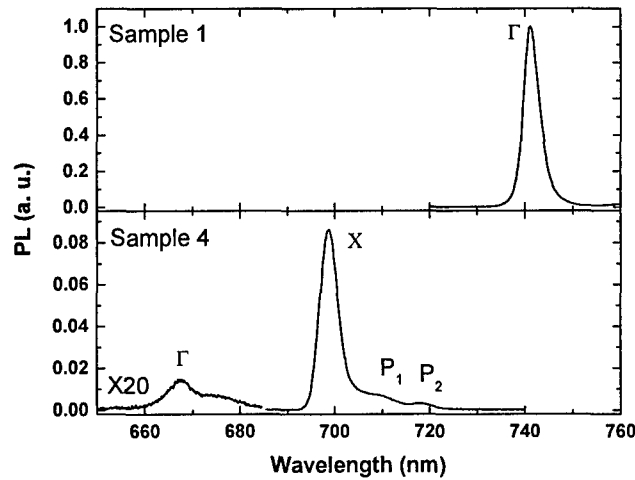

Fig. 1. PL spectra of samples #1 and #4 at the pump intensity of 87.0 W/cm^2. The PL intensity for sample #4 is relative to that for sample #1.
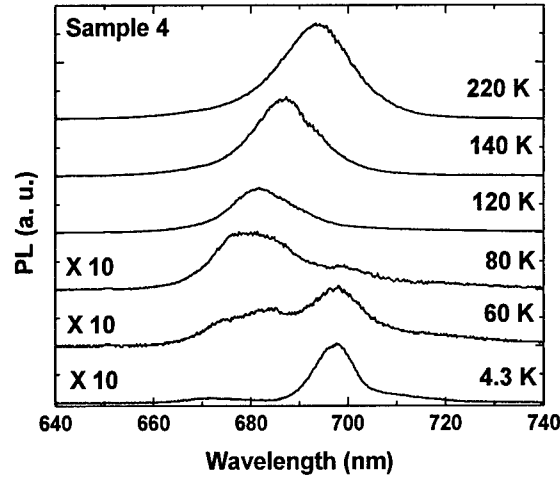
Fig. 2. PL spectra of Sample 4 at the pump intensity of 8.7 kW/cm^2 for different temperatures.

Our measurements show that sample #1 corresponds to type-I SL's whereas samples #2-5 belong to type-II SL's. Fig. 1 shows typical PL spectra for Samples 1 and 4, measured at a low pump intensity (87.0 W/cm^2) and 4.3 K. Similar to the previous results [3-9], our type-II SL's consist of four peaks corresponding to quasi-direct (quasi-Γ), quasi-indirect (quasi-X) transitions, and phonon replicas (P_1,P_2), respectively. Among the phonon replicas P_1 is accompanied by emission of longitudinal optical (LO) phonons in GaAs layers whereas P_2 is by LO phonons in AlAs layers [3,7,9]. From the PL spectra the quasi-direct and quasi-indirect transition energies as well as the LO phonon energies for GaAs and AlAs are directly determined, see Table 1. In order to confirm our assignment on the emission peaks, we have also measured the decay times of the quasi-indirect peaks on samples #2-5, see Table 1.
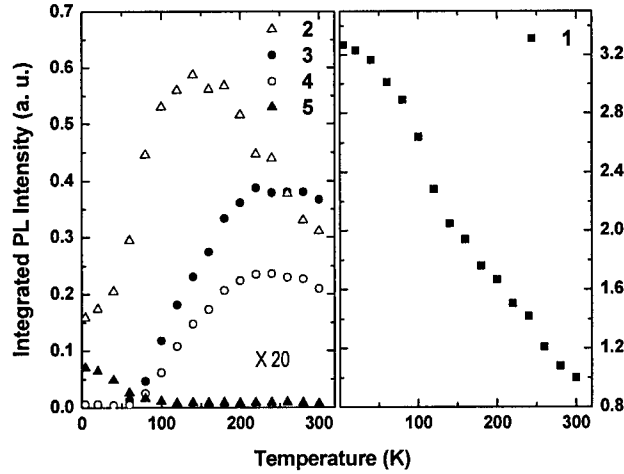

Fig. 3. Wavelength-integrated PL intensities for the quasi-direct transition as a function of the SL temperature measured for samples #1-5 at the pump intensity of 8.7 kW/cm^2. The results have been normalized by the PL intensity for sample #1 at 300 K.

Usually, due to the dissociation of excitons and/or the different effective masses for the

electrons and holes, the PL intensity decreases as the SL temperature increases. Such a behavior was indeed observed on Sample 1, as shown in Fig. 2. However, for samples #2-4, the quasi-direct PL intensity was unusually increased by raising the SL temperature to 150 K-200 K. Although the thermal transfer of the electrons from the quasi-X states to the quasi-Γ states was previously introduced for explaining the enhancement of the quasi-direct PL intensity at high temperatures [6], such a mechanism cannot obviously be used to explain the dramatic increase of the PL intensity observed in our experiment. As one can see from Table 1, since the energy difference between the quasi-Γ and quasi-X states is much larger than the thermal energy, $k_B T$, the effect of the thermal transfer of electrons is negligible.
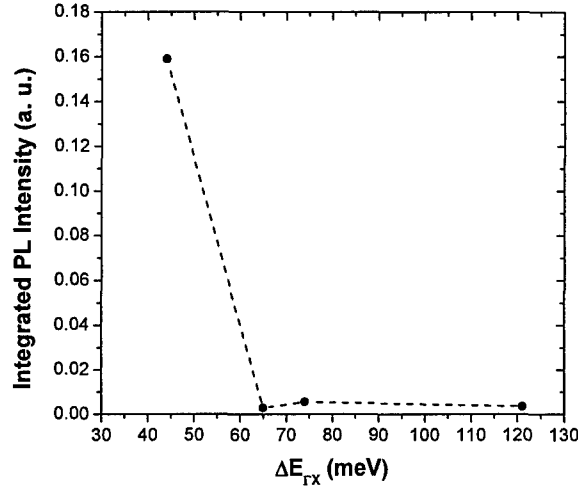

Fig. 4. Wavelength-integrated PL intensity vs. the energy difference between the quasi-Γ and quasi-X states at 4.3 K. Dashed line is to guide eyes.

According to the energy differences between quasi-Γ and quasi-X states in samples #2-4, we believe the intervalley up-transfer for the electrons must be assisted by LO phonons. Due to the momentum conservation, the photogenerated electrons relax to the bottom of the quasi-Γ subband and then to the quasi-X subband, accompanied by phonon emission. Since the phonon scattering process in the time scale of 5~20 ps is much faster than the radiative recombination (typically 300~800 ps) for the quasi-Γ subband [10], most of the quasi-Γ electrons are quickly scattered to the quasi-X subband. Therefore, the excitation process creates a large number of LO phonons in the type-II SL's with the density proportional to the pump intensity. In this case, each quasi-X electron has high probability to absorb a single LO phonon and jump back to the quasi-Γ subband. Such an up-transfer process requires a minimum kinetic energy for each electron [11]:

$$E_M(T) = \Delta E_{\Gamma X}(T) - \hbar \omega_p,\tag{1}$$

where $\Delta E_{\Gamma X}(T)$ is the energy difference between the quasi-Γ and quasi-X subbands and $\hbar \omega_p$ is the phonon energy. Obviously, at 4.3 K since all the electrons have almost zero kinetic energy, this phonon-assisted process can occur only if the phonon energy is higher than $\Delta E_{\Gamma X}$. According to the measurements shown in Table 1, sample #2 is the only one which can satisfy this condition, i.e., $\Delta E_{\Gamma X}$ (44 meV) is lower than the LO phonon energy for AlAs (48 meV). Indeed, we have plotted the integrated quasi-direct PL intensity vs. $\Delta E_{\Gamma X}$ at 4.3 K in Fig. 4. One can see that the quasi-direct PL intensity is much higher for Sample 2 than for sample #3-5 (by a

factor of 56). These results confirm the resonance nature for the phonon-assisted up-transfer of the electrons. At higher SL temperatures, due to the increase of the electron kinetic energies, the electron up-transfer assisted by the GaAs phonons (28 meV) becomes possible in sample #2, which can further enhance the quasi-direct PL intensity. Furthermore, the phonon-assisted up-transfer also takes place in samples #3-5. However, since the values of $\Delta E_{\Gamma X}(T)$ in samples #3-5 are closer to $\hbar\omega_{p_2}$ than $\hbar\omega_{p_1}$, the up-transfer is assisted by the AlAs LO phonons rather than the GaAs phonons. By increasing the SL temperature, more electrons at the quasi-X states can gain a sufficiently large kinetic energy to jump to the quasi-Γ states by absorbing one LO phonon. Moreover, as the SL temperature increases our experimental results show that $\Delta E_{\Gamma X}(T)$ decreases for all the samples, which means that $E_M(T)$ also decreases. Therefore, when the temperature increases the rate of the up-transfer also increases due to the two combined factors mentioned above.

In order to determine the temperature dependence of $\Delta E_{\Gamma X}$, we assume that the valence band-offset in the SL's is independent of the temperature. In addition, the Γ-bandgaps of bulk GaAs and AlAs have similar temperature dependences [12]. Therefore, as the temperature changes the Γ-subband will not change much compared with the Γ-band of bulk GaAs (or AlAs). On the other hand, since the electron at the quasi-X state has a large effective mass (e.g., 1.987 m_0 for GaAs and 0.813 m_0 for AlAs, even heavier than the heavy holes in the two materials) [10], the energy difference between the X-subband and the X-band of AlAs should nearly be a small constant. Therefore, we can approximate the temperature dependences of Γ- and X-subbands by that of the Γ-band of GaAs and X-band of AlAs. Under these approximations, $\Delta E_{\Gamma X}(T)$ can be written as:

$$\Delta E_{\Gamma X}(T) \approx \Delta E_{\Gamma X}(0) - \left(\frac{A_1 T^2}{T + B_1} - \frac{A_2 T^2}{T + B_2} \right), \qquad (2)$$

where $\Delta E_{\Gamma X}(0)$ is the energy difference between Γ- and X-subbands at $T = 0$ K, and A_1, B_1 and A_2, B_2 are constants for Γ-band of GaAs and X-band of AlAs, respectively [12].

Since the phonon-assisted up-transfer corresponds to the transition of the electron from a quasi-X state to a quasi-Γ state, we assume that the following steady-state equation holds between the two states by the absorption of one LO phonon per transition [10]: (Due to the Boltzmann distribution, the probability for the absorption of multiple LO phonons per transition is negligible).

$$\frac{\Delta N_\Gamma}{\tau_S} + \frac{\Delta N_\Gamma}{\tau_R} = BN_X N_P \frac{\int_{E_M}^{\infty} \{1 + \exp[(E - E_{fn})/K_B T]\}^{-1} dE}{\int_0^{\infty} \{1 + \exp[(E - E_{fn})/K_B T]\}^{-1} dE} \cdot \frac{\exp[-(3/2)\hbar\omega_p / K_B T]}{\sum_{n=0}^{\infty} \exp[-\hbar\omega_p(n + 1/2)/K_B T]}, \qquad (3)$$

where ΔN_Γ is the additional electron density at the quasi-Γ state due to the up-transfer; τ_S and τ_R are the scattering time constant and radiative recombination lifetime for the electrons at the quasi-Γ state, respectively; B is a constant for the phonon absorption; N_X is the electron density at the quasi-X state; N_P is the phonon density; and E_{fn} is the quasi-Fermi level for the electrons. Following Eq. (3), the radiative recombination rate can then be written to be

$$\frac{\Delta N_\Gamma}{\tau_R} = \frac{\tau_S}{\tau_S + \tau_R} BN_X N_P \frac{\int_{E_M}^{\infty} \{1 + \exp[(E - E_{fn})/K_B T]\}^{-1} dE}{\int_0^{\infty} \{1 + \exp[(E - E_{fn})/K_B T]\}^{-1} dE} \cdot \frac{\exp[-(3/2)\hbar\omega_p / K_B T]}{\sum_{n=0}^{\infty} \exp[-\hbar\omega_p(n + 1/2)/K_B T]}. \qquad (4)$$

Using Eq. (4), we have plotted the normalized recombination rate as a function of the temperature in Fig. 5, for sample #2 based on the AlAs and GaAs LO phonon-assisted up-transfers, respectively, and samples #3-5 based on the AlAs LO phonon-assisted up-transfer. In our calculations, we choose E_{fn} for the X conduction band to be 200 meV,[10] $A_1 = 0.55$ meV/K, $B_1 = 225$ K, $A_2 = 0.70$ meV, and $B_2 = 530$ K [12]. The other parameters are listed in Table 1. By comparing Fig. 5 with Fig. 3, we can see that the Eq. (4) qualitatively describes the temperature behaviors observed on samples #2-4 except near the room temperature. This is due to the fact that the phonon absorption in these three samples approaches saturation at the high temperature range. In this case, the PL intensity usually decreases as the temperature increases similar to sample #1 shown in Fig. 3. For sample #5, Fig. 5 shows that the calculated PL intensity can be slightly increased near room temperature. However, it is not possible to observe such a slight increase in the experiment since it is compensated by the overall decrease of the PL intensity similar to sample #1. Nevertheless, from the quadratic PL intensity dependence of this sample at high temperatures, see below, the phonon absorption still happens in this sample.
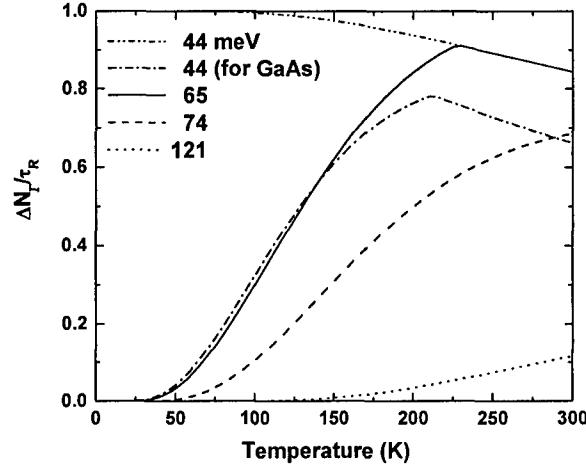

Fig. 5. Theoretical phonon-assisted quasi-direct emission rate as a function of the SL temperature for the four type-II GaAs/AlAs samples used in this experiment.
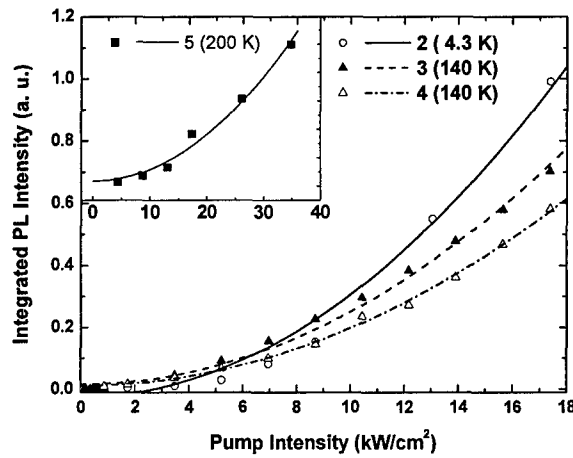

Fig. 6. Wavelength-integrated PL intensities for the quasi-direct transition as a function of the pump intensity measured for sample #2 at 4.3 K, samples #3 and #4 at 140 K, and sample #5 at 200 K. The curves correspond to the fitting by using a square law.

One can readily see from Eq. (4) that the phonon-assisted radiative recombination rate is quadratically dependent on the pump intensity. This is due to the fact that the process of the phonon absorption depends on both the phonon and X-electron densities. Indeed, our experimental results show that the integrated quasi-direct PL intensities for sample #2-5 fit a square power law very well when the sample temperature is above the temperature listed in Fig. 6 for each sample. On the other hand, for Sample 1 in the entire temperature range and samples #3-5 below 60 K, the dependences are always linear due to the absence of the phonon-assisted up-transfers.

Our results indicate that type-II GaAs/AlAs superlattices can be used to efficiently remove LO phonons, i.e. when the light is absorbed by the structure the luminescence can occur. The energy of each photon from the luminescence can be higher than that for the incoming light. Through such a process one can remove LO phonons. This is very important since the scattering of carriers by the LO phonons is the most efficient process in semiconductors. One can immediately think about the possibility of cooling semiconductors based on our results. Such a method of cooling is attractive for the detectors deployed in space since it does not involve in any mechanical movement and power supply. We have optimized our initial structure by incorporating a layer of GaAs for the enhancing the absorption of the incoming light. We have also designed a Sb-based structure consisting of the layers of AlInGaAs, AlGaAsSb, AlInAs, and AlInGaAs for working at the near-IR region. We will report our results in our future progress report.

The results presented here were published in IEEE J. Quantum Electron. (2005).

1. S. Krylyuk, D. V. Korbutyak, V. G. Litovchenko, R. Hey, H. T. Grahn, and K. H. Ploog, Appl. Phys. Lett. **74**, 2596 (1999).
2. V. G. Litovchenko, D. V. Korbutyak, A. I. Bercha, Yu. V. Kryuchenko, S. G. Krylyuk, H. T. Grahn, R. Hey, and K. H. Ploog, Appl. Phys. Lett. **78**, 4085 (2001).
3. E. Finkman, M. D. Sturge, and M. C. Tamargo, Appl. Phys. Lett. **49**, 1299 (1986).
4. F. Minami, K. Hirata, K. Era, T. Yao, Y. Masumoto, Phys. Rev. **B36**, 2875 (1987).
5. M.-H. Meynadier, R. E. Nahory, J. M. Worlock, M. C. Tamargo, J. L. de Miguel, and M. D. Sturge, Phys. Rev. Lett. **60**, 1338 (1988).
6. R. Cingolani, L. Baldassarre, M. Ferrara, M. Lugarà, and K. Ploog, Phys. Rev. **B40**, 6101 (1989).
7. W. Ge, M. D. Sturge, W. D. Schmidt, L. N. Pfeiffer, and K. W. West, Appl. Phys. Lett. **57**, 55 (1990).
8. H. Fujimoto, C. Hamaguchi, T. Nakazawa, K. Taniguchi, K. Imanishi, H. Kato, and Y. Watanabe, Phys. Rev. **B41**, 7593 (1990).
9. V. G. Litovchenko, D. V. Korbutyak, S. Krylyuk, H. T. Grahn, and K. H. Ploog, Phys. Rev. **B55**, 10621 (1997).
10. P. Bhattacharya, *Semiconductor Optoelectronic Devices*, Prentice-Hall, Englewood Cliffs, 1994.
11. M. A. Stroscio and M. Dutta, *Phonons in Nanostructures*, Cambridge, Cambridge, 2001.
12. I. Vurgaftman, J. R. Meyer, and L. R. Ram-Mohan, J. Appl. Phys. **89**, 5815 (2001).

4. TEM picture and band-filling effects in quantum-well dots

Recently, we demonstrated that a single InGaAs/GaAs quantum well strained by InAs quantum dots (i.e. quantum-well dots) exhibits significantly-improved optical properties, see the report on project #2 above. Indeed, we have used measurements of photoluminescence (PL) spectra as an effective technique to characterize these structures. On the two quantum dots (QD's) and quantum-well dots (QWD's), see Table 1 in the report on project #2 above, we have found that the quantum-well dots have much narrower PL linewidths at all levels of the pump intensities. Indeed, the linewidth for the quantum-well dots can be narrower than that for the quantum dots by an amount as large as 35 meV. In addition, the wavelength-integrated PL intensity for the quantum-well dots is much higher. Within the lateral plane, the energies for

optical transitions stay more or less the same for the quantum-well dots whereas for the quantum dots they shift quite a lot from one location to the next.
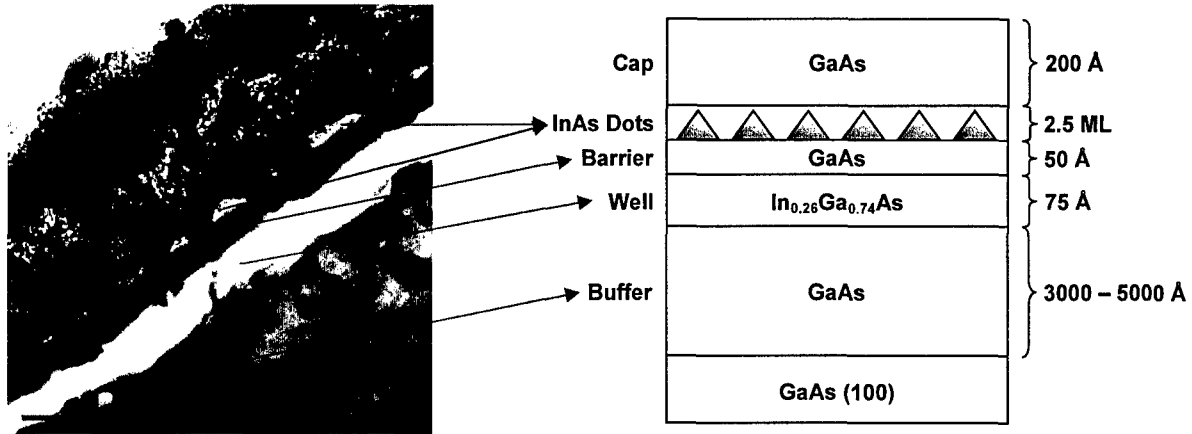

Fig. 1. Left: Cross-section TEM picture of quantum-well dots designed by us and grown by MBE. Right: Designed structure of quantum-well dots.

In order to confirm the structure of the quantum-well dots designed by us and grown by MBE, we have taken a TEM picture of the sample in the cross section, see Fig. 1 (left). In reference to the grown structure based on our design [Fig. 1 (right)], we have seen the layer of the InGaAs well and two GaAs barriers, as marked. In addition, we have confirmed the existence of the InAs dots on the top of the GaAs barrier layer, as marked.
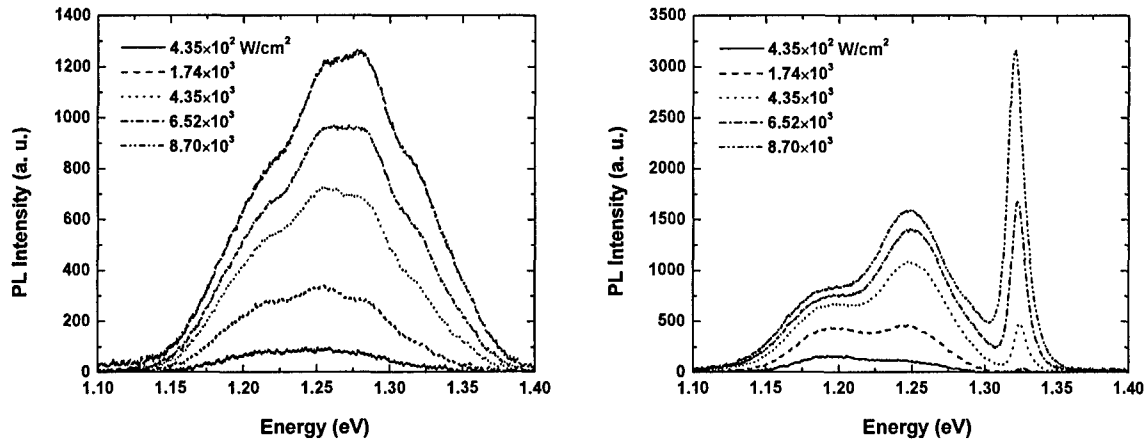

Fig. 2. PL spectra for QD's (left) and QWD's (right) at different pump intensities measured on Sample Set #2 at 4.3 K. See also the report on project #2 above.

As we increase the pump intensity, the QWD's exhibit much more pronounced band-filling effect in Sample Set #2 as shown in Fig. 2. One can see that the relative strength for the lowest transition decreases as the pump power increases. As the pump power increases further, the peak next to the lowest transition starts to become saturated. Eventually, the QW transition peak dominates the PL spectrum. In fact, at the pump power of 150 mw (the pump intensity of 6.5 kW/cm^2), the strength for the QW emission peak is more or less the same as that of the peak near 1.25 eV. However, for the self-assembled QD sample the band-filling effect is much weaker.

This result further supports our conclusion that the QWD's are much more uniform than the self-assembled QD's. On the other hand, for Sample Set #1 as the pump power increases the relative strength for the QW emission in the QWD sample also increases. Eventually at the sufficiently-high pump power, the QW emission dominates the PL spectrum. Similar effects were observed in an InGaAs/GaAs QW strained by InP dots [1], although in our case the PL spectra are eventually dominated by the QW emission peaks.

These results were included in Laser Phys. Lett. (2005).

1. M. Sopanen, H. Lipsanen, and J. Ahopelto, Appl. Phys. Lett. 66, 2364 (1995).

5. A monochromatic and high-power THz source tunable
in the ranges of 2.7–38.4 μm and 58.2-3540 μm for variety of potential applications

A tunable monochromatic THz source is the key to biomedical diagnostics, THz spectroscopy, and chemical identification [1,2]. Such a source can be used to directly probe a DNA binding state [2] and to detect skin cancer. Furthermore, it can be used to study gaseous molecules and biological macromolecules [3]. Other applications such as label-free genetic diagnostics [1] and detection of explosives such as HMX also require a THz source to be tuned in a large range. In all these examples a wide tuning range has an advantage of directly probing characteristic resonances in the THz domain. Besides broad tunability a THz source should have advantages of narrow linewidth, simple alignment, stable THz output, and compactness.
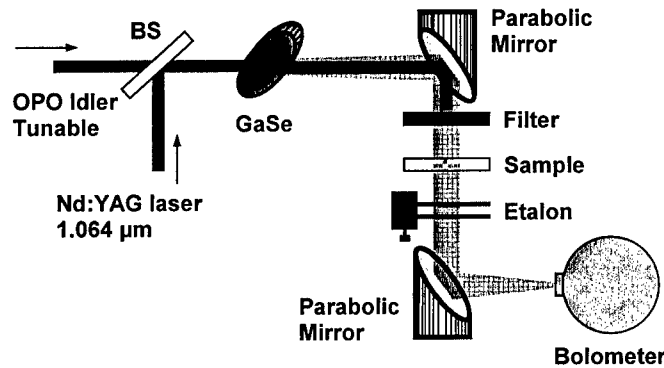

Fig. 1. Schematic setup for THz radiation based on DFG in a GaSe crystal. BS_1, 50/50 Beamsplitter. GaSe crystal was mounted on a rotational stage in order for us to optimize the two angles. Etalon is made from two parallel Ge plates mounted on two mirror mounts on two separate translation stages.

Besides free-electron lasers, high-power THz waves were generated based on synchrotron radiation of relativistically-accelerated cyclotron electrons [4]. Another attractive approach is based on interminiband transitions of a semiconductor heterostructure [5a]. Indeed, at 90 K the output peak power can reach 2.6 mW at 87 μm (3.5 THz) [5b]. However, tuning in a broad range remains to be greatly challenging for such a scheme. Optical-heterodyne mixing can only produce low output powers [6]. Other promising mechanisms proposed recently [7] have not been implemented yet. Among all the schemes, parametric processes such as DFG in nonlinear optical (NLO) crystals such as $LiNbO_3$ and DAST are quite promising [8,9]. However, large absorption coefficients of $LiNbO_3$ and DAST in the THz domain result in low efficiencies and limited tunability [9,10]. Among all the NLO crystals GaSe is the most superior for the THz generation. First, it has the lowest absorption coefficients (α) in the THz wavelength region [11-

13]. Consequently, GaSe has the largest figure of merit for the THz generation ($d_{eff}^2/n^3\alpha^2$), which is several orders of magnitude larger than that for bulk LiNbO₃ at 300 μm [11-13]. Furthermore, since GaSe has anomalously large birefringence PM can be achieved in an ultrabroad wavelength range. Even though GaSe has potential to reach mirrorless parametric oscillation by just using a single pump beam [12], DFG offers the advantages of relative compactness, simplicity for tuning, straightforward alignment, much lower pump intensities, and stable THz output powers and wavelengths. Indeed, unlike the parametric oscillation, DFG does not require a complicated alignment procedure even if wavelength tuning is required. Recently, we implemented a THz source tunable in the range of 56.8–1618 μm (0.18–5.27 THz) based on DFG in GaSe [14]. The peak output power reaches 69.3 W at 196 μm, which corresponds to the power conversion efficiency of 0.018%. In our experiment, we have obtained a linewidth of 0.77 μm (6000 MHz). In principle, this linewidth can be reduced further by using the pump beams with much narrower linewidths.

In this section, we report our most updated result that GaSe can be used to produce much wider tuning ranges and higher peak powers. Our experimental setup is shown in Fig. 1. The peak intensity for the Nd:YAG pump beam focused onto the GaSe crystal is about 17 MW/cm², which much lower than that used for achieving the parametric oscillation in LiNbO₃ [10]. The second pump beam is an idler output beam from an optical-parametric oscillator with the energy per pulse 3-5 mJ. To improve the tuning ranges and peak powers, we used a single GaSe crystal with the length of 20 mm along the optic axis, which is much longer than the previous GaSe crystals. In addition, this new crystal has much better optical and surface quality. Therefore, the linear absorption coefficients in the near-IR region are lower. Furthermore, the damage threshold is higher. For type oe-e and type eo-o collinear PM interaction (o and e indicate the polarization of the beams inside the GaSe crystal), the effective NLO coefficients for GaSe depend on the PM (θ) and azimuthal (φ) angles as $d_{eff} = d_{22}\cos^2\theta\ \cos3\varphi$ and $d_{eff} = -d_{22}\cos\theta\ \sin3\varphi$, respectively [11]. To optimize d_{eff}, azimuthal angles were chosen such that $|cos\ 3\varphi|=1$ and $|\sin3\varphi|=1$.
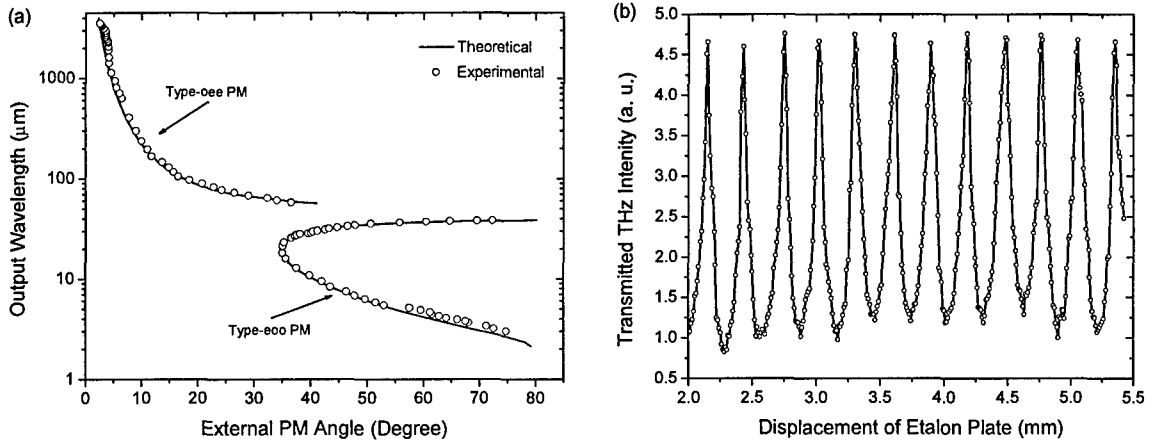

Fig. 2. (a) Type-oe-e and type-eo-o phase-matched output wavelengths vs. external phase-matching angle. Dots – data; solid curves - calculation by using phase-matched conditions and refractive index dispersions [15]. (b) Fabry-Perot etalon scanning spectrum. Displacement between two periods (600 μm) corresponds to THz wavelength. Free spectral range of etalon is about 2.5 GHz.

Fig. 2a shows the external PM angular tuning curves for the type-oee and type-eoo collinear DFG THz radiation. The pump and output wavelengths were verified by an infrared spectrometer and a home-made scanning THz etalon, see Fig. 2b. One can see that the output wavelengths are consistent with those calculated from DFG. For the type-oee PM interaction, monochromatic THz output radiation tunable in the extremely-wide range of 58.2-3540 μm (0.0848 THz – 5.15 THz) has been achieved. This is the widest tuning range ever achieved besides the free-electron lasers. The short-wavelength cutoff for the THz output is due to the presence of a narrow lattice absorption band for GaSe, which peaks at 40 μm [16]. On the other hand, the long-wavelength end is limited by the measurable THz signal since it decreases as the output wavelength increases [17]. Obviously, the signal-to-noise ratio for the bolometer determines the cut-off on this side. By using the type-eoo configuration on the same crystal, the coherent radiation from 2.7 μm to 38.4 μm (111 – 7.81 THz) has also been achieved (Fig. 2a). This tuning range already covers high-frequency end of the THz regime defined in the range of 0.1 THz – 10 THz. It represents significant improvement over the tuning range of 2.7–28.7 μm achieved previously [18]. One can see that the obtained output wavelengths almost cover the entire range of the THz band defined as 0.1 THz – 10 THz except for a narrow gap of 5.15 THz – 7.81 THz (58.2 – 38.4 μm) based on the combination of two types of the phase-matched DFG. Such a narrow gap between the two output ranges is once again due to the lattice absorption band for GaSe, which has the narrowest width among all the nonlinear-optical materials as a result of the layered structure for GaSe.
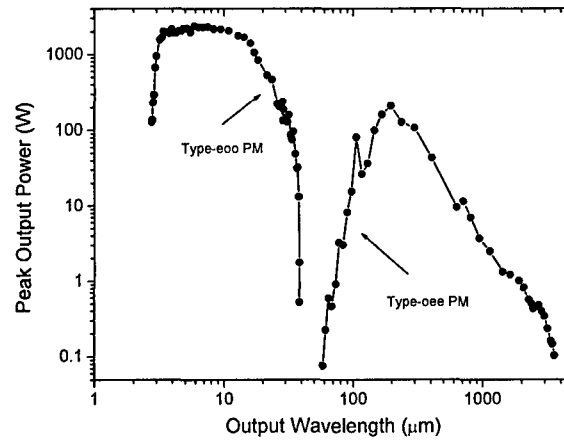

Fig. 3. Output peak power vs. output wavelength for two types of phase-matched DFG.

The generated output beams in the two PM configurations had pulse duration of 5 ns and a repetition rate of 10 Hz. Their pulse energies were measured by a pyroelectric detector and calibrated bolometer (see Fig. 3). The maximum output peak powers for the two PM configurations are measured to be 2364 W at 5.87 μm (51 THz) and 209 W at 196 μm (1.53 THz) corresponding to the power conversion efficiencies of 0.75% and 0.055%, respectively. These output powers and conversion efficiencies are also improved significantly compared with the previous results [14,18]. When the THz wave is tightly focused, the corresponding intensity reaches the level of MW/cm^2 at 196 μm, which can be used to explore a number of new fundamental, nonlinear coherent effects in the THz domain. According to Fig. 2a, the PM angles are small for type-oe-e interaction, which is important since the effective NLO coefficient is correspondingly high while the conversion efficiency is also high. Moreover, in the range of 70-
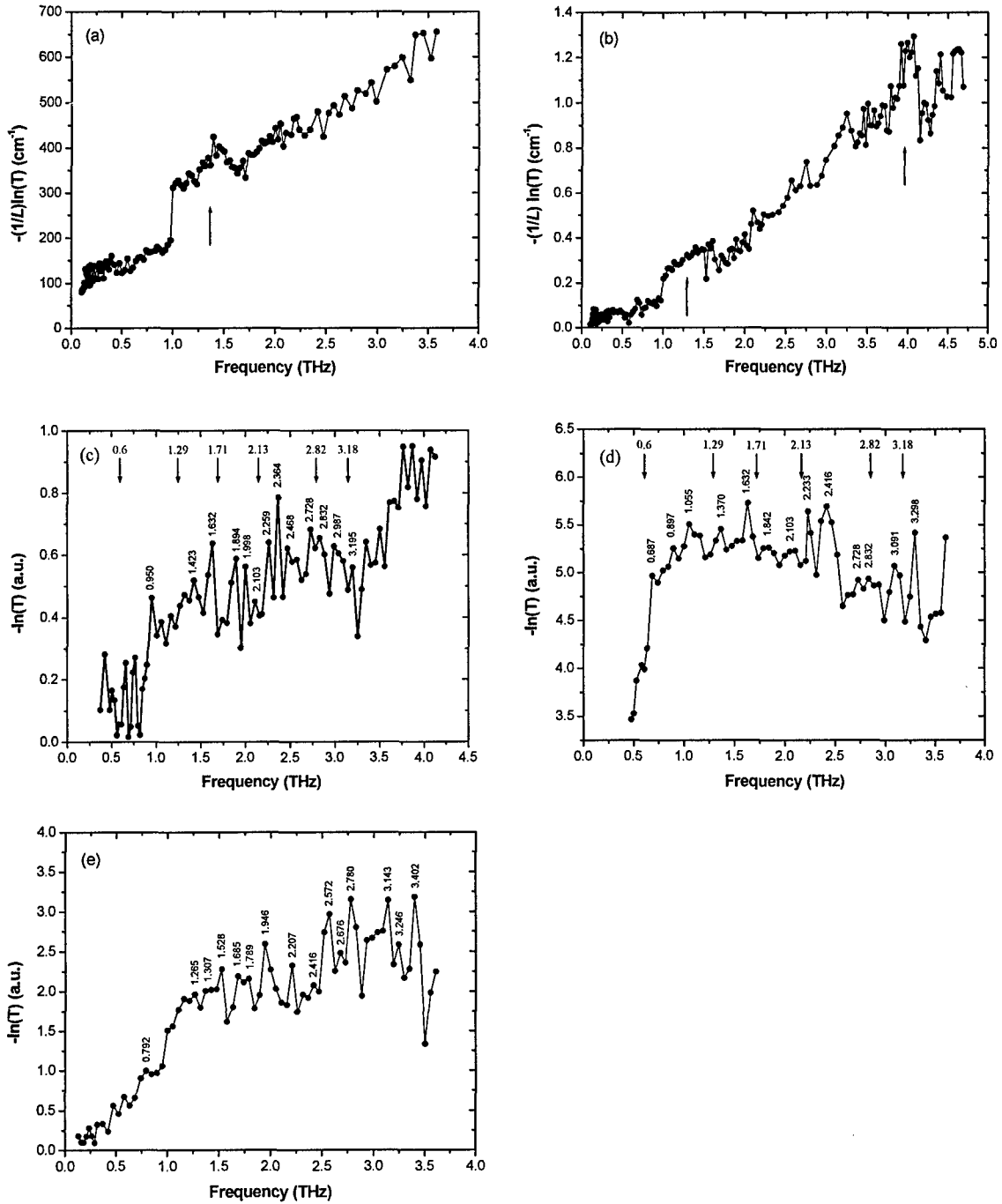
Fig. 4. Directly-measured transmission spectra: (a) Water, where T is transmittance and L is thickness of water. Arrow marks location of B band. (b) Polystyrene foam, where L is thickness of foam. Arrows mark locations of B band and vibrational band. (c) Herring DNA. (d) Salmon DNA. For (c) and (d), arrows mark locations of predicted resonance peaks based on Ref. [21]. (e) Salmon protein.

2000 μm (0.15-4.29 THz) the THz peak power can be kept to be higher than 1 W. Such an extremely-wide tuning range with a high level of the output peak powers can be quite valuable to

a number of potential applications such as DNA and cancer detections, nondestructive evaluations, identification of explosives, and perhaps probing stellar dust clouds for space science [1,2,3,19]. Since a tunable monochromatic THz wave is used for these investigations, transmission spectra can directly be obtained. Indeed, we have directly measured transmission spectra of water, polystyrene foam, herring and salmon DNA, and salmon protein with our preliminary results shown in Fig. 4. For water there is a broad absorption peak in the range of 1.09-1.5 THz (200-275 µm), see Fig. 4a. This is due to bending of intermolecular hydrogen bonds [20]. On the other hand, for polystyrene foam there is a relatively sharp peak near 4.07 THz (73.7 µm) (Fig. 4b). We believe this is due to vibrational band of the one-dimensional polymer chains. Moreover, polystyrene foam has extremely low absorption coefficients and refractive indices of about unity in the THz range. Besides the polystyrene foam, we have also measured herring and salmon DNA's (Figs. 4c and 4d). In our experiments, non-oriented films of DNA's or proteins were used, which were obtained by dissolving DNA or protein powders in distilled water to form gels and then drying the gels in air. According to Figs. 4c and 4d, there are a number of distinct modes in addition to the common phonon modes (i.e., at 1.632, 2.728 and 2.832 THz). These resonance frequencies are consistent with the predictions [21] and the measurements made via FTIR [22]. On the other hand, the spectrum for the salmon protein is quite different from those of the DNA's (Fig. 4e). Although more detailed studies must be carried out, our results indicate that the direct measurements of the transmission spectra may eventually become a valuable tool for identifying DNA's and proteins based on their unique resonance peaks in the range of 1-3 THz.

In summary, our result presented here has set a world record for a widely-tunable, monochromatic (narrow-linewidth), and tabletop THz source. Indeed, an efficient and coherent THz wave tunable in the two extremely-wide ranges of 2.7–38.4 µm and 58.2-3540 µm, with typical linewidths of 6000 MHz, has been achieved by us. These tuning ranges are much wider than those achieved so far based on all the schemes besides the free-electron lasers. Furthermore, the wide spectral bands achieved by us can be easily accessible by rotating the GaSe crystal to change the PM angle and/or to select the configuration. Besides the extremely-wide tuning ranges, the linewidths can also be quite narrow. The maximum peak output power has reached 209 W at 196 µm with a pulse width of about 5 ns. GaSe is the best nonlinear optical material ever used for the THz generation in terms of the absorption coefficient in the THz domain and nonlinear coefficient. The transmission spectra of DNA's directly measured by us can eventually become valuable for characterizing and perhaps identifying biological macromolecules.

A widely-tunable THz source with narrow linewidths is critical for realizing the applications of absorption spectroscopy on gaseous molecules, chemical identification, and biomedical diagnostics, all of which are important to the U.S. Air Force. Furthermore, since the peak power is quite high one can envision a single-shot THz camera for imaging. Such a source can also be used for the investigation of nonlinear coherent THz effects.

These results were published in Appl. Phys. Lett. (2004).

1. P. G. O'Shea and H. P. Freund, Science **292**, 1853 (2001).
2. M. Nagel, P. H. Bolivar, M. Brucherseifer, H. Kurz, A. Bosserhoff, and R. Büttner, Appl. Phys. Lett. **80**, 154 (2002).
3. D. L. Woolard, T. R. Globus, B. L. Gelmont, M. Bykhovskaia, A. C. Samuels, D. Cookmeyer, J. L. Hesler, T. W. Crowe, J. O. Jensen, J. L. Jensen, and W. R. Loerop, Phys. Rev. E **65**, 051903 (2002).
4. G. L. Carr, M. C. Martin, W. R. McKinney, K. Jordan, G. R. Neil, and G. P. Williams, Nature **420**, 153 (2002).

5. (a) R. Köhler, A. Tredicucci, F. Beltram, H. E. Beere, E. H. Linfield, G. Davies, D. A. Ritchie, R. C. Lotti, and F. Rossi, Nature **417**, 156 (2002). (b) G. Scalari, L. Ajili, J. Faist, H. Beere, E. Linfield, D. Ritchie, and G. Davies, Appl. Phys. Lett. **82**, 3165 (2003).

6. E. R. Brown, F. W. Smish ,and K. A. McIntosh, J. Appl. Phys. **73**, 1480 (1993).

7. I. Vurgaftman and J. R. Meyer, Appl. Phys. Lett. **75**, 899 (1999); L. Friedman, G. Sun, and R. A. Soref, Appl. Phys. Lett. **78**, 401 (2001).

8. F. Jr. Zernike and P. R. Berman, Phys. Rev. Lett. **15**, 999 (1965).

9. K. Kawase, T. Hatanaka, H. Takahashi, K. Nakamura, T. Taniuchi and H. Ito, Opt. Lett. **25**, 1714 (2000).

10. K. Imai, K. Kawase, J. –I. Shikata, H. Minamide and H. Ito, Appl. Phys. Lett. **78**, 1026 (2001).

11. V. G. Dmitriev, G. G. Gurzadyan and D. N. Nikogosyan, Handbook of Nonlinear Optical Crystals (Springer, Berlin, 1999), pp. 119-125, 166-169.

12. Y. J. Ding and I. B. Zotova, Opt. Quant. Electron. **32**, 531 (2000).

13. Y. J. Ding and J. B. Khurgin, Opt. Commun. **148**, 105 (1998).

14. W. Shi, Y. J. Ding, N. Fernelius, and K. L. Vodopyanov, Opt. Lett. **27**, 1454 (2002).

15. K. L. Vodopyanov and L. A. Kulevskii, Opt. Commun. **118**, 375 (1995).

16. E. D. Palik, Handbook of optical Constants of Solid (Academic, New York, Vol. III, 1998).

17. A. Yariv, Quantum Eletronics (Wiley, New York, 1988), p. 401.

18. W. Shi, Y. J. Ding, X. Mu and N. Fernelius, Appl. Phys. Lett. **80**, 3889 (2002).

19. W. S. Holland, J. S. Greaves, B. Zuckerman, R. A. Webb, C. McCarthy, I. M. Coulson, D. M. Wather, W. R. F. Dent, W. K. Gear, and I. Robson, Nature **392**, 788 (1998).

20. H. R. Zelsmann, J. Mol. Structure **350**, 95 (1995).

21. M. Bykhovskaia, B. Gelmont, T. Globus, D. L. Woolard, A. C. Samuels, T. Ha-Duang, and K. Zakrzewska, Theor. Chem. Acc. **106**, 22 (2001).

22. J. W. Powell, G. S. Edwards, L. Genzel, F. Kremer, A. Wittlin, W. Kubasek, and W. Peticolas, Phys. Rev. A **35**, 3929 (1987).

6. Coherent THz waves based on
difference-frequency generation in zinc germanium phosphide

In this section, we report our new result on the improvements of the tuning ranges and peak powers by using $ZnGeP_2$, based on phase-matched difference-frequency generation (DFG). Such a significant progress is made possible by using a new and longer $ZnGeP_2$ crystal. Furthermore, the absorption coefficients of this new crystal at the two pump wavelengths are further reduced as a result of the annealing process, as confirmed by our measurements.
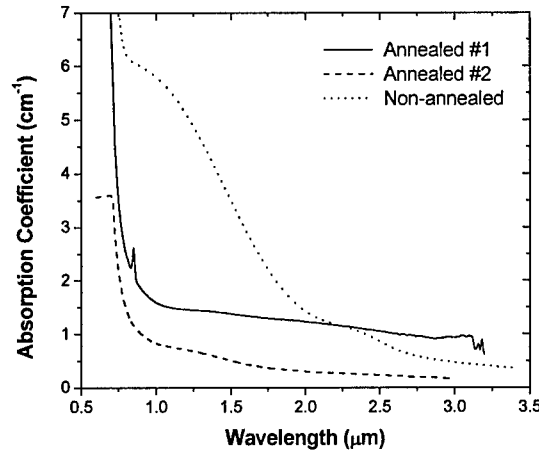

Fig. 1. Absorption spectra for three types of $ZnGeP_2$ crystals.

$ZnGeP_2$ is a positive uniaxial crystal with a point group of $\overline{4}2m$. It possesses a large second-order nonlinear coefficient ($d_{36} = 74$ pm/V) and figure of merit (d_{eff}^2/n^3) [1]. Although it

has a transparency range from 0.74 to 12 μm, a ZnGeP$_2$ crystal always has anomalously-large absorption coefficients in the near-infrared domain (1-2 μm) that are highly process-dependent, see Fig. 1 [1,2]. Recently it has been demonstrated that by annealing ZnGeP$_2$ the absorption coefficients can be dramatically reduced in this domain. As we mentioned above. we have chosen a ZnGeP$_2$ crystal for THz generation since its absorption coefficients in the THz domain are next to the lowest among many commonly-used nonlinear-optical crystals [3]. According to Fig. 2, the absorption coefficient for ZnGeP$_2$ at 200 μm is about 0.37 cm^{-1}. In comparison, for GaSe the absorption coefficient is about 0.14 cm^{-1} at the same wavelength. However, it is about 3 cm^{-1} for LiNbO$_3$. Perhaps, the simplest design based on ZnGeP$_2$ corresponds to 0°-cut. In our experiment, we used the ZnGeP$_2$ crystal which is 20.6 mm long along c axis, a cross-sectional area of 15 mm × 14 mm, and no antireflection coatings. The absorption coefficient of this ZnGeP$_2$ crystal is measured to be about 0.75 cm^{-1} at 1.064 μm (i.e. annealed #2 in Fig. 1). This is much lower than those used in our previous work [4] and a commonly-available crystal [3]. Indeed, the absorption coefficient is measured to be 5.63 cm^{-1} for the ZnGeP$_2$ crystal without performing any annealing process (i.e. non-annealed in Fig. 1). In our previous work on the annealed crystal (annealed #1 in Fig. 1) the absorption coefficient is measured to be about 1.52 cm^{-1} at 1.064 μm.
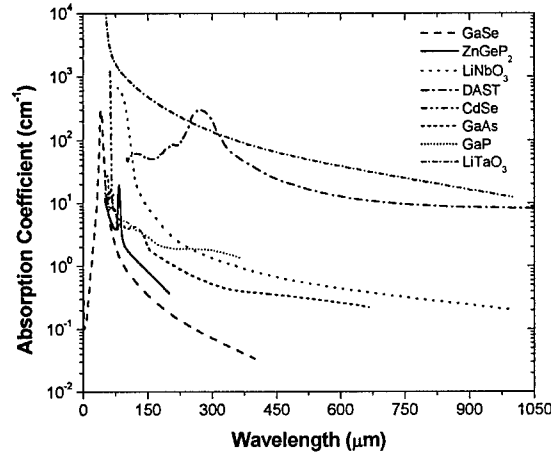

Fig. 2. Absorption coefficients vs. wavelength for some of commonly-available nonlinear crystals.

It can be readily shown that using the 1.064 μm as one of the pump wavelengths only the configurations of oe-e and oe-o can be phase-matched in a ZnGeP$_2$ crystal where the first and second letters designate the polarizations for the 1.064-μm and second (idler) pump beams while the third letter corresponds to the polarization for the THz beam, respectively. The corresponding phase-matching conditions can be written to be

$$\frac{n_o(\lambda_3)}{\lambda_3} - \frac{n_e(\lambda_2,\theta)}{\lambda_2} = \frac{n_e(\lambda_1,\theta)}{\lambda_1} \tag{1}$$

$$\frac{n_o(\lambda_3)}{\lambda_3} - \frac{n_e(\lambda_2,\theta)}{\lambda_2} = \frac{n_o(\lambda_1)}{\lambda_1} \tag{2}$$

where λ_3 = 1.064 μm, λ_2 is the wavelength of the idler beam, λ_1 is the THz wavelength, θ is phase-matching angle, and $n_e(\lambda, \theta)$ can be expressed as

$$n_e(\lambda,\theta) = \frac{n_o(\lambda)n_e(\lambda)}{[n_o^2(\lambda)\sin^2\theta + n_e^2(\lambda)\cos^2\theta]^{1/2}} \qquad (3)$$

In Eqs. (1-3), $n_o(\lambda)$ and $n_e(\lambda)$ are the principal indices of refraction for the ordinary and extraordinary waves at the respective wavelengths, determined by the Sellmeier equations written as follows [5]:

$$n_o^2(\lambda) = 4.47330 + \frac{5.26576\lambda^2}{\lambda^2 - 0.13381} + \frac{1.49085\lambda^2}{\lambda^2 - 662.55},$$

$$n_e^2(\lambda) = 4.63318 + \frac{5.34215\lambda^2}{\lambda^2 - 0.14255} + \frac{1.45795\lambda^2}{\lambda^2 - 662.55} \qquad (4)$$

One of the most important parameters for the efficient THz parametric conversion is the effective nonlinear coefficient. For the two configurations described above, the effective nonlinear coefficients depend on the phase-matching and azimuth angles (θ,φ) according to Ref. [1] as follows:

$$d_{eff}^{(oe-e)} = d_{36}\sin 2\theta\cos 2\varphi; \quad d_{eff}^{(oe-o)} = d_{36}\sin\theta\sin 2\varphi, \qquad (5)$$

where d_{36} is about 75 pm/V (Ref. [2]). Obviously $d_{eff}^{(oe-e)}$ reaches an optimized value at $\varphi = 0°$. On the other hand, $d_{eff}^{(oe-o)}$ reaches a maximum value at $\varphi = 45°$. As a result, by properly choosing different values of φ through crystal rotation we can select one of the two configurations. Such dependences of the effective nonlinear coefficient are indeed confirmed in our experiment. Moreover, the larger the angle θ, the larger the effective nonlinear coefficients. It is obvious that for the same angle θ, $d_{eff}^{(oe-o)}$ is lower than $d_{eff}^{(oe-e)}$. This is also confirmed in our experiment.
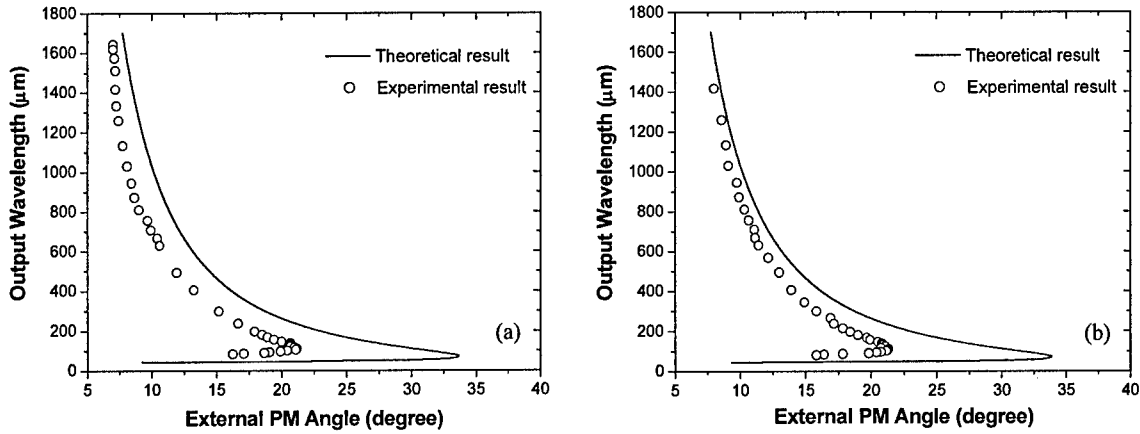

Fig. 3. (a) Collinear phase-matched DFG for oe-e configuration: THz output wavelength vs. external phase-matching angle. Open circles – data; solid lines – theory. (b) Collinear phase-matched DFG for oe-o configuration: THz output wavelength vs. external phase-matching angle. Open circles – data; solid lines – theory.

Our experimental setup is briefly described as follows. The idler beam, used as one of the pump beams for the DFG experiment, is generated by a master oscillator and then amplified by power oscillators. Both the master and power oscillators are pumped by the frequency-tripled beam from a pulsed Nd:YAG laser. This beam can be tuned in the range of 0.73–1.8 μm with a pulse duration of 5 ns and a repetition rate of 10 Hz. The residual Nd:YAG beam at the

wavelength of 1.064 μm with a pulse duration of 10 ns is used as the second pump beam. Two convex lenses are used to focus these two pump beams into the ZnGeP$_2$ crystal through a beamsplitter. An optical delay is used for the residual Nd:YAG beam to ensure that the two pump beams simultaneously arrive at the crystal. The beam spot size at the crystal ($1/e^2$ radius) is measured to be ~300 μm. The ZnGeP$_2$ crystal is mounted on a rotational stage. The generated THz waves are collected by two off-axis parabolic mirrors used as two lenses. They are separated from the pump beams by Ge and black polyethylene plates as filters and then focused onto a Si bolometer. The electrical signal outputted from the bolometer is in turn amplified and averaged in a boxcar integrator. The absolute value of the pulse energy corresponding to the generated THz wave radiation is calibrated by a pyroelectric detector.

We have first measured the angle-tuning characteristics for the oe-e DFG, see Fig. 3(a). The open circles correspond to the experimental results when the phase-matching condition is satisfied while solid curves correspond to the calculations by using the Sellmeier equations, Eq. (4) from Ref. [5]. It is important for us to point out that we have compared among three different Sellmeier equations from Refs. [5-7]. (For Ref. [7] only the dispersion for the ordinary wave is available.) It turns out that the theoretical results based on Eq. (4) produce the best fit to our experimental results. For each data point in Fig. 3(a) a phase-matching peak is achieved by optimizing the THz pulse energy through varying θ and one of the pump wavelengths. As a result, tunable and coherent output wavelengths in the range of 83.1–1642 μm (3.61-0.18 THz) [Fig. 3(a)] have been achieved. On the other hand, Fig. 3(b) illustrates the angle tuning for the oe-o configuration. In this case, tunable and coherent THz radiation in the range of 80.2–1416 μm (3.74-0.21 THz) has been achieved. These tuning ranges are much wider than that in Ref. [4]. On the long-wavelength side, the oe-e configuration produces the longer cut-off wavelength due to the different dependences of effective nonlinear coefficients on θ. Indeed, since is $d_{eff}^{(oe-e)}$ proportional to $sin2\theta$ it is larger than $d_{eff}^{(oe-o)}$ for the same value of θ, see Eq. (5). On the other hand, on the short-wavelength side, the cut-off wavelength for the oe-o configuration is shorter. This is primarily due to the fact that the absorption for the ordinary wave in the oe-o configuration is lower than that for the oe-e configuration near 80 μm, see Ref. [3]. The theoretical and experimental phase-matching curves significantly deviate from each other over the entire two ranges of the output wavelengths. These discrepancies are due to the fact that the theoretical curves are obtained by using the Sellmeier equations for the un-annealed ZnGeP$_2$ crystal.[17] These equations provide the best fit to our data. Based on the measured absorption coefficients of the un-annealed and annealed ZnGeP$_2$ crystals mentioned above, however, we conclude that although the absolute values for the refractive indices for these two types of the crystal are close to each other near 1.064 μm the dispersions around this wavelength can be quite different from each other. Since the phase-matching angles primarily depend on the index dispersions, especially for the THz generation, the angles are significantly changed for the annealed crystal. On the other hand, since the wavelength for the THz wave is so long the dispersion in this domain has negligible effect on the phase-matching angles. Therefore, the Sellmeier equations obtained previously are not accurate enough for the annealed ZnGeP$_2$. Based on Figs. 3(a) and 3(b) it is obvious that an annealed ZnGeP$_2$ crystal is more advantageous than the conventional one since the measured phase-matching angles are much smaller.

For the Nd:YAG pump intensity of 17 MW/cm^2 and OPO pump energy of 2.5 mJ, the output peak powers at different output wavelengths are also measured for the oe-e and oe-o configurations, see Fig. 4. For the pump intensity of under 20 MW/cm^2, there is no apparent

surface damage for the annealed ZGP crystal. The measured THz radiation has the pulse duration of 5 ns and a repetition rate of 10 Hz. The highest output peak power for the THz can reach 133.8 W at 237 μm (1.27 THz) for the oe-e and 90 W at 196 μm (1.53 THz) for the oe-o configuration. These peak powers are much higher than what we obtained recently [4]. The peak power for the oe-e configuration is much higher than that for the oe-o configuration since $d_{eff}^{(oe-e)}$ is larger than $d_{eff}^{(oe-o)}$, see Eq. (3). Therefore, it is obvious that the oe-e configuration has an advantage over the oe-o configuration since the corresponding peak power is higher. In addition, the oe-o configuration produces longer wavelengths. On the other hand, the oe-o configuration has an advantage of generating shorter wavelengths. In our experiments we have consistently observed two dips near 110 μm (see Fig. 4). This is consistent with a similar peak appearing in the previous absorption spectrum [3].
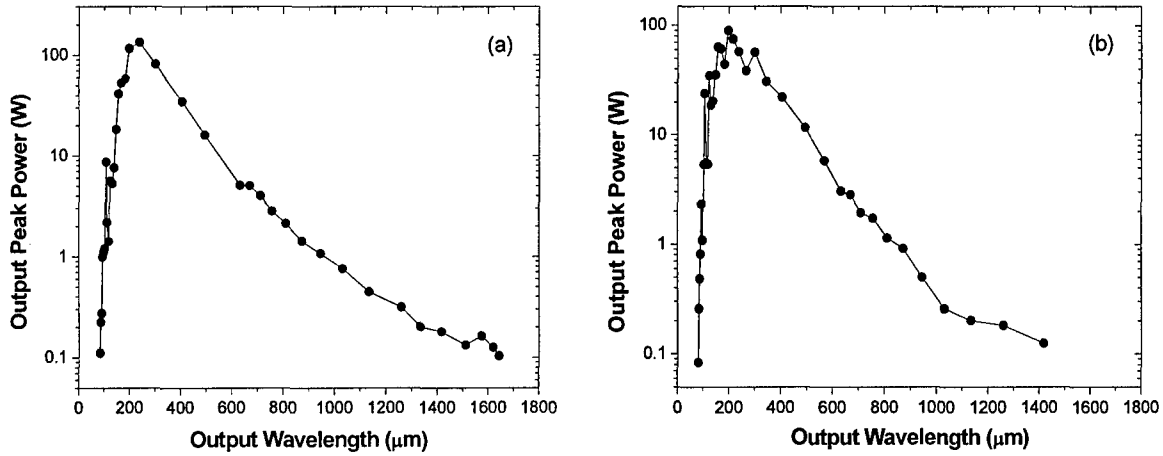

Fig. 4. THz output peak power vs. output wavelength: (a) oe-e configuration and (b) oe-o configuration.

For the highest output peak powers mentioned above the energy conversion efficiencies are measured to be 0.037% and 0.026% for the oe-e and oe-o configurations, respectively. Consider the collinear phase-matched DFG. Assume two Gaussian pump beams with the same beam radius and no diffraction effect. The conversion efficiencies, defined as $\eta=P_1/P_2$, where P_1 and P_2 are the peak powers for the THz and idler beams, respectively, can be calculated by using the following formula (Ref. [8]):

$$\eta = \frac{4\pi^2 d_{eff}^2 L^2 P_3}{\varepsilon_0 c n_1 n_2 n_3 \lambda_1^2 A_3}$$ (6)

where L is the crystal length, λ_1 is the output wavelength, P_3 is the peak power for the 1.064-μm beam, n_1, n_2, and n_3 are the indices of refraction for the THz, idler, and 1.064-μm beams, respectively, c is speed of light in vacuum, ε_0 is the permittivity constant, d_{eff} is the effective nonlinear coefficient introduced above, and A_3 is the cross-sectional area of the 1.064-μm beam defined by the $1/e^2$ radius of the Gaussian beam. Using the equation above, the conversion efficiencies are calculated to be 0.048% and 0.039%, respectively. Therefore, the measured values are in very good agreements with the theory.

Our results demonstrate that ZnGeP$_2$ is another nonlinear crystal that can be used for efficient generation of widely-tunable monochromatic THz waves.

These results were published in Appl. Phys. Lett. (2003) and Opt. Commun. (2004).

1. V. G. Dmitriev, G. G. Gurzadyan, and D. N. Nikogosyan, *Handbook of Nonlinear Crystals* (Springer, Berlin, 1999).
2. P. D. Mason, D. J. Jackson, and E. K. Gorton, Opt. Commun. **110**, 163-166 (1994).
3. E. D. Palik, *Handbook of optical Constants of Solid* (Academic, New York, Vol. III, 1998).
4. W. Shi and Y. J. Ding, Appl. Phys. Lett. **83**, 848-850 (2003).
5. G. C. Bhar, L. K. Samanta, D. K. Ghosh, and S. Das, Sov. J. Quantum Electron. **17**, 860-861 (1987).
6. D. E. Zelmon, E. A. Hanning, and P. G. Schunemann, J. Opt. Soc. Amer. B **18**, 1307-1310 (2001).
7. G. D. Boyd, T. J. Bridges, C. K. N. Patel, and E. Buehler, Appl. Phys. Lett. **21**, 553-555 (1972).
8. A. Yariv, *Quantum Eletronics* (Wiley, New York, 1988).

7. Measurement of absorption spectrum on air in THz region

Our widely-tunable THz source can be used to identify chemicals. To demonstrate this, as the first step we have made preliminary measurements of the absorption spectrum of air. Indeed, as one can see from Fig. 1, every peak can be clearly resolved. This result is similar to Ref. [1]. On the contrary, all the transitions are congested in the mid-IR and IR domains. To some extent, this result illustrates that the absorption spectrum can be used to identify each type of the molecules similar to the identification of each person through the fingerprint. In the future, we will also measure the absorption spectra of the other chemical species to demonstrate that the absorption peaks in the THz can be, indeed, used to identify chemical species.
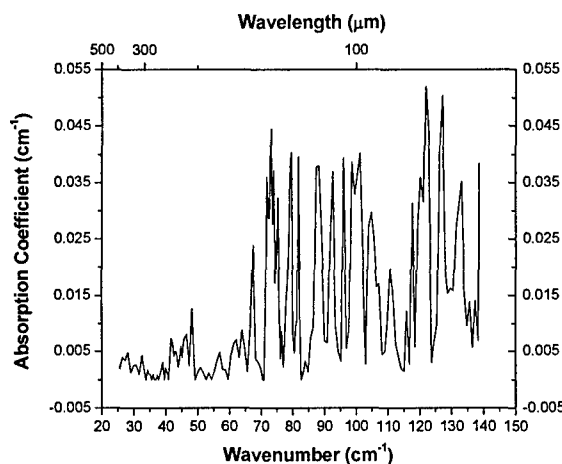

Fig. 1. Absorption spectrum for the air, for a beam pass of 15 cm, humidity of 34%, temperature of 74 °F, and pressure of 1 atm. This important result illustrates that the unique and sharp transition peaks for gases can be obtained from the direct measurements of the absorption spectra. Some of these peaks may be due to the weak interactions between N_2 or O_2 and H_2O.

These results were included in Laser Phys. Lett. (2004).

1. F. C. De Lucia, Opt. Photon. News **14**, 44 (2003).

8. Design, fabrication, and characterization of photonic bandgap crystals in THz

THz spectroscopy as a method for detection of chemical and biological agents has its own advantage. One advantage is based on the fact that each type of the molecules has its own distinct signature in the absorption spectrum. THz spectroscopy can be used to create "fingerprint" for individual molecules. For example, H_2S, NH_3, O_3, SO_2, HCN, and H_2O have extremely-sharp transition lines at 225.3 μm, 301.3 μm, 313.60 μm, 349.1 μm, 372.5282 μm, and 220.2279 μm, respectively. Sensitivities for measuring these substances based on the THz

absorption spectroscopy can be very high due to the presence of these sharp and unique transitions.

A second advantage is based on the fact that both the sensitivity and selectivity of any detection process can be greatly enhanced by exploiting the resonant phenomena in time and space. When the frequency of radiation of interest is close to the temporal resonance (i.e. close to the frequency of the absorption line) or to the spatial resonance (resonance of the cavity, for instance) the amplitude of the response gets enhanced by a Q-factor of the resonance which can be very high. Away from the resonance the response decays with a rate also proportional to the Q. If the resonance frequencies can be tuned, very sensitive and versatile sensing devices can be built. One can take advantage of the stunning advances in nanofabrication to develop high-Q structures with resonances in the THz region of the spectrum. These resonant structures will include resonant emitters and detectors based on novel structures of quantum dots as well as photonic bandgap structures. In our opinion, it is precisely the THz region where the resonant structures with the highest possible Q's can be realized. Consider the temporal resonance, i.e. the resonance between two levels in quantum dots. The transition frequency is smaller than the frequency of longitudinal-optical phonons (~10 THz) thus the main linewidth-broadening mechanism is effectively blocked resulting in high Q. Thus highly-resonant and narrow-linewidth sources and detectors can be built.

When it comes to exploiting the resonance in the spatial domain, one would want to take advantage of the PBC's and their unusual properties. Of course, PBC's have been proposed and demonstrated in a number of spectral regions both above and below the THz range, but, we strongly believe, that it is within the THz range where the PBC's can be most beneficial. Indeed, in the visible/near-IR range the size of the feature of the PBC must be about a quarter wavelength of light in the medium – this cannot be achieved using traditional fabrication methods. Furthermore, the tolerances of fabrication should be much smaller than the wavelength, i.e. of the order of nanometers, or suffer from a very low Q. In the microwave range, on the other hand, the PBC can be easily realized, but its size becomes very large – in order to attain D-dimensional PBC with high Q the number of elements in the PBC should be at least Q^D. For the centimeter waves one needs structures of at least about 10 cm long and wide. Now, if one considers 100-μm radiation, and the refractive index of the order of 4, the typical size of the PBC feature is about 5-10 μm and the tolerances are of the order of 100 nm – quite attainable with today nanofabrication methods. The total size of the structure is of the order of a few hundred μm to mm – i.e. it can be integrated on one chip. Furthermore, the high index contrast in the THz range is easily available in a number of material combinations, including the most common group IV and III-V semiconductors.

Finally, the all-important feature of all the resonances described here is that they can be easily tailored to any wavelength in the wide range by varying the size of the features. Moreover, their resonances can be tuned by applying external fields (albeit not in a very wide region). Thus we can produce the custom-made chemical sensors that can be further fine-tuned for the best performance towards a particular chemical.

During the last 12 months, as the first step we have designed and fabricated distributed Bragg reflectors (DBR's) based on multiple Si/Air interfaces (i.e. 1-D photonic bandgap crystals). Our estimates show that for the two air slots surrounded by three Si bridges, the peak reflectivity is about 99.75% at 1 THz. The total amount of the absorption is negligible. At the 1-THz frequency, the required width for the Si and air slot is about 21.96 micrometers and 75 micrometers. The above results clearly illustrate the advantage of using the periodic air slots over

the alternating Si/Ge or GaAs/GaP layers: only two air slots are needed to produce a photonic bandgap! The process of fabricating our DBR's is quite simple. On each of the 0.3-mm-thick semi-insulating Si wafers, we used UV laser pulses (ns long) to "drill" three rectangular apertures, see Fig. 1. Since the Si wafers are quite thin, we have vertically stacked 3-4 DBR's to increase the signal/noise ratio. For our initial study we have three structures:

1 $d_1 = 29.28$ μm, $d_2 = 100$ μm, $d_3 = 2000$ μm
2 $d_1 = 43.92$ μm, $d_2 = 150$ μm, $d_3 = 2000$ μm
3 $d_1 = 50.85$ μm, $d_2 = 175$ μm, $d_3 = 2000$ μm.
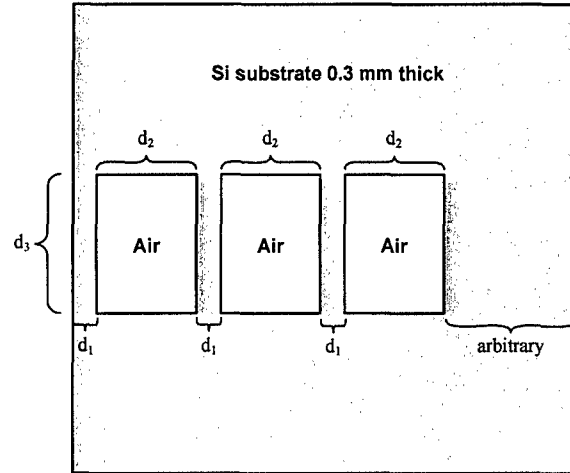

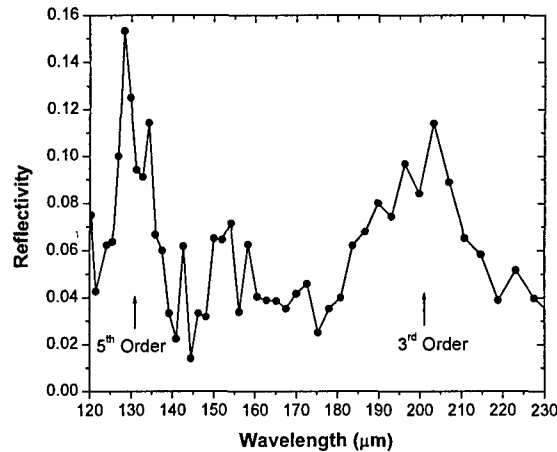Fig. 1. Structure of distributed Bragg reflectors in THz region.

Fig. 2. Reflectivity is measured vs. wavelength. Right and left arrows mark locations of third and fifth orders of distributed Bragg reflection.

Our measurements show that the ns UV laser is not the best source for such a type of the fabrication. We have consistently had difficulties to precisely fix the thickness of the Si walls (d_1). It seems to us the fabricated wall thicknesses deviate from our designed values by as large as ±5 μm. In addition, each aperture has a "taper" in the amount of 1-3 degrees (half angle). All these problems are reflected on the reflection spectra of the DBR's as significantly-shifted and broadened peaks. Fig. 2 shows our typical result of the measurement of the reflection spectrum

on the structure #3. One can clearly see the two peaks marked as the third and fifth orders of the distributed Bragg reflection. The corresponding peaks in the reflection spectra for the other two structures are somewhat less pronounced due to the fact the thickness fluctuations of the Si walls have more severe effects on the structures #1 and 2 due to their smaller wall thicknesses.

Some of these results were included in SPIE Proc. (2005).

9. Observation of strong backward THz wave by mixing two infrared laser beams

In this section, we summarize our results on the observation of a backward THz wave by mixing two infrared laser beams in a GaSe crystal, which is one step closer to backward parametric oscillation.
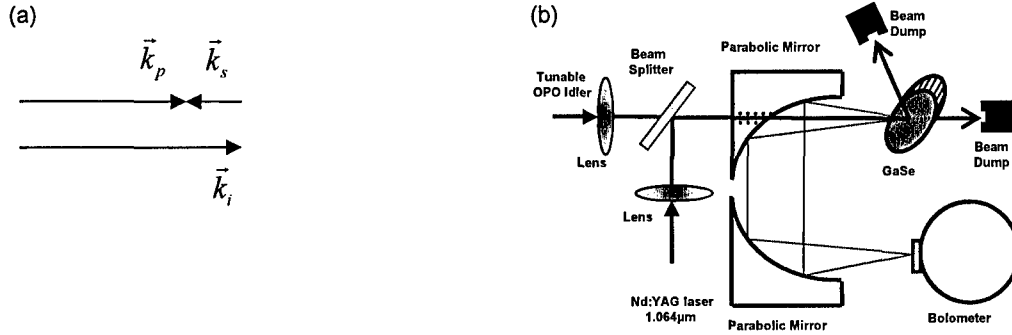

Fig. 1. (a) Wave vectors of three parametric waves that satisfy phase-matching condition: $\vec{k}_p = \vec{k}_s + \vec{k}_i$. In addition, $\omega_p = \omega_s + \omega_i$. In our experiment, $\vec{k}_s$ corresponds to the wave vector for the THz wave. (b) An experimental setup for observing backward phase-matched DFG in a GaSe crystal.

One of the parametric processes in nonlinear optics, yet to be demonstrated, is backward optical parametric oscillation (OPO), i.e. one of the parametric waves propagates in a direction opposite to that for the pump wave, see Fig. 1(a). Such a fundamentally important scheme was proposed in 1966 [1]. A backward OPO has a major advantage over the forward one (i.e. all three parametric waves propagates in the same direction): Since the signal and idler waves counter-propagate in a nonlinear medium, an oscillation can occur without even a mirror, whereas the forward OPO cannot oscillate without a cavity for the signal. However, owing to the fact that one of the parametric waves has its wave vector opposite to those of the other two waves, the phase-matching condition places a tough requirement on the dispersion of the nonlinear-optical crystal. Although the quasi-phase-matching can be an alternative, the period required to achieve a backward OPO in the mid-IR domain [2] is beyond the fabrication capability. Furthermore, a backward OPO intrinsically has a threshold that is much higher than that for a forward OPO. Our recent theoretical analysis [3] shows that the THz domain may be one of the best regions for observing a backward parametric oscillation. This is because the magnitude of the wave vector for the THz wave is much smaller than those in the infrared. As a result, the backward phase-matching condition can be more readily satisfied. The implementation of a backward parametric oscillation in the THz domain is not only fundamentally important in nonlinear optics, but also impacts its applications in the THz field. Indeed, due to the absence of a cavity, the output frequencies can be easily tuned in a large range without the presence of the cavity-induced instabilities.

To efficiently generate a backward wave in the THz region, we have calculated the phase-matching characteristics for all the nonlinear-optical crystals known to us. There are a few issues

to consider. First, the effective nonlinear coefficient should be as large as possible for the short-wavelength side of the THz wave. This is important since the threshold for the backward parametric oscillation rapidly increases as the THz wavelength increases. Second, the other competing effects such as two-photon absorption, free-carrier absorption, and nonlinear refractive index should not be strong enough to increase the threshold. Third, the crystal must be transparent enough such that a long interaction length can be maintained. As a result, we have chosen GaSe as our optimum nonlinear-optical crystal for our experiment [3].

According to our calculation, phase matching can be achieved for type-*eo-e* backward difference-frequency generation (DFG) in GaSe. The effective nonlinear coefficient is given by $d_{eff} = d_{22} \cos^2\theta \sin3\phi$, where d_{22}=52.8 pm/V. In order to optimize d_{eff}, $\phi = 0^0$ such that $\cos3\phi = 1$, which was confirmed in our experiment. Our experimental setup is schematically shown in Fig. 1(b). One pump beam is from the output of a Nd:YAG laser beam (1.064 μm) with a pulse duration of 10 ns, a pulse energy of 3 mJ, and a repetition rate of 10 Hz. The second pump beam is the idler beam of a β-BaB$_2$O$_4$–based OPO pumped by the third harmonic of the Nd:YAG laser, with a duration of 5 ns, a pulse energy of 3.5 mJ, and a repetition rate of 10 Hz. In front of the GaSe crystal we placed an an off-axis parabolic metallic mirror on which a 1.5-mm hole was drilled to allow the two pump beams to pass through it. The generated backward THz waves were collected by two off-axis parabolic metallic mirrors and focused onto a Si bolometer. The THz signal was then averaged by a boxcar and monitored by a digital oscilloscope. It is worth noting that to collect the generated THz signal a set of the spectral filters for blocking the pump beams are not required any more in this backward configuration since there are no residual pump beams propagating along the propagation direction of the THz wave. In our experiment, we used a 7-mm-long z-cut GaSe crystal with a 35 mm×15 mm elliptical aperture.
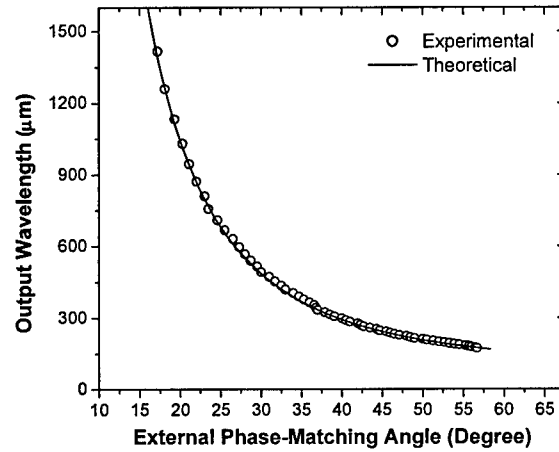

Fig. 2. Angle-tuning characteristics for the type-*eo-e* backward THz DFG.

Fig. 2 shows the external PM angular tuning curves for the type-*eo-e* backward DFG. The open circles in Fig. 2 correspond to our experimental results while the solid curve illustrates the theoretical result obtained by using the phase-matching condition. We observed the phase-matching peaks by varying the angle (θ) and the wavelength of the idler pump beam. The generated THz wavelengths were verified by a scanning THz etalon, which precisely coincided with the difference frequencies between the two pump beams. From Fig. 2, one can see that a tunable and coherent THz wave propagating in the backward direction, in the wide range of

172.7-1416.7 μm (0.212–1.74 THz), was achieved based on the phase-matched DFG in GaSe. In addition, our experimental results are in an excellent agreement with our calculations for the type-*eo-e* backward DFG, see Fig. 2. In order to verify that the above THz output is due to the backward DFG, we measured the THz signal behind the GaSe crystal, as shown in Fig. 1. A very weak THz signal was detected when the THz signal measured before the crystal was the strongest. We believe that the measured weak signal behind the crystal was just a reflection of the backward THz wave. According to our calculations, the forward DFG cannot be phase-matched for the type-*eo-e* or type-*eo-o* configurations in a GaSe crystal.
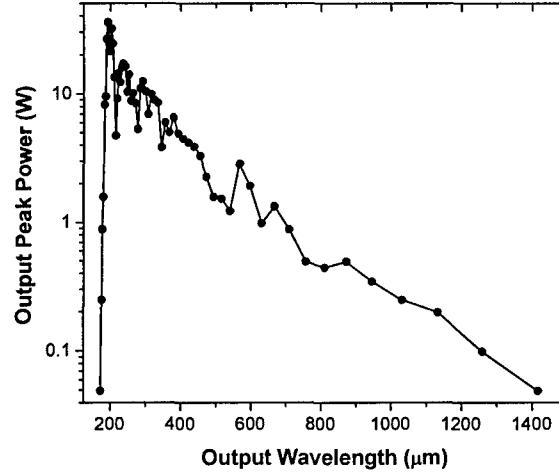

Fig. 3. The THz output peak power is measured vs. the output wavelength for the type-*eo-e* phase-matched backward DFG in a GaSe crystal.

The backward THz output powers were measured by using the Si bolometer calibrated by a pyroelectric detector in terms of pulse energies. Fig. 3 is the plot of the measured output peak powers vs. the different output wavelengths for the type-*eo-e* backward DFG in the GaSe crystal. According to Fig. 3, one can see that the highest output peak power is 35.7 W at 193 μm, which corresponds to a power conversion efficiency of 0.0051%. Such an output power is significantly higher than that for the forward configuration with the about same conversion efficiency [4]. Furthermore, in the output range from 180 μm to 690 μm, the output peak power can always be kept at the level of above 1 W.

In summary, we have observed a backward THz wave by efficiently mixing the two pump beams in the infrared range. The generated coherent THz radiation can be tuned from 172.7 μm to 1416.7 μm. In addition, the highest output peak power is 35.7 W at the wavelength of 193 μm, which corresponds to a conversion efficiency of 0.0051%. Even much higher output powers can be obtained. According to the absorption coefficient of GaSe at 193 μm, the output peak power can be as high as 3.5 kW is possible using a longer GaSe crystal. Such a peak power can be tightly focused down to produce a peak intensity of 12×10^6 W/cm^2, which is sufficiently high for us to uncover a class of novel nonlinear effects in the THz domain in the future.

These results were included in Opt. Lett. (2005) and J. Nonlinear Opt. Phys. & Mats. (2003).

1. S.E. Harris, "Proposed backward wave oscillation in the infrared," *Appl. Phys. Lett.* **9**, 114-116 (1966).

2. Y. J. Ding and J. B. Khurgin, "Backward optical parametric oscillators and amplifiers," *IEEE J. Quant. Electron.* **32**, 1574-1582 (1996).
3. Y. J. Ding and I. B. Zotova, "Coherent and tunable terahertz oscillators, generators, and amplifiers," *J. Nonlinear Opt. Phys. & Mats.* **11**, 75-97 (2002).
4. W. Shi, Y. J. Ding, N. Fernelius, and K. Vodopyanov, "Efficient, tunable, and coherent 0.18-5.27-THz source based on GaSe crystal," Opt. Lett. **27**, 1454-1456 (2002).

10. Efficient THz generation in a cubic crystal

In this section, we highlight our results on the efficient generation of THz waves continuously tunable in the range of 84–1134 μm in a cubic crystal, GaP, based on collinear quasi-phase-matched difference-frequency generation. The highest peak power is 15.6 W at 173 μm.

Parametric processes in nonlinear optical (NLO) crystals represent an efficient method for the generation of coherent and monochromatic THz radiation [1,2]. In order to achieve phase-matching, birefringence is usually necessary. The disadvantage for the birefringence-based phase-matching is the necessity of rotating NLO crystals as demonstrated in Refs. [1,2]. Recently, we showed [3] that for cubic NLO crystals such as GaAs and GaP, phase-matching can still be achieved for particular sets of the three parametric wavelengths. For example, for GaP the pump wavelength for producing a THz wave at 300 μm is calculated to be 1.03 μm for the phase-matched difference-frequency generation (DFG) [3]. Besides GaSe and $ZnGeP_2$ crystals, GaP is attractive since it has large second-order NLO coefficients and low absorption coefficients in the THz region [4]. Furthermore, GaP has very low two-photon absorption coefficients. Although there have been some reports of using GaP crystals for the efficient THz generation under a *noncollinear* phase-matched condition [5], the tuning ranges are narrow. Furthermore, the output peak power is too low to be practical. Indeed, among all the previous results based on GaP the widest tuning range and highest peak power achieved so far are 42.8-600 μm and 100 mW, respectively. Here, we report our first result of achieving the THz radiations by using *collinear* quasi-phase-matched DFG in a GaP crystal. We have extended the THz output wavelengths to as long as 1134 μm. In addition, the peak power can now reach 15.6 W. Since GaP is a cubic crystal, we do not need to rotate the crystal for tuning the output wavelength.
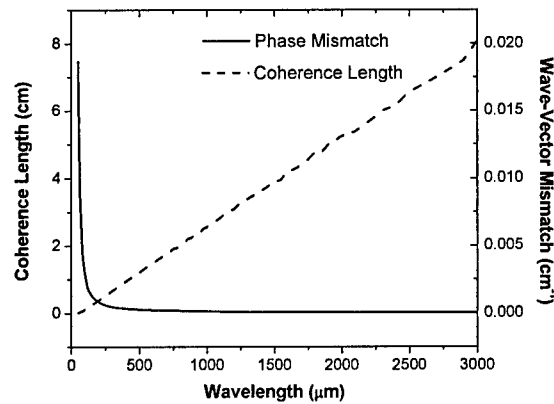

Fig. 1. Coherence length and wave-vector mismatch vs. wavelength for GaP at pump wavelength of 1.064 μm.

In our experiments, the two mixing beams used for the DFG consist of an idler beam (0.73–1.8 μm) from a BBO-based master oscillator/power oscillator pumped by a frequency-

tripled Nd:YAG laser and the residual Nd:YAG beam (1.064 μm). The Nd:YAG laser pulses have a pulse duration of 10 ns and a repetition rate of 10 Hz. A GaP crystal with the dimensions of 19.9 mm in length (along [001]), 25 mm in width, and 25 mm in height was used. According to our calculation, collinear DFG for THz generation can only be phase-matched when the pump wavelength is in the range of 0.995-1.033 μm for the output wavelengths in the range of 90-1000 μm. If the pump wavelength is longer than 1.033 μm, the phase-matching is not possible. In this case, however, the quasi-phase matching is still possible. Indeed, at 1.064 μm the coherence length linearly increases as the output wavelength increases, see Fig. 1. When the output wavelength is higher than 780 μm the coherence length is longer than the GaP thickness (19.9 mm). In this case, the length of the crystal is on the same order of magnitude as the coherence length for the DFG. Therefore, we define that such a DFG process is "quasi-phase-matched". In our experiments, the generated THz radiation was measured by a bolometer and then amplified and averaged in a boxcar integrator. Consider the two polarization configurations: the polarizations of the two input beams are parallel to [100] (*parallel*) and orthogonal to each other with one of them along the crystal axis in the GaP crystal (*orthogonal*). Fig. 2 (a) and (b) show the angle-tuning spectra measured by us at different output wavelengths for both the parallel and orthogonal configurations, respectively. The highest THz output powers at the different THz wavelengths all occur at the external angles of about 62° and 53° for the parallel and orthogonal polarizations, respectively. Because the GaP crystal is isotropic in terms of its linear optical properties, these dependences of the output powers on the external angles are originated from the angle dependences of the effective nonlinear coefficients.
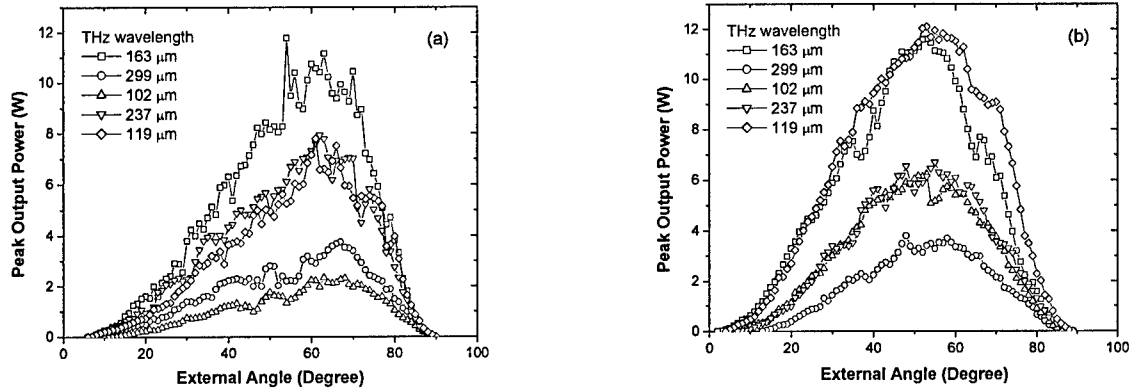

Fig. 2. Peak output power vs. external incident angle when pump beam polarizations are (a) parallel and (b) orthogonal to each other.

The output peak power was measured vs. output wavelength for the two input polarizations, see Fig. 3. For the parallel and orthogonal polarizations, we have set the incident angles to be 62° and 53° to achieve the highest output peak powers in our experiments following Fig. 2. One can see that we have achieved coherent THz radiation widely tunable in the range of 84–1134 μm (0.26-3.57 THz) for the parallel polarizations and 83–810 μm (0.37-3.61 THz) for the orthogonal polarizations in the GaP crystal. Although these ranges are not as wide as those obtained by us by using GaSe, they are the widest tuning ranges ever achieved by using the GaP crystal based on the parametric processes. As we mentioned above the widest tuning range achieved before is only 42.8-600 μm based on GaP [5]. Since GaP is a cubic crystal, our tuning ranges were achieved without rotating the GaP crystal. This can be an advantage for the

application of our THz source in spectroscopy and chemical identification. In those cases, we can just tune one of the two pump wavelengths in order to tune the output wavelength in a wide range.
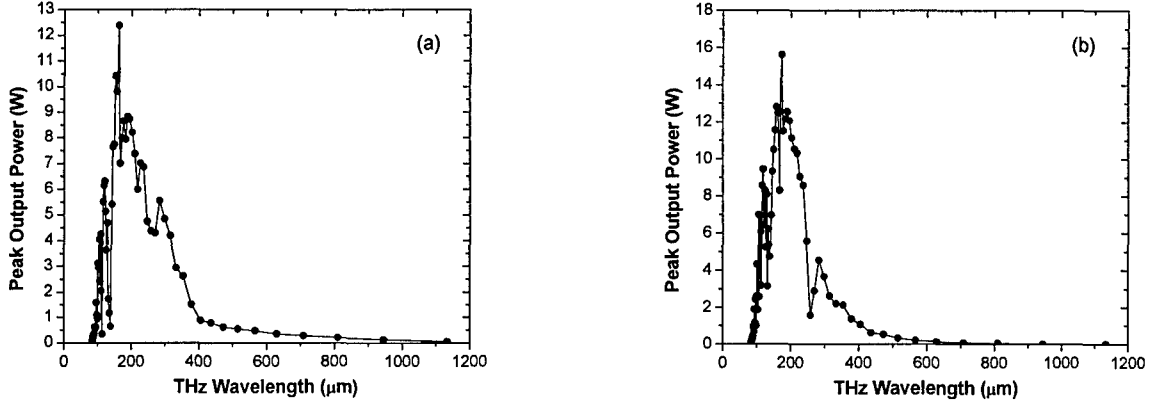

Fig. 3. Output power vs. wavelength when input polarizations are (a) parallel and (b) orthogonal to each other.

For the parallel polarizations the highest output peak power of 12.4 W at 163 μm has been obtained by us, with the corresponding conversion efficiency of ~ 0.0016%. On the other hand, for the orthogonal polarizations the highest output peak power of 15.6 W at 173 μm has been achieved, with the corresponding conversion efficiency of ~ 0.002%. The highest peak power achieved in our experiments is a factor of 156 higher than the previous result [5]. Furthermore, compared with GaSe [1] and ZnGeP$_2$ [2], GaP has another advantage of producing relatively higher output powers at shorter wavelengths. Finally, we would like to point that several dips appearing in the curves of Fig. 3 are primarily due to the absorption of water vapor in air and on the GaP surface.

In summary, by using a GaP crystal based on quasi-phase-matched DFG, we have achieved widely-tunable, monochromatic and coherent THz radiations in the range of 84–1134 μm for the parallel polarizations of the two mixing beams and 83–810 μm for the orthogonal polarizations. By using a collinear configuration, we have greatly increased the tuning ranges for the output wavelength and output peak powers. Compared with other NLO crystals, GaP offers an obvious advantage for tuning the output wavelength since one does not need to rotate the GaP crystal. Moreover, since the phase-matched pump wavelengths for GaP are the same as the output wavelengths from an Yb-doped fiber laser, we will be able to eventually implement a compact THz source pumped by Yb-doped fiber lasers.

These results were published in J. Nonlinear Opt. Phys. & Mats. (2006) and Opt. Lett. (2005).

1. W. Shi, Y. J. Ding, N. Fernelius, and K. Vodopyanov, "Efficient, tunable, and coherent 0.18-5.27-THz source based on GaSe crystal," Opt. Lett. **27**, 1454-1456 (2002).
2. W. Shi and Y. J. Ding, "Continuously tunable and coherent terahertz radiation by means of phase-matched difference-frequency generation in zinc germanium phosphide," Appl. Phys. Lett. **83**, 848-850 (2003).
3. Y. J. Ding and I. B. Zotova, J. Nonlinear Opt. Phys. & Mats. **11**, 75 (2002).
4. E. D. Palik, *Handbook of Optical Constants of Solids* (Academic, New York, 1998), Vol. III.
5. T. Tanabe, K. Suto, J. Nishizawa, K. Saito, and T. Kimura, "Tunable terahertz wave generation in the 3- to 7-THz region from GaP," Appl. Phys. Lett. **83**, 237-239 (2003).

11. Optimization, fabrication, and characterization of THz Bragg reflectors

In this section, we report our results of the first attempt to design, fabricate, and characterize THz Bragg reflectors (i.e. 1-D PBC's) on Si wafers. We have demonstrated that even just for three air slots, we have achieved the reflectivity as high as 91%, which is already high enough to be used as an output coupler for a taser. Furthermore, we have also measured the spectrum of the reflectivity and then compared it with our calculations.

THz waves can be generated based on several schemes such as tasers (similar to lasers, but in the THz region) [1], optical rectification [2], photoconduction [3], and parametric processes [4]. Tasers may eventually replace other techniques for certain applications due to their compact size and convenient pumping via current injection. Recently, it has been shown that transitions between light-hole and heavy-hole subbands based on Ge_xSi_{1-x} structures appear to be quite promising for achieving a taser [5]. However, it has been quite challenging to design and fabricate THz output couplers in the past, which are indispensable to tasers. Another potential application for THz mirrors is the possibility of constructing a cavity for THz waves such that the conversion efficiency for parametric processes can be greatly enhanced. If 2-D photonic bandgap crystals (PBC's) in the THz region are available, similar to other microwave and optical ranges [6], even more important applications such as chemical sensors can be realized by e.g. incorporating Si or GaAs emitters and detectors all into the PBC's.
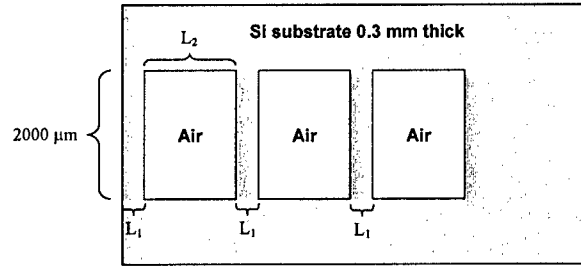

Fig. 1. Structure of Bragg reflector fabricated by drilling periodic air slots on semiconductor wafer.
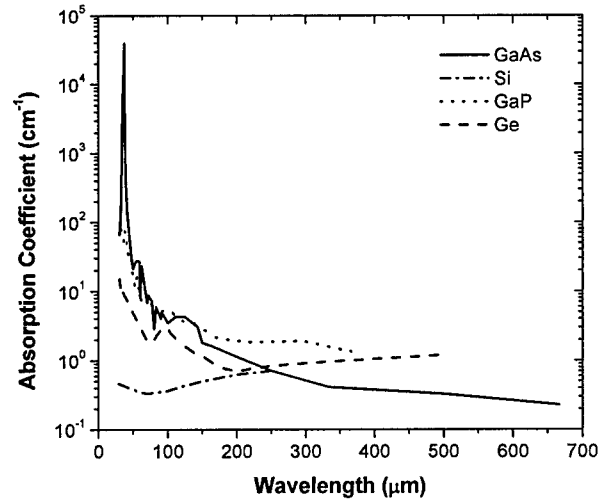

Fig. 2. Absorption coefficient vs. wavelength for four semiconductor materials.

Conventionally, most of the Bragg reflectors have been made by using two alternating materials such as GaAs and AlAs to form a quarter-wave stack. In order to achieve a high

reflectivity, a few tens of pairs are required. Our Bragg reflector consists of periodic air slots fabricated on a Si wafer, see Fig. 1. Among the common semiconductor materials, Si is attractive since it has much lower absorption coefficients for the wavelengths below 250 μm, see Fig. 2. Since the index of refraction for Si in the THz region is quite high (3.49), we only need a few air slots to achieve an extremely high reflectivity at the Bragg condition. Indeed, even just using two air slots the reflectivity at 1 THz can reach 99.75%. The required lengths for the Si and air slot are estimated to be about 21.96 μm and 75 μm, corresponding to the quarters of the THz wavelengths in the Si and air, respectively. Such dimensions can readily be achieved by using a few common techniques such as chemical etching, deep reactive ion etching, and laser drilling. We have chosen laser drilling due to its simplicity. Indeed, using such a method we do not need to design and fabricate a mask. The Bragg reflector can be fabricated directly on the Si wafer. Therefore, such a technique can be quite attractive for fabricating an output coupler for a taser. In order to fabricate the Bragg reflectors we have used a UV laser to drill the air slots. In this case, the UV laser pulse is converted to heat upon irradiance on a Si wafer. Consequently, the temperature rise at the irradiated area is sufficiently high to melt that part of the Si wafer. Using this method a typical taper of 1-3° and fluctuation of the Si bridge on the order of ±5 μm are expected.
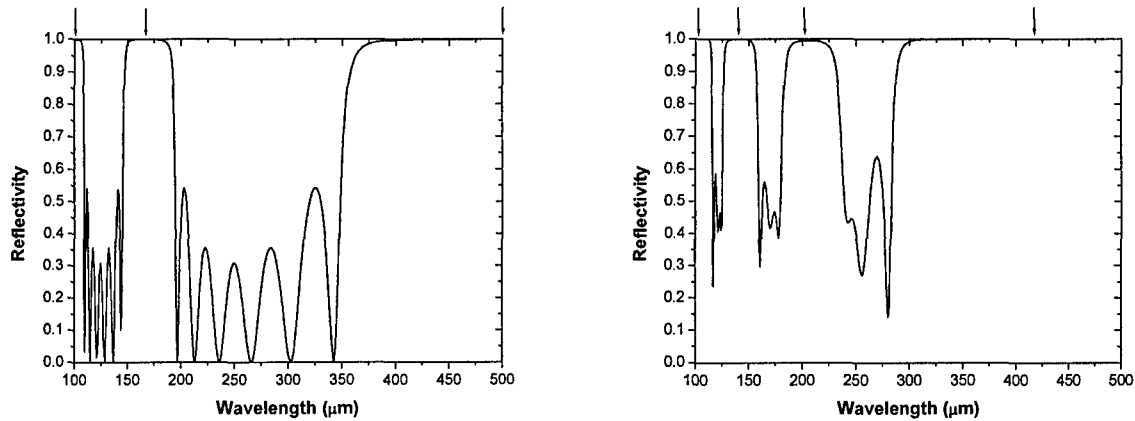
Fig. 3. Calculated reflectivity vs. wavelength for lengths of Si bridge and air slot to be 36.6 μm and 125 μm. Left: normal incidence; right: incident angle of 46.5°. Arrows mark locations of all peaks.

There is another advantage for the Bragg reflector implemented based on the Si/air interfaces: The bandwidth for the lowest-order Bragg reflection is much broader than that based on the two alternating materials having much closer values of the indices of refraction. According to Fig. 3 for the three air slots with the lengths of the Si bridge and air slot to be 36.6 μm and 125 μm, respectively, the 1st order Bragg reflection occurs at 500 μm. The half of the bandwidth defined at the point where the reflectivity is reduced to 90% is as wide as 142 μm. In addition, due to the phase shift of π for the wave propagating in the air reflected by each Si surface, all even orders vanish in the reflection spectrum, see Fig. 3. When the incident angle is large enough, however, the spectrum looks strikingly different, see Fig. 3. For such a case the peak wavelength for the 1st order Bragg reflection occurs at 418 μm instead of 500 μm. In addition, there are four Bragg peaks instead of the three at the normal incidence.

Typically it is quite difficult for us to drill deep air slots by using the UV laser due to the temperature gradient along the propagation direction of the laser beam. Therefore, the thickness

of the wafers we have used for the Bragg reflectors is only about 300 μm. For such a thickness, as shown by us previously [7] the THz wave is actually confined by the waveguide with a modal index. However, using an off-axis parabolic mirror it would be quite difficult for us to couple the incoming THz wave into the waveguide with a high coupling efficiency. Therefore, to avoid the waveguiding effect we have stacked three Bragg reflectors with almost the same structure. This way, we can also increase the reflectivity for the incident THz wave.
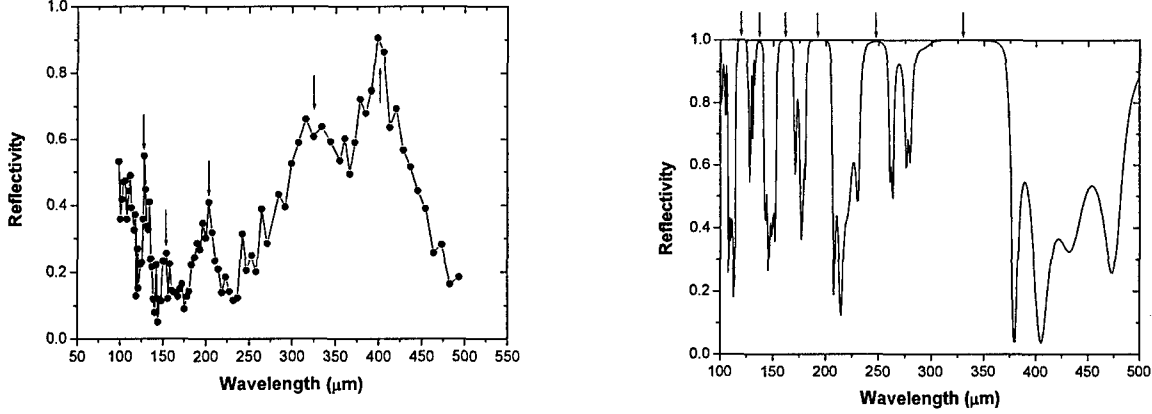

Fig. 4. Left: reflectivity is measured vs. wavelength for three Bragg reflectors stacked together with designed lengths for Si bridge and air slot to be 50.9 μm and 175 μm at incident angle of 34°. Right: reflectivity is calculated as a function of wavelength for the same Bragg reflectors as the left.

In our experiment the THz wave is from the output of a tunable THz source generated based on the phase-matched difference-frequency generation in a GaSe crystal [4]. Such a THz source has a typical tuning range of 58.2-3540 μm with the highest peak power of 209W at 196 μm. We have measured the spectra of the reflectivity for a variety of the Bragg reflectors fabricated by us. Fig. 4 shows one of our results for the designed lengths of the Si bridge and air slot to be 50.9 μm and 175 μm, respectively. We would like to note that for convenience the incident angle for this measurement is set to be about 34°. We have observed several peaks in the reflection spectrum at the wavelengths of 128 μm, 154 μm, 203 μm, 325 μm, and 398 μm, respectively. To calculate the reflectivity for the stacked Bragg reflectors we have taken into consideration the length fluctuations for the Si bridge and air slot within each reflector and among the three reflectors. Fig. 4 shows our spectrum calculated for the same Bragg reflectors at the incident angle of 34°. One can see that there are six peaks at the wavelengths of 120 μm, 137 μm, 162 μm, 193 μm, 247 μm, and 329 μm, respectively. For the incident angle of 34° the 1st order Bragg peak occurs at 329 μm instead of 700 μm. The pair of the peaks at 120 μm and 137 μm can hardly be resolved in our experiment. We believe the peak at 128 μm is the due to the convolution of these two peaks. On the other hand, the two separate peaks at the 247 μm and 329 μm cannot be resolved in our experiment either. In addition, we would like to note that theoretically there are two dips near 380 μm and 405 μm that could be one of the origins for the dip appearing near 375 μm. Obviously the measured reflectivities for the wavelengths longer than 400 μm significantly deviate from the calculated values. We believe this is caused by the diffraction of the THz wave by the interfaces between the adjacent reflectors. Another factor is the horizontal misalignment among the three reflectors in each stack. The highest reflectivity measured by us is about 91% at the wavelength of about 400 μm, which is high enough for our

Bragg reflector to be used as an output coupler. As one can see from Fig. 4 the measured reflectivity is much higher for the range of 325-400 µm. We believe this is due to the fact that near the 1st order the bandwidth for the Bragg peak is so broad that the horizontal misalignment among the three reflectors in each stack would cause much less fluctuation on the reflectivity.

In the next stage of the work, we will optimize the design of our Bragg reflectors and study the effect of waveguiding for the THz wave with the presence of alternating Si/air gratings. We will also use other two techniques, i.e. chemical etching and deep reactive ion etching to fabricate these Bragg reflectors. To reduce the diffraction of the THz wave by the interfaces between the adjacent reflectors, we will diffusion-bond the three reflectors. The new results will also be reported.

In summary, we have made a proof-of-principle demonstration on the Bragg reflectors in the THz domain based on a few periods of alternating Si bridges and air slots fabricated on the Si wafers by using a UV laser. Due to the high contrast of the indices between Si and air, there are certain advantages for these Bragg reflectors. Indeed, we only need a few pairs to achieve extremely high reflectivities. For three air slots, we have achieved a peak reflectivity as high as 91%. In addition, the bandwidth for the 1st order Bragg reflection is much broader due to greatly-reduced accumulation of the phase through the entire grating.

Some of these results were included in SPIE Proc. (2005).

1. R. Köhler, A. Tredicucci, F. Beltram, H. E. Beere, E. H. Linfield, G. Davies, D. A. Ritchie, R. C. Lotti, and F. Rossi, Nature **417**, 156-169 (2002).
2. L. Xu, X.-C. Zhang, and D. H. Auston, Appl. Phys. Lett. **61**, 1784-1786 (1992).
3. D. H. Auston, K. P. Cheung, and P. R. Smith, Appl. Phys. Lett. **45**, 284-286 (1984).
4. see, e.g., W. Shi, Y. J. Ding, N. Fernelius, and K. Vodopyanov, Opt. Lett. **27**, 1454-1456 (2002).
5. L. Friedman, G. Sun, and R. A. Soref, Appl. Phys. Lett. **78**, 401-403 (2001).
6. E. Yablonovitch, Phys. Rev. Lett. **58**, 2059-2062 (1987).
7. W. Shi and Y. J. Ding, Appl. Phys. Lett. **82**, 4435-4437 (2003).

12. Measurement of spectrum of two-photon absorption for ZnGeP$_2$

In this section, we report our new result on the measurement of the spectrum of two-photon absorption coefficients in the range of 0.76-1.33 µm on ZnGeP$_2$ based on z-scan technique. We have compared our measured values with calculations.

ZnGeP$_2$ has large second-order nonlinear coefficients (75 pm/V) and a wide transparency range (0.74-12 µm). Therefore, this material can be used for efficient generation of mid-IR to far-IR beyond 4 µm with the highest conversion efficiencies and output powers [1]. Although it has a wide transparency range a commercially-available ZnGeP$_2$ crystal always has anomalously-large absorption coefficients in the near-IR domain (1-2 µm) that are highly process-dependent. Recently, it was demonstrated that this material could be annealed such that the absorption coefficients in the range of 1-3 µm could be greatly reduced [2]. This enables us to use the pump sources at the wavelengths of 1.03 µm, 1.064 µm, and 1.55 µm that are conveniently available from Nd:YAG, Yb-doped and Er-doped fiber, and other near-IR lasers. Indeed, most recently we generated a monochromatic THz wave continuously tunable in the ranges of 83.1–1642 µm and 80.2–1416 µm as a result of phase-matched difference-frequency generation in an annealed ZnGeP$_2$ [3]. However, since the band-edge cut-off wavelength for ZnGeP$_2$ is about 0.74 µm, one would naturally assume that there is two-photon absorption (TPA) for the wavelengths below 1.48 µm. Such a multiphoton process can ultimately affect the performance of nonlinear conversion processes pumped by those IR wavelengths [4]. However,

to the best of our knowledge, there are no data for the TPA coefficients on this material. Here, we report our first result on the measurement of the TPA coefficients in the range 0.76-1.33 μm by using subpicosecond laser pulses based on z-scan technique [5]. To avoid contribution from free-carrier absorption to the effective two-photon absorption, short laser pulses are used.
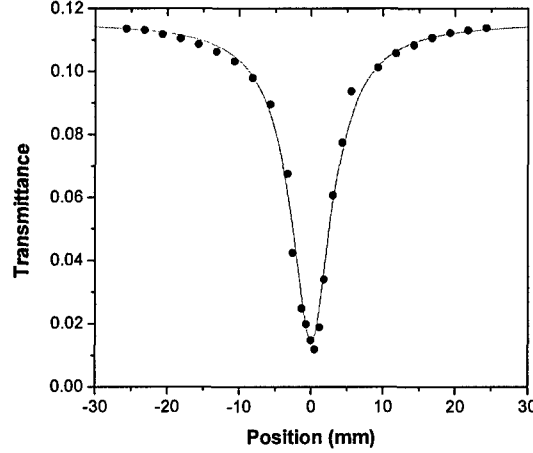

Fig. 1. Dots: transmittance measured vs. position by translating $ZnGeP_2$ crystal across beam waist of Gaussian beam (z = 0) at pump wavelength of 0.92 μm. Solid line: best nonlinear least-square fit by Eq. (1).

A single $ZnGeP_2$ crystal cut for $\theta = 0°$ has dimensions of a length of 12 mm along c axis and a cross-sectional area of 12 mm × 7.5 mm with no antireflection coatings. The linear absorption coefficient was previously measured to be 1.52 cm^{-1} at 1.064 μm. The laser beams for this experiment are from the output of a Ti:Sapphire laser with the pulse width of 120 fs and a repetition rate of 76 MHz and a subpicosecond optical-parametric oscillator based on CTA and KTA crystals. The pump beam is propagating along the optic axis of the crystal and then focused into the crystal by using a convex lens. The transmitted beam is collected by another convex lens and then measured by a power meter. By translating the crystal along the direction parallel to the optic axis of the crystal back and forth around the beam waist, we can measure the transmittance as a function of z. Fig. 1 shows a typical result of our z scan. Assuming the pump is a Gaussian beam, we have obtained the transmittance as a function of z:

$$
T = \frac{T_0 \exp(-\alpha l)\lambda z_0 \left(1+\dfrac{z^2}{z_0^2}\right)}{2\beta l_{\text{eff}}P} \ln\left[1+\frac{2\beta l_{\text{eff}}PT_0}{\lambda z_0\left(1+\dfrac{z^2}{z_0^2}\right)}\right]
\tag{1}
$$

where l is the crystal length, α is the linear absorption coefficient, $l_{\text{eff}} = [1-\exp(-\alpha l)]/\alpha$ is the effective crystal length, β is the TPA coefficient, P is the laser peak power, λ is the laser wavelength, T_0 is the transmittance through the front or back surface due to Fresnel reflections when the absorption is negligible, and $z_0 = \pi w_0^2/\lambda$ with w_0 the beam radius. By measuring w_0 and adjusting β in Eq. (1), we can achieve the best nonlinear least-square fit to the result shown in Fig. 1. One can see that we have obtained nearly perfect fitting at such a wavelength. We would like to note that the linear absorption is quite large in the range of 0.76-1.33 μm for the crystal length used. This is the reason why the transmittance obtained in Fig. 1 is low. Now if repeat

such a procedure for all the other pump wavelengths available, we can obtain the spectrum of β, see Fig. 2. To the best of our knowledge, this is the first report for the measurement of the full spectrum of the TPA coefficient in the range of 0.76-1.33 μm for $ZnGeP_2$. One can see from Fig. 2 that the TPA coefficient increases dramatically as the pump wavelength decreases below 1.16 μm. At the pump wavelength of 1.064 μm, the value of the two-photon absorption coefficient is extrapolated to be about 2.72 cm/GW based on our measurements. Since there have been no reports on the values of the TPA coefficients on $ZnGeP_2$, we cannot compare our results with any previous values. Based on a three-band non-parabolic model [6], we have also plotted the theoretical values. One can see that our experimental values are in a good agreement with the calculated ones. In addition, the dependence of β on $hc/\lambda E_g$ is in an excellent agreement with the theory except for the point at 1.335 μm.
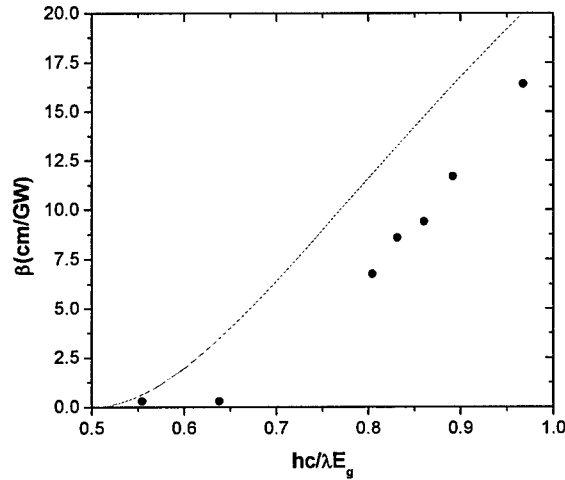

Fig. 2. Dots: spectrum of two-photon absorption coefficient by fitting profiles obtained via z-scan technique (see e.g. Fig.1) with our theory at typical incident average power of 300 mW. h is Planck constant, c is speed of light in vacuum, λ is pump wavelength, and $E_g \approx 1.677$ eV,. Solid line: theoretical result based on three-band non-parabolic model.

The spectrum of the TPA coefficient for $ZnGeP_2$ measured by us can be quite valuable for using this crystal towards the efficient generation of the mid-IR, far-IR, and THz waves based on parametric processes by using Ti:Sapphire, Nd:YAG, and other near-IR lasers.

These results were presented at CLEO/IQEC 2004.

1. P. G. Schunemann, K. L. Schepler, and P. A. Bundi, "Nonlinear frequency conversion performance of AgGaSe$_2$, ZnGeP$_2$, and CdGeAs$_2$," MRS Bull. 23, 45-49 (1998).
2. D. E. Zelmon, E. A. Hanning, and P. G. Schunemann, "Refractive-index measurements and Sellmeier coefficients for zinc germanium phosphide form 2 to 9 μm with implications for phase matching in optical frequency-conversion devices," J. Opt. Soc. Amer. B 18, 1307-1310 (2001).
3. W. Shi, Y. J. Ding, and P. G. Schunemann, "Coherent terahertz waves based on difference-frequency generation in zinc germanium phosphide: Improvements on tuning ranges and peak powers," submitted to Opt. Commun.
4. I. B. Zotova and Y. J. Ding, Opt. Commun. 198, 453 (2001).
5. M. Sheik-Bahae, A. A. Said, T. H. Wei, D. J. Hagan, and E. W. Van Stryland, IEEE J. Quantum Electron. 26, 760 (1990).
6. C. R. Pidgeon, B. S. Wherrett, A. M. Johnston, J. Dempsey, and A. Miller, Phys. Rev. Lett. 42, 1785 (1979).

13. Observation of stimulated emission in
short-period quasi-indirect type-II GaAs/AlAs superlattices

We have demonstrated that type-II GaAs/AlAs superlattices can be used to greatly increase the recombination times and to achieve stimulated emission in these structures with greatly-reduced gain coefficients for applications as optical amplifiers.

Short-period GaAs/AlAs superlattices (SL's) are indirect in both real space and k space, thus the lifetime of electron-hole pairs in these structures can be engineered to be as long as a few µs. There are a number of benefits associated with the long lifetime for a gain medium such as ability to store large energy for high peak power Q-switched applications, reduction of cross-gain modulation in optical amplifiers, and reduction in intensity noise [1]. Within the last fifteen years or so, there have been intensive studies on short-period GaAs/AlAs SL's. For example, the indirect transitions in type-II superlattices were due to recombination of localized excitons [2]. In this work, we have measured the recombination times in short-period type-II GaAs/AlAs SL's. Unlike the previous results in Refs. [2,3], our photoluminescence (PL) decay curves exhibit slow and fast decay rates, which are attributed to the recombination of localized and free quasi-indirect excitons. Our results show that the type-II SL's can be engineered to achieve long recombination times. Moreover, we have achieved stimulated emission and determined the gain coefficient for the type-II SL's.

Table 1. Short-period GaAs/AlAs SL's used in this report.

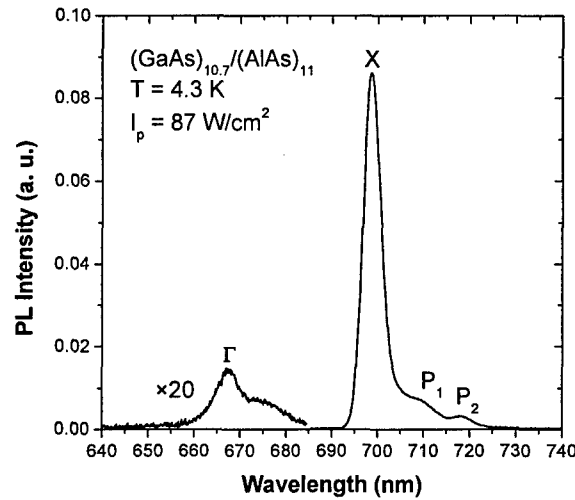| №	Thickness (ML) GaAs/AlAs	E_Γ (eV)	E_X (eV)	$\Delta E_{\Gamma X}$ (meV)	$\hbar\omega_p$ (meV) GaAs	$\hbar\omega_p$ (meV) AlAs	τ(ns)
1	17.9/19.3	1.671	-	-	-	-	-
2	13.5/11.5	-	1.744	-	-	-	230
3	12/12	1.801	1.757	44	28	48	500
4	10.5/11.3	1.832	1.767	65	27	48	800
5	10.7/11	1.850	1.776	74	27	48	800
6	8/7	1.975	1.854	121	30	49	1300
7	6/6	2.062	1.902	160	-	47	600
8	4/4	2.224	1.972	252	31	49	600

Fig. 1. Typical PL spectrum of type-II GaAs/AlAs SL's measured in this experiment at temperature of 4.3 K and pump intensity of 87 W/cm^2.

Our short-period GaAs/AlAs SL's were grown on semi-insulating GaAs (001) substrates in a Riber 32 MBE system at the temperature of 580°C with a growth rate of 1 ML/s for both GaAs and AlAs. The layer thicknesses for GaAs and AlAs were measured by X-ray diffraction and reflection high-energy electron diffraction. Each of the SL samples consists of 40 periods of GaAs and AlAs layers with different thicknesses shown in Table 1. A cryostat is used in the experiment to vary the sample temperature. The pump sources include a pulsed laser at 532 nm (6-ns pulse width with 10 Hz repetition rate) and cw green and red lasers at 532 nm and 695 nm in order to measure decay times and stimulated emission, respectively. The PL is picked up by a photomultiplier tube with a response time of ~6 ns after a spectrometer.
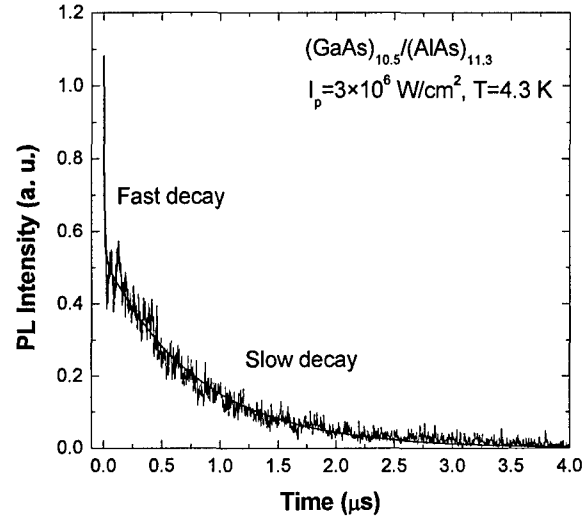

Fig. 2. PL decay curves at 4.3 K. The smooth curves buried in experimental decay curves are fitting results by using a biexponential function. The pump intensity is 3×10^6 W/cm^2.

Fig. 1 shows a typical measurement of PL spectrum. Two peaks labeled by X and Γ correspond to the quasi-indirect and quasi-direct transitions, respectively. The other two tiny peaks marked by P_1 and P_2 are assigned to the phonon-assisted indirect transitions. The PL time decay curves measured at different temperatures are shown in Fig. 2. Unlike the previous experimental results [2,3], our results clearly show a superposition of fast and slow decays. The free exciton recombination corresponds to the fast decay while the recombination of the localized excitons corresponds to the slow one. For all the type-II samples grown by us, the slow decay times are determined by us and summarized in Table 1. One can see that the decay times are in the range of 230 ns – 1.3 μs. It is important for us to point out that the decay times for the (GaAs)$_{4,6}$/(AlAs)$_{4,6}$ are much shorter than that for the three other type-II SL's. We believe this is due to the fact that when the SL period is sufficiently short the overlap between the wave functions of the electrons and heavy holes is significantly increased due to the penetrations of the wave functions into the AlAs barriers.

Our setup for achieving stimulated emission is shown in Fig. 3(a). Fig. 3(b) shows our results of the measurements of the cw PL intensity vs. emission wavelength at the frequency locked with the chopper for the laser beam at 695 nm. As one can see from Fig. 3(b), there is a large gain when the pump beam at 532 nm is present for a propagation length of about 1 mm. Using such a technique, the gain is then measured vs. the pump intensity at 532 nm for different pump intensities at 695 nm, see Fig. 4. At a low enough pump intensity at 695 nm, the gain

linearly increases as the pump intensity at 532 nm increases. For higher and higher pump intensities at 695 nm, the gain is more and more saturated. Indeed, when the laser intensity at 695 nm is about 8.7 kW/cm^2, there is almost no gain no matter how high the laser intensity at 532 nm is. When the laser intensity at 695 nm is high enough, the carriers generated by this beam completely fill up the quasi-X and quasi-Γ bands. In this case, only when the SL temperature is increased the gain can be increased as well due to the empty states available in the both bands. This is confirmed in our experiment, indeed. The highest gain is measured to be 14.4 at 150 K and for the pump intensity of 170 W/cm^2 at 695 nm, which corresponds to a gain coefficient of about 30 cm^{-1}. Such a low value of the gain coefficient is the direct consequence of increasing the recombination time in the SL's. One can see from Fig. 3(b) that the gain coefficient for the quasi-Γ transition is actually much larger than that for the quasi-X transition due to the fact that the quasi-Γ transition is more direct. We believe the PL pumped by the laser beam at 695 nm is propagating as an evanescent wave inside the type-II SL's. Such an evanescent wave is then amplified when the laser beam at 532 nm is present.
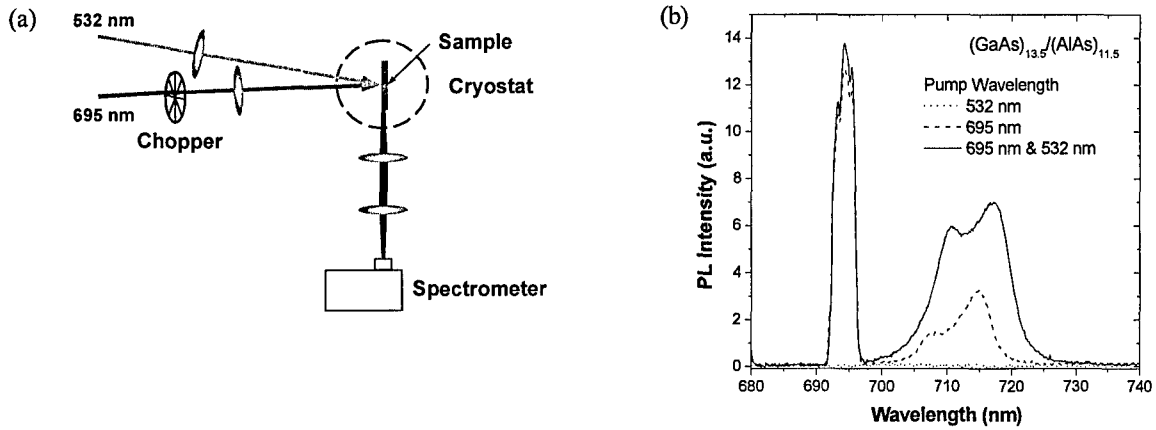
Fig. 3. (a) Experimental setup for achieving stimulated emission and measuring gain coefficients. (b) PL intensity vs. emission wavelength when only laser beam at 532 nm is present (dotted line), only laser beam at 695 nm is present (broken line), and both laser beams at 532 nm and 695 nm are present (solid line). Left peaks below 700 nm are from pump lasers.
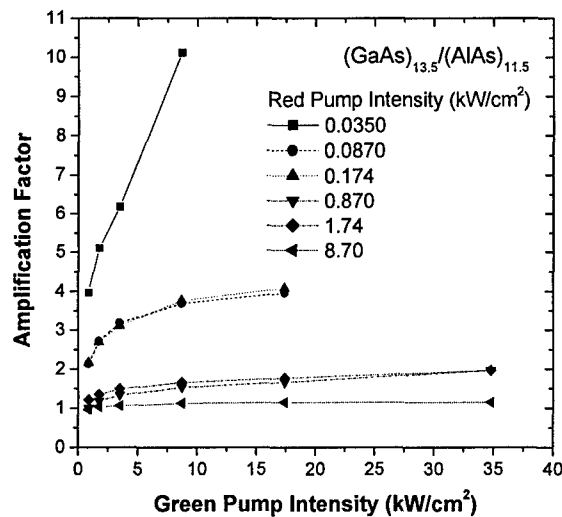

Fig. 4. Gain vs. pump intensity at 532 nm for different pump intensities at 695 nm at 80 K.

Our next step is to use an external-cavity configuration combined with a Q switch to achieve Q-switched high-power output. We will also use Sb-based type-II SL's to achieve Q-switched high powers in the range of 2-6 μm. Our estimates show that for an average of 10 mW the peak power can be increased to 100 W by using our optimized type-II SL's. We will report these new results as well.

By engineering the type-II SL's, we have demonstrated that they can be used to obtain long recombination times. Furthermore, we have achieved stimulated emission by optically-amplifying the evanescent wave in these structures and determined the gain coefficients. Indeed, due to the increase of the recombination times in these structures, the gain coefficient is greatly reduced. These structures are ideal for achieving high peak powers via Q-switching, decreasing the amplitude noise, and reducing the cross talk for optical amplifiers. Another potential application for these type-II SL's is the possibility of efficiently removing LO phonons through the optically-pumped stimulated emission, see project #3 above. Such a novel approach is made possible since an electron generated by optical pumping can absorb a LO phonon and then up-transfer from the quasi-X band to the quasi-Γ band. Thus, the stimulated emission carries the energies of the LO phonons away with it.

Some of these results were included in Laser Phys. (2005), Proc. LPHYS'04.

1. J. B. Khurgin, I. Vurgraftman, and J. R. Meyer, "Modeling of Q-switched semiconductor lasers based on type II QW's –increasing the pulse energy and peak power," Appl. Phys. Lett. **80**, 2631-2633 (2002); "Reduced crosstalk semiconductor optical amplifiers based on type-II quantum wells," IEEE Photon. Tech. Lett. **14**, 278-280 (2002).
2. F. Minami, K. Hirata, K. Era, T. Yao, and Y. Masumoto, "Localized indirect excitons in a short-period GaAs/AlAs superlattice," Phys. Rev. **B36**, 2875-2878 (1987).
3. M. D. Sturge, J. L. Mackay, C. Maloney, and J. K. Pribram, "Photoluminescence decay time studies of type-II GaAs/AlAs quantum well structures," J. Appl. Phys. **66**, 5639-5641 (1989).
4. D. S. Jiang, H. Jung, and K. Ploog, "Temperature dependence of photoluminescence from GaAs single and multiple quantum-well heterostructures grown by molecular-beam epitaxy," J. Appl. Phys. **64**, 1371–1377 (1988).

14. Coupling between InAs quantum dots and strained InGaAs/GaAs coupled quantum wells

We have studied coupling between InGaAs/GaAs coupled quantum wells and self-assembled InAs quantum dots by measuring the linewidths, peak energies and peak intensities of photoluminescence peaks for different pump powers and lateral locations.

Self-assembled quantum dots (QD's) as a result of phase transition due to lattice mismatch suffer from severe size fluctuation. Recently, strain-induced quantum-well dots (QWD's) have been observed in InGaAs and InGaP quantum wells (QW's) by using InP QD's as a 2-D stressor [1-4]. Since the thickness of the QW's can be controlled within a subatomic layer, the size fluctuation of the strain-induced QWD's can be greatly reduced. Moreover, the interface and surface recombination rates can be significantly reduced. Since the QWD's are next to QW regions, the carrier capture and de-trapping rates are expected to be greatly increased. However, so far in all the previous work only InP QD's have been used as stressors and InP QD's have not been capped. Recently [5], we demonstrated that InAs QD's could also be used to strain an InGaAs/GaAs QW. As a result, the optical properties have significantly been improved. Indeed, the linewidth for the QWD emission has been reduced by as large as 29 meV compared with that for the QD's. Furthermore, the PL intensity for the QWD's has been increased by about a factor of 2. It was predicted quite well ago [6] that the spatial distribution of the strain field induced by

the QD's should depend on the width and period of the stressors, the thickness of the cap layer, and total thickness of the QW. Besides the strain field, coupling between the QD's and QW can be made the optimum by engineering the structures of the QW's.

In this work, the photoluminescence spectra (PL) of $In_{0.26}Ga_{0.74}As$/GaAs coupled quantum wells strained by the self-assembled InAs QD's are investigated and compared with those of the InAs QD's and coupled quantum wells (CQW's). We have chosen CQW's since they allow us to study the spatial uniformities of the strain fields inside each of the two InGaAs quantum wells. In addition, the lowest transition of the CQW's can be made quite close to the average of the lowest transitions in the InAs QD's. Thus, we are approaching the regime of the optimum coupling between the CQW's and QD's. The comparisons among the QD's, CQW's, and CQWD's show that CQWD's are much more uniform spatially in the lateral plane. Furthermore, we have demonstrated that the two transitions in the CQWD's are due to the recombination of the electrons and heavy holes truly confined in the three dimensions.

Two sets of the samples were grown on GaAs (001) substrates by two separate MBE systems at the temperature range of 500-620°C. The first set of the sample was grown by a Riber 32 MBE system at the temperature of 500°C and growth rates of 0.23, 0.28 and 0.1 ML/s for GaAs, InGaAs and InAs, respectively. The CQWD sample consists of a 300 nm-thick GaAs buffer layer, 75 Å-thick $In_{0.26}Ga_{0.74}As$ well, 50 Å-thick GaAs barrier, 35 Å-thick $In_{0.26}Ga_{0.74}As$ well, 50 Å-thick GaAs barrier, 2.5 ML-thick InAs and a 20 nm-thick GaAs cap layer. In order to compare the experimental results between the CQWD's and self-assembled InAs QD's, two additional samples, i.e. the self-assemble InAs QD's and $In_{0.26}Ga_{0.74}As$/GaAs coupled quantum wells, were grown. The second set of the samples was grown at 620°C, 520°C, and 520°C for the buffer layers, InGaAs/GaAs CQW layers, and 2.2-ML InAs QD layers and GaAs cap layers, respectively. Due to the large lattice mismatch between InAs and GaAs, the 2.5-ML and 2.2-ML-thick InAs layers break into self-assembled QD's with an average diameter and height of ~10 nm and ~5 nm, respectively. Each InAs QD may apply a 2-D potential to the CQW layers beneath it. Therefore, the strain-induced CQW's are formed. Moreover, the InAs QD's are strongly coupled with the strained CQW's to form the CQWD's.
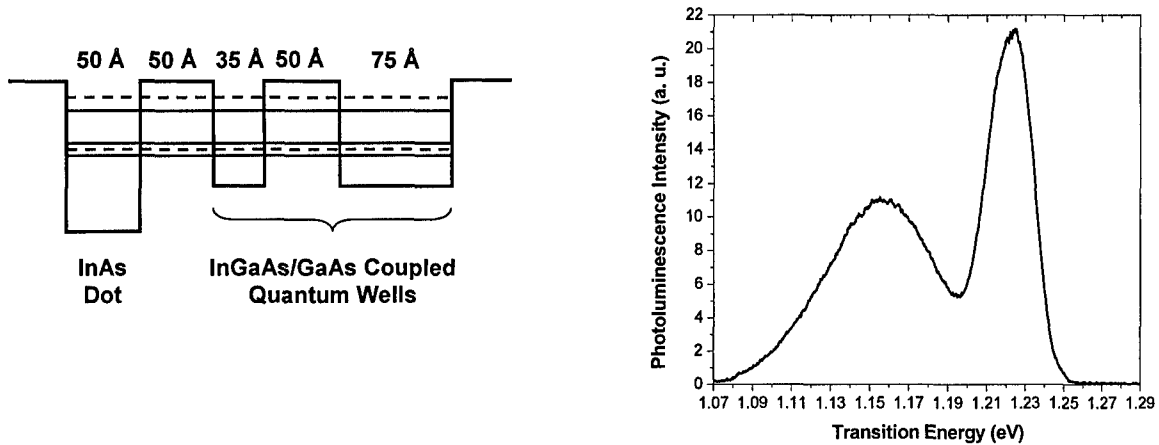

Fig. 1. Left: configuration of coupled QW's strained by InAs QD's to form CQWD's. Right: PL spectrum when QD's are adjacent to narrow well of CQW's.

A Ti:sapphire laser with the wavelength of 800 nm is used as a pump source in all the PL measurements. Fig. 1 shows a configuration of the CQWD's in which the QD's are grown

adjacent to the narrow InGaAs quantum well. Fig. 2 shows our measurements of the PL spectra for the first CQWD sample. One can see that there are two distinct peaks corresponding to the two new quantum-dot states as a result of mixing the original QD and strained CQW states, i.e. well-like and dot-like transitions. Therefore, the well-like transition is significantly broadened compared with the transition just from the CQW's. In addition, the dot-like transition is also significantly broadened on the low-energy side compared with the transition peak from the QD's. Moreover, the well-like and dot-like transitions suffer from the tremendous fluctuations from one position to the next within the lateral plane in terms of their peak intensities and linewidths. Indeed, the well-like peak intensity fluctuates by 169% while the linewidth changes by 53%. On the other hand, for the dot-like transition the peak intensity and linewidth change by 65% and 20%, respectively. We believe these broadenings and spatial fluctuations are due to the spatially-inhomogeneous strain fields parallel to the surface normal applied to the wide well by the QD's. In order to further investigate spatial uniformities of the strain fields inside the CQW's, we have grown the second CQWD sample in which the QD's are grown adjacent to the wide InGaAs quantum well. Fig. 2 shows the measurements of the PL spectra at different pump powers. The dot-like transition is significantly sharpened on the low-energy side compared with that for the QD's. On the other hand, the well-like transition has a narrower linewidth than that for the CQW's. Compared with the results above for the first CQWD sample, we conclude that the strain fields are more or less spatially uniform across the wide InGaAs quantum well (width of 75 Å) in the second CQWD sample.

At a low enough pump power, the PL spectrum is dominated by the dot-like transition, see Fig. 2. However, as the pump power increases the relative strength for the well-like transition significantly grows. This is due to band-filling effects, namely as the pump power increases more and more carriers start to fill up the well-like states due to the fact that the dot-like states can only take the maximum carrier densities. At the sufficiently high pump power, the PL spectrum is completely dominated by the well-like transition. In order to confirm that these two transitions are originated from quantum-dot states, we have measured the linewidths for the two peaks in Fig. 2, see Fig. 2. As one can see from Fig. 2, the linewidths for these two peaks more or less stay the same. On the contrary, for the InAs QD's and InGaAs/GaAs coupled QW's, the linewidths increase from 75 meV and 14 meV to 157 meV and 33 meV, respectively. This indicates that the dot-like and well-like states in the CQWD's are truly quantum-dot states in nature.
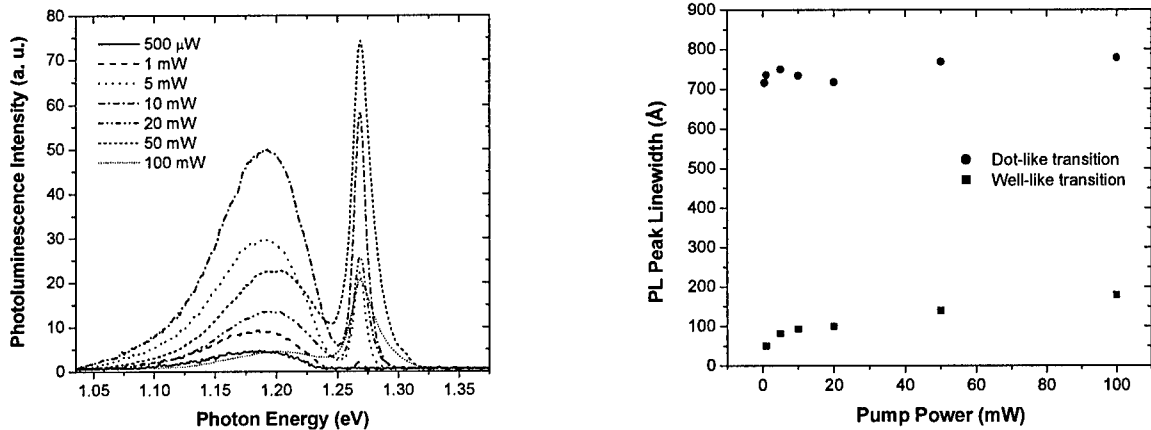
Fig. 2. Left: PL spectra at different pump powers for CQWD's measured at 4.3 K, in which QD's are adjacent to wide well of CQW's. Right: PL peak linewidths as a function of pump power, determined from the left figure.

Another strikingly difference between the CQWD's and QD's and CQW's is reflected by the spatial uniformities in the lateral plane normal to the growth direction, see Fig. 3. Indeed, for the QD's and CQW's the peak intensities and lineshapes change quite a lot from one location to the next. Specifically, for the QD's the peak intensity and linewidth change by 64% and 48%, respectively. On the other hand, for the CQW's the peak intensity and linewidth change by 70% and 17%, respectively. In contrast, for the CQWD's the peak intensities of the well-like and dot-like transitions only change by 9.1% and 6.5%, respectively, while the corresponding linewidths fluctuate by 2.3% and 1.9%, respectively. Based on the comparisons made above, we can clearly see that the CQWD's are much more uniform spatially compared with the QD's and even CQW's. Furthermore, these fluctuations are much less than the corresponding values for the first CQWD sample above. Therefore, this indicates that the strain fields are more or less uniform within the wide InGaAs QW. This new type of the highly-uniform quantum dots can definitely be used for implementing an array of optoelectronic devices with the uniform performances. In addition, these well-like and dot-like states can be used to achieve coherent oscillations for the carriers.
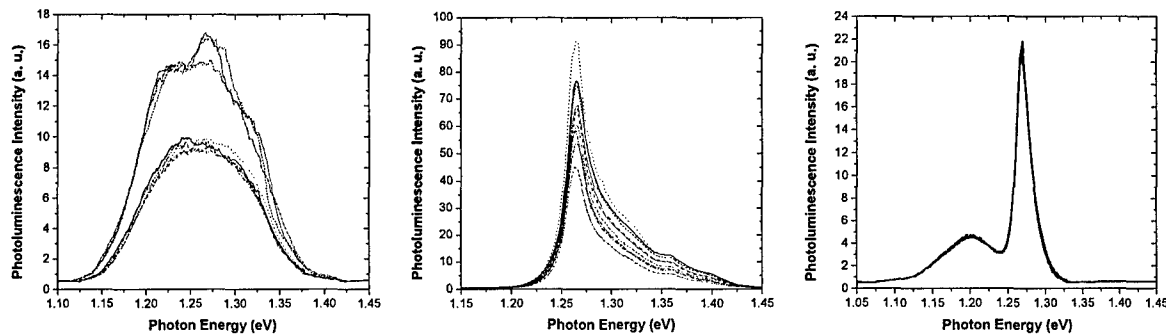

Fig. 3. PL spectra at different lateral locations for left, QD's; middle, CQW's; and right CQWD's (QD's are adjacent to wide well of CQW's), measured at 4.3 K and pump power of 100 mW.

The InGaAs/GaAs CQWD's are formed by using the self-assembled InAs QD's as stressors applying the strain fields on the InGaAs/GaAs coupled quantum wells. We have evidenced strong coupling between the QD's and strained CQW's to form a new type of quantum dots in terms of optical properties. Furthermore, we have also studied spatial uniformities of the strain fields applied by the QD's to the different regions of the CQW's. Finally, we have demonstrated that the CQWD's are much more uniform spatially in the lateral plane than the QD's and even CQW's.

These results were published in SPIE Proc. (2005) and presented at CLEO/IQEC (2004).

1. H. Lipsanen, M. Sopanen, and J. Ahopelto, "Luminescence from excited states in strain-induced $In_xGa_{1-x}As$ quantum dots," Phys. Rev. **B51**, 13868-13871 (1995).
2. M. Sopanen, H. Lipsanen, and J. Ahopelto, "Strain-induced quantum dots by self-organized stressors," Appl. Phys. Lett. **66**, 2364-2366 (1995).
3. M. Sopanen, M. Taskinen, H. Lipsanen, and J. Ahopelto, "Red luminescence from strain-induced GaInP quantum dots," Appl. Phys. Lett. **69**, 3393-3395 (1996).
4. G. Walter, N. Holonyak, Jr., J. H. Ryou, and R. D. Dupuis "Room-temperature continuous photopumped laser operation of coupled InP quantum dot and InGaP quantum well in InP-InGaP-In(AlGa)P-InAlP heterostructures," Appl. Phys. Lett. **79**, 1956–1958 (2001).
5. X. Mu, Y. J. Ding, Z. Wang, and G. J. Salamo, "Quantum-well dots formed by a single InGaAs/GaAs quantum well strained by an array of InAs quantum dots," submitted to Appl. Phys. Lett.

6. Z. Xu and P. M. Petroff, "Stain-induced carrier confinement in a buried stressor structure," J. Appl. Phys. **69**, 6564-6568 (1991).

15. A novel detection scheme for THz waves based on upconversion at room temperature

Within the last two decades, THz waves have been generated based on a variety of the mechanisms. Among them, THz parametric processes, especially difference-frequency generation, offer the advantages of high coherence (monochromatic output), simplicity for wavelength tuning, easy alignment, and stable output powers and wavelengths. For example, by using a GaSe crystal the output wavelength was tuned in a wide range of 56.8-1618 μm (5.27-0.18 THz) whereas the highest peak power was 69.4 W at 196 μm [1]. Both of the tuning range and peak power have been significantly extended and improved by us since. A widely tunable monochromatic THz wave has potential applications in chemical analysis [2], detections of chemical and biological agents, identification of bioaerosols, and imaging. However, in order to develop practical instruments for the field applications a new detection scheme must be developed. Indeed, the most sensitive THz detector available so far is the bolometer. However, such a detector must be cooled to 4 K or below. (The optimum temperature is 1.8 K.) Although Schottky diodes can be used to measure the average powers of the THz radiation at room temperature [3], they cannot be used to measure the THz pulses with high peak powers and low repetition rates. Indeed, the average powers produced by the difference-frequency generation are not high enough to be picked up by any Schottky diodes. (For a peak THz power of 200 W, a pulse width of 5 ns, and a repetition rate of 10 Hz, the average power is about 10 μW.) Besides, most Schottky diodes have low responsivities near 1 THz and above. Furthermore, both Schottky diodes and bolometers are slow detectors. For example, the bandwidth for a bolometer is usually limited to 30 kHz (a response time of 15 μs). Due the slow response, the bolometer picks up a lot of noise between the short THz pulses. Obviously a new scheme for the THz detection is really needed. A new THz detector must be able to operate at room temperature, have a high sensitivity, and have a wide bandwidth (short response time).

In this section, we report our first observation of upconversion achieved in a GaSe crystal, i.e. the generation of an infrared wave by mixing an intense infrared beam with a weak THz wave. We demonstrate that such a parametric process can be used to measure the THz peak power, wavelength, linewdith, and pulse width. Due to the limitation of the bandpass filter, the THz wavelengths measured by us are limited to the range of 75-187 μm whereas the minimum THz peak power is about 2.1 W, which corresponds to an average THz power of 128 nW. There are a few advantages for using the upconversion for the THz detection. First, the THz wave is now detected at room temperature. Second, since the THz wave has to be coherent for the efficient upconversion, we can significantly reduce the background noise originated from the incoherent THz wave. Third, even though the conversion efficiency for the upconversion is low, see below, the minimum THz power measured by us is reasonable low since we take advantage of the low-noise and high-responsivity InGaAs photodiode in the infrared region. Fourth, the response of this new detection system can be very fast (~ ns) if a fast PMT is used.

In our experiments, our THz source is the output produced based on different-frequency generation in a GaSe crystal [1]. In order to achieve the upconversion, we mixed a Nd:YAG laser at 1.064 μm with a peak intensity of several MW/cm^2 to with the THz wave from our THz source in the second GaSe crystal, based on type-*oe-e* phase-matched difference-frequency generation in which the first two letters, *oe*, designate the polarizations of the 1.064-μm and the THz beams, respectively, and the third letter, *e*, denotes the polarization of the up-converted

signal. Fig. 1 is the setup for an upconversion experiment. A THz signal was focused to a 14-mm-thick GaSe crystal by a parabolic mirror. In order to allow the 1.064-μm beam to go through the mirror, we drilled a hole with a diameter of 2 mm through the mirror.
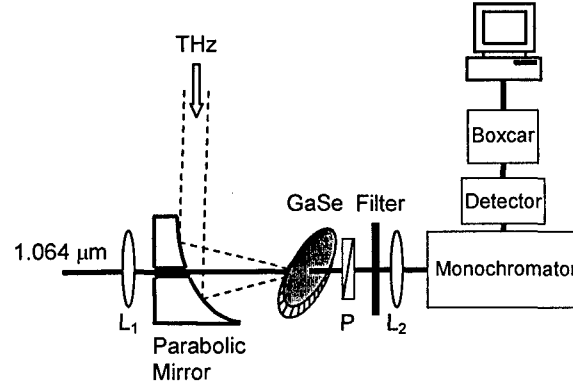

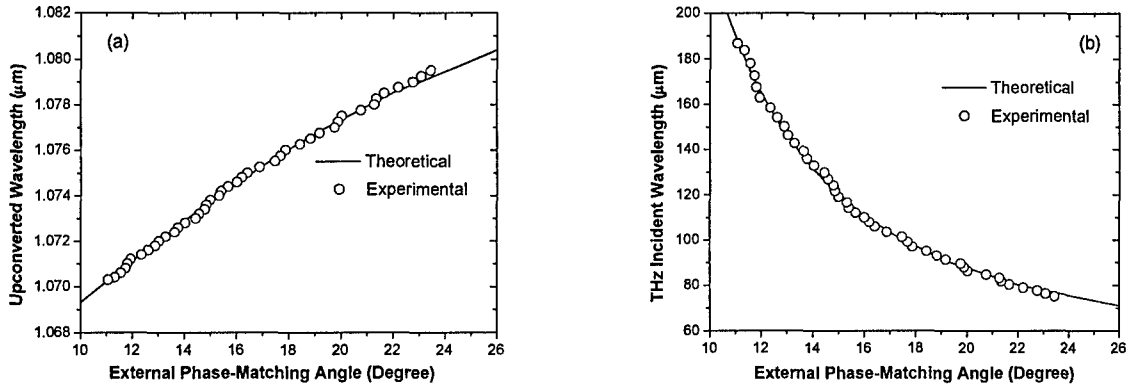Fig. 1. Experimental setup for THz detection based on upconversion.

Fig. 2. Phase-matched angle-tuning results for (a) upconverted signal and (b) THz input.

A polarizer and a bandpass filter were placed in the pass of the upconverted beam. The upconverted signal was focused onto a slow InGaAs detector after passing through a compact monochromator (5.25"×6.25"×3.25"). The upconverted signal was amplified and averaged in a boxcar integrator. Fig. 2(a) shows the angle-tuning result for the upconversion. One can see from Fig. 2(a) that the up-converted signal wavelengths cover the range of 1.0703-1.0795 μm. The solid curve corresponds to the theory obtained by using the phase-matching condition and dispersion relations [4]. One can see that our experimental results are in a very good agreement with the theory. Fig. 2(b) shows our result for the incident THz wavelengths, determined from the wavelengths of the Nd:YAG laser and up-converted signal. According to Fig. 2(b), the THz incident wavelengths measured by us cover the range of 75-187 μm.

The spectra of the upconverted signal were determined based on the output voltages of the InGaAs photodiode measured by us and calibrated by using an InP/InGaAsP PMT with response times of a few ns, see Fig. 3. It is worth noting that the spectra of the up-converted signal shown in Fig. 3 exhibit several sharp dips, which are due to the absorption of the THz beam by the water vapor in the beam pass [2].
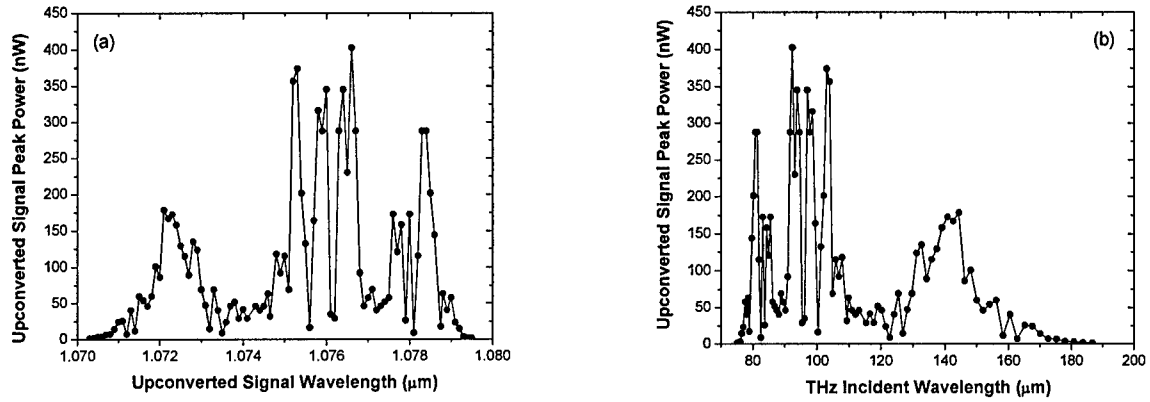
Fig. 3. Upconverted-signal peak power vs. (a) upconverted signal wavelength and (b) THz incident wavelength.

We also measured the linearity of our detection system, see Fig. 4. One can see that the response is linear. Moreover, by using our detection system the dynamic range was determined to be two orders of magnitude. By analyzing the result presented in Fig. 4, we determined the responsivity to be 0.174 mV/W. One can see that the highest peak power for the upconverted signal is 409 nW at the wavelength of 1.0766 μm for the pump power of 242 W at the THz incident wavelength of 92.4 μm. Therefore, the highest conversion efficiency for the upconversion was measured to be 1.69×10^{-7}%. On the other hand, the minimum detectable power for the upconverted signal is 1.15 nW, which corresponds to the THz peak power of 2.1 W measured by the calibrated bolometer. Our detection system allows us to determine the linewidth of the input THz wave by measuring the linewidth of the upconverted signal via a compact spectrometer. Indeed, we measured the linewidth to be about 0.22 THz at $\lambda \approx 97$ μm. Furthermore, by measuring the temporal response of the upconverted signal using the ns-InP/InGaAsP PMT we obtained the pulse duration for the THz pulses to be 6.09 ns. For the minimum detectable THz power of 2.1 W, the corresponding average power is 128 nW. Based on our calculations, the minimum detectable power could be a few orders of magnitude lower than 2.1 W if the ns-InP/InGaAs PMT was used instead of the slow InGaAs detector.
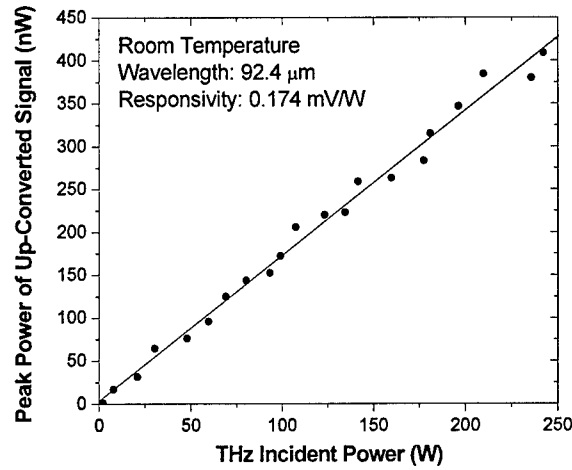

Fig. 4. At the THz incident wavelength of 92.4 μm, upconverted-signal peak power vs. THz incident power.

In summary, by upconverting a THz beam to the infrared output through mixing the THz input with a pump beam from a Nd:YAG laser in a GaSe crystal based on phase-matched difference-frequency generation, we have demonstrated a novel detection scheme for the THz beam. This new detection method offers the advantages of measuring the THz peak power, wavelength, linewdith, and pulse width at room temperature. We believe such a detection system will eventually replace bolometers and Schottky diodes and could be the key to the implementations of the practical systems for fully taking advantage of the THz waves.

These results were published in Appl. Phys. Lett. (2006) and J. Nonlinear Opt. Phys. Mats. (2006).

1. W. Shi, Y. J. Ding, N. Fernelius, and K. L. Vodopyanov, "Efficient, tunable, and coherent 0.18-5.27-THz source based on GaSe crystal," Opt. Lett. **27**, 1454-1456 (2002).
2. W. Shi and Y. J. Ding, "Fingerprinting molecules based on direct measurement of absorption spectrum by frequency-tuning monochromatic THz source," Laser Phys. Lett. **1**, 560-564 (2004).
3. See, e.g., H. R. Fetterman, P. E. Tannenwald, B. J. Clifton, C. D. Parker, W. D. Fitzgerld, and N. R. Erickson, "Far-IR heterodyne radiometric measurements with quasioptical Schottky diode mixers," Appl. Phys. Lett. **33**, 151-154 (1978).
4. K. L. Vodopyanov and L. A. Kulevskii, "New dispersion relationships for GaSe in the 0.65–18 μm spectral region ," Opt. Commun. **118**, 375-378 (1995).

16. Generation of quasi-single-cycle THz pulses based on broadband-phase-matched difference-frequency generation: high conversion efficiencies and output powers

Short THz pulses have become essential for a number of applications such as THz spectroscopy, biomedical diagnostics, and chemical identification [1]. In the past, these pulses were generated via optical rectification [i.e. difference-frequency generation (DFG) within each pulse] [2], photoconduction [3], and Cherenkov radiation [4]. However, the THz pulses generated in the past usually have low energies and peak powers. For example, using a pump intensity of 280 GW/cm^2, a maximum conversion efficiency of $\sim 10^{-10}$ was achieved based on optical rectification [5]. We are motivated by finding out the upper limit for the conversion efficiency on the THz generation by using a single optical pulse. In order to maximize the conversion efficiency, the bandwidth for the THz pulses must reach the limit, i.e. that for single-cycle pulses. Although wideband THz pulses were generated [6] and detected [7] using ZnTe, the bandwidths available were still much narrower than that for the single-cycle pulses.

Here, we propose to use the broadband-phase-matched DFG among different frequency components within each ultrafast laser pulse for the efficient generation of the quasi-single-cycle THz pulses with high conversion efficiencies and output powers [8].

Taking Fourier transforms of the two coupled Maxwell's equations for the pump and THz waves, one obtains:

$$\left[\nabla^2 + \frac{\Omega^2}{c^2}n^2(\Omega)\right]\overline{E}_{THz}(\vec{r},\Omega) = \frac{2d_{eff}}{c^2}\int_{-\infty}^{+\infty}\left(\frac{\partial^2 E_p^2}{\partial t^2}\right)e^{-i\Omega t}dt = -\frac{d_{eff}\Omega^2}{c^2}\overline{|\tilde{\varepsilon}|^2} \tag{1a}$$

$$\left[\frac{i}{2k_p}\nabla_t^2 + \frac{\partial}{\partial z} + i\frac{n_{pg}\Omega}{c} + \frac{i}{2}k_p''\Omega^2\right]\overline{\tilde{\varepsilon}} = -\frac{2id_{eff}\omega_p}{cn_p}\overline{E_{THz}\tilde{\varepsilon}} \tag{1b}$$

where k_p, ω_p, n_{pg}, k_p'', E_p, and $\tilde{\varepsilon}$ are the wave vector, angular frequency, group index, the group velocity dispersion (GVD) parameter, electric field and a slowly-varying envelope for the pump beam at λ_p, d_{eff} is the effective nonlinear coefficient in the frequency domain, E_{THz} and n are the electric field and index of refraction for the THz wave, and c is the speed of light in vacuum.

Assume that both the pump and THz waves are the plane waves and GVD is negligible. Consider $\widetilde{\varepsilon}(z,t) = E_0 g[(t - n_{pg}z/c)/\tau]$, where E_0 is the magnitude of the electric field for the pump wave and τ is the effective pulse width. First, neglecting the pump depletion, one obtains

$$\overline{E}_{THz}(L,\Omega) = -\frac{id_{eff}E_0^2\Omega\overline{g}^2(0,\Omega)L}{c(n_{pg}+n)}sinc\left[\frac{\Omega}{2c}(n_{pg}-n)L\right]exp\left[-i\frac{\Omega}{2c}(n_{pg}+n)L\right] \tag{2}$$

where L is the length of the nonlinear medium. The frequency dependence of $\overline{E}_{THz}(L,\Omega)$ in Eq. (2) can be separated into the spectrum and phase-matching terms, i.e. the first and second expressions in Eq. (2). For hyperbolic-secant pulses, $\overline{g}^2(0,\Omega) = \pi\Omega\tau^2/sinh(\pi\Omega\tau/2)$. The first expression has a peak frequency determined by $\Omega_{THz}\tau \approx 1.219$. In addition, the spectral bandwidth is defined between $\Omega_{low} \approx 0.5652/\tau$ and $\Omega_{high} \approx 2.147/\tau$. On the other hand, the phase-matching term reaches the maximum value when the phase-matching condition is satisfied [9,6]:

$$n(\Omega_{THz}) = n_{pg}(\omega_p) \tag{3}$$

According to Eq. (2), the coherence length is defined as [9,6]: $L_c = \lambda/(2|n_{pg} - n|)$, where $\lambda = 2\pi c/\Omega$. For the fixed pump frequency, we assume that the phase-matching condition is perfectly satisfied at one THz frequency. The coherence lengths can be then long for a wide range of the THz frequencies (wavelengths) in the vicinity of this phase-matched output frequency (wavelength), if the corresponding indices of refraction change little in the same range. Therefore, if $L \le L_c$ for the same range of the output wavelengths the corresponding output wavelengths form a phase-matching bandwidth. Consider the case when the phase-matching bandwidth is much wider than the spectral bandwidth defined above, which is approximately the same as the ideal case when Eq. (3) is satisfied for every output frequency. We can then plot the spectrum of the electric-field amplitude according to Eq. (2) in Fig. 1(a).

One can take Fourier transform of Eq. (2):

$$E_{THz}(L,t) = -\frac{iE_0^2L}{2\pi c}\int_{-\infty}^{+\infty}\frac{d_{eff}\Omega\overline{g}^2(0,\Omega)}{n_{pg}+n}sinc\left[\frac{\Omega}{2c}(n_{pg}-n)L\right]exp\left\{i\Omega\left[t - \frac{L}{2c}(n_{pg}+n)\right]\right\}d\Omega \tag{4}$$

Assuming d_{eff} is independent of Ω, we can then simplify Eq. (4) to

$$E_{THz}(L,t) = -\frac{d_{eff}E_0^2L}{2cn_{pg}}\frac{\partial g^2[(t - n_{pg}L/c)/\tau]}{\partial t} \tag{5}$$

i.e. at each point the THz electric field is determined by the derivative of the pump intensity with respect to time regardless of what the pulse shape is. For the hyperbolic-secant pulses, the THz field is plotted vs. time in Fig. 1(b), i.e. a perfect single-cycle pulse. One can also obtain the conversion efficiency:

$$\eta = \frac{J_{THz}}{J_p} = \frac{2d_{eff}^2L^2\eta_0}{15c^2n_{pg}n_p^2\tau^3}\left(\frac{J_p}{A_p}\right) \tag{6}$$

where J_{THz} is the pulse energy density for the THz wave, J_p and A_p are the pulse energy and focal area of the pump beam, and η_0 is the vacuum impedance. The conversion efficiency and THz pulse energy are inversely proportional to the cubic power of the pump pulse width. Therefore, there is an obvious advantage of using short pump pulses. However, only when both the phase-

matching condition, Eq. (3), is satisfied and the phase-matching bandwidth is broad enough we can gain the huge enhancement due to the spatial accumulation, reflected by $J_{THz,\eta} \propto L^2$ in Eq. (6).

For the hyperbolic-secant pulses, the plane waves, and $k_p'' = 0$, one obtains

$$\widetilde{\mathcal{E}}(L,t) \approx \frac{E_0}{\cosh\!\left[\left(t - n_{pg}L/c\right)/\tau\right]} \exp\!\left\{-i\eta\left(\frac{15\omega_p\tau}{2}\right)\frac{\tanh\!\left[\left(t - n_{pg}L/c\right)/\tau\right]}{\cosh^2\!\left[\left(t - n_{pg}L/c\right)/\tau\right]}\right\} \tag{7}$$

The term inside the braces of Eq. (7) defines an effective nonlinear refractive index (n_2) due to the cascaded second-order parametric processes.
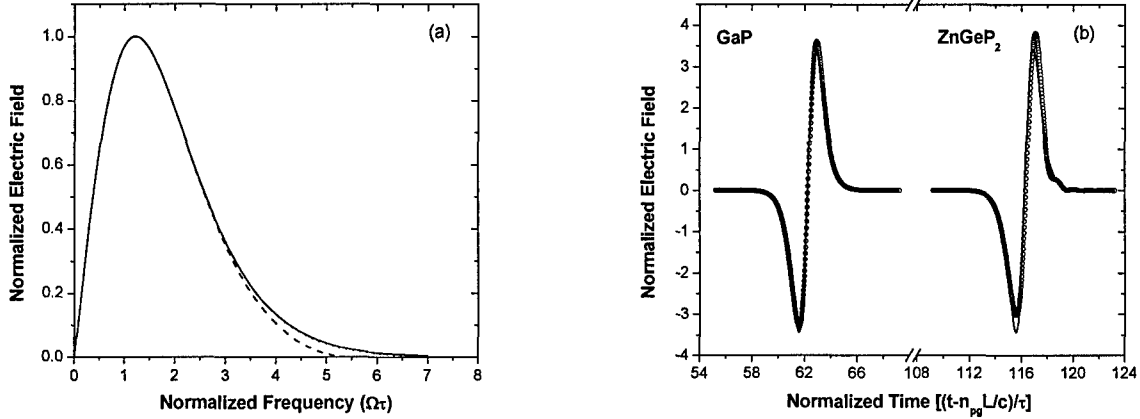

Fig. 1. (a) Solid curve: normalized spectral electric-field amplitude vs. normalized frequency for the ideal case. For comparison, normalized spectral electric-field amplitude is also plotted vs. normalized frequency for 2-mm-long GaP and ZnGeP$_2$ crystals at pump wavelengths of 1.034 μm and 1.218 μm, corresponding to dotted (almost coincides with the solid curve) and dashed curves, respectively. (b) Normalized instantaneous electric field vs. normalized time for the ideal case (two solid curves), a 2-mm-long GaP crystal (open circles), and a 2-mm-long ZnGeP$_2$ crystal (open circles) at pump wavelengths of 1.034 μm and 1.218 μm, respectively.

For a bulk GaP crystal, $\lambda_p \approx 1.031$ μm can be used to generate the central wavelength ~ 300 μm according to Eq. (3). The spectral bandwidth is then calculated to be between 170 μm and 366 μm. The optimum FWHM pulse width is $\tau_p \approx 2.149/\Omega_{THz} \approx 341$ fs. GaP has an advantage over other nonlinear crystals since its two-photon absorption (2PA) coefficient is negligible at 1.031 μm. By comparing the spectral and temporal profiles with those for the ideal case, see Fig. 1, one can see that the output THz pulses generated from a GaP crystal can be approximated by single cycles. Consider a peak pump power of 3.3 MW, $A_p \approx 0.22$ mm^2, and $L \approx 2$ mm. One can calculate the THz peak intensity to be about 3.4×10^5 W/cm^2 (peak power of 243 W) based on Eq. (6). Such an output power corresponds to a conversion efficiency of $8.9 \times 10^{-3}\%$. For such a conversion efficiency $n_2 \approx 5.0 \times 10^{-15}$ cm^2/W using Eq. (7). For the pumping condition considered above, the contributions due to GVD, 2PA, three-photon absorption (3PA), free-carrier absorption (FCA), and n_2 can be all neglected. For a bulk GaAs crystal with $\lambda_p \approx 1.328$ μm the central output wavelength is also ~ 300 μm. On the other hand, for a ZnGeP$_2$ crystal $\lambda_p \approx 1.218$ μm.

In order to find out the upper limits of the conversion efficiencies and output powers, we numerically solved Eqs. (1a) and (1b) for the plane waves. Consider $\lambda_p \approx 1.031$ μm in a 2-mm-long GaP crystal ($k_p'' = 1.3$ fs^2/μm). When the peak pump intensity is increased to 38 GW/cm^2,

the conversion efficiency reaches 0.23%, which approaches $\Delta\omega_p/\omega_p \approx 0.32\%$ where $\Delta\omega_p \approx 1.122/\tau$ is the pump bandwidth. There is only a slight saturation of the conversion efficiency at the high-intensity end. Moreover, the distortions of the THz temporal profiles due to the pump depletion are still negligible, see Fig. 2. The 3PA and corresponding FCA can be eliminated by using $\lambda_p \approx 1.339$ μm. In this case, one needs to use a channeled waveguide for the THz wave, resulting in the slight decrease of the index. As a result, it is possible for us to use the 2-mm-long GaP crystal for the efficient THz generation with the output peak power reaching 150 kW, corresponding to the peak intensity of 210 MW/cm^2.
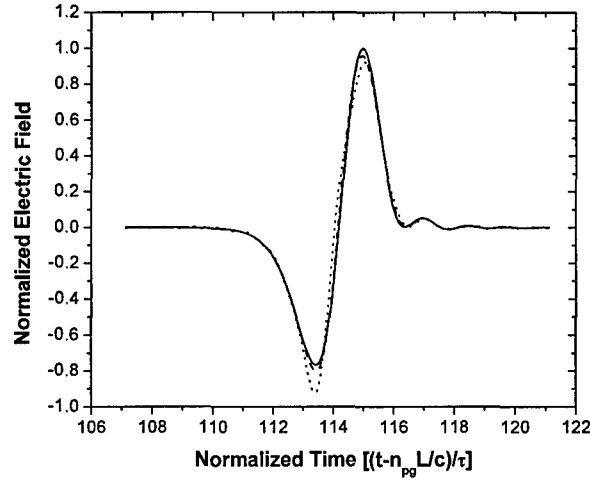

Fig. 2. For a 2-mm-long GaP crystal ($\lambda_p \approx 1.031$ μm and $k_p'' = 1.3$ fs$^2/\mu$m), normalized instantaneous electric field vs. normalized time for three different pump intensities: 1.5 GW/cm^2, solid curve; 14 GW/cm^2, dashed curve; and 38 GW/cm^2, dotted curve.

In summary, we have made a feasibility study for the efficient generation of quasi-single-cycle pulses by using broadband-phase-matched DFG among different frequency components within each pump pulse. We have shown that it is possible for us to achieve extremely high peak powers and peak intensities with high conversion efficiencies. These high-intensity THz pulses can be used to study nonlinear regimes of the interaction between short THz pulses and medium. At CLEO'06, Prof. Ted Norris' group confirmed some of our predicted results in a GaP crystal (CTuL2).

Our results were published in Opt. Lett. (2004) and IEEE J. Sel. Top. Quantum Electron. (2004).

1. D. Mittleman, "Terahertz imaging," in *Sensing with terahertz radiation*, Ed. D. Mittleman, Springer, NY (2003), pp. 117-153.
2. L. Xu, X.-C. Zhang, and D. H. Auston, Appl. Phys. Lett. **61**, 1784 (1992).
3. D. H. Auston, K. P. Cheung, and P. R. Smith, Appl. Phys. Lett. **45**, 284 (1984).
4. D. H. Auston, K. P. Cheung, J. A. Valdmanis, and D. A. Kleinman, Phys. Rev. Lett. **53**, 1555 (1984).
5. T. J. Carrig, G. Rodriguez, T. S. Clement, A. J. Taylor, and K. R. Stewart, Appl. Phys. Lett. **66**, 121 (1995).
6. A. Nahata, A. S. Weling, and T. F. Heinz, Appl. Phys. Lett. **69**, 2321 (1996).
7. Q. Wu, M. Litz, and X.-C. Zhang, Appl. Phys. Lett. **68**, 2924 (1996).
8. Y. J. Ding, Opt. Lett. **29**, 2650 (2004).
9. T. Yajima and K. Inoue, IEEE J. Quantum Electron. **5**, 140 (1969).

17. Backward parametric oscillation in second-order nonlinear medium

In a forward optical parametric oscillator (OPO), the pump, signal and idler beams all propagate in the same direction. If the idler beam propagates in the direction opposite to that for the pump beam, a backward OPO is also possible. For the frequency of the idler beam in the IR or mid-IR domain, such a process requires an anomalously large birefringence [1]. Besides such a stringent requirement the nonlinear crystal must be transparent in the wavelength range within which the output wave is produced. As a result, only a few nonlinear-optical crystals can satisfy these two conditions. Furthermore, a backward OPO has a threshold that is intrinsically much higher than that for a forward OPO. These are the underlying reasons why the backward OPO has not been achieved for the last four decades. In fact, even the backward difference-frequency generation (DFG) of the mid-IR wave has been only observed in $NaNO_2$ [2], to the best of our knowledge. A backward OPO has a major advantage over the forward one: Since the signal and idler waves counter-propagate in a nonlinear medium, an oscillation can occur without a mirror, whereas the forward OPO cannot oscillate without a cavity for the signal. Moreover, the linewidth for the backward OPO is much narrower than that for the forward OPO. Furthermore, due to severe temporal walk-off the backward OPO is efficient for long pump pulses. On the other hand, all nonlinear-optical crystals exhibit strong reststrahlen bands in the THz domain. Naturally on the low-frequency side of the reststrahlen bands, all the crystals become transparent. The THz domain may be one of the optimum regimes for achieving a backward THz parametric oscillation (TPO). Since the wave vector for the THz is much smaller compared with that for the mid-IR, the birefringence of the crystal does not have to be anomalously large. Instead, the birefringence can be used to minimize the threshold by properly selecting the parametric wavelengths. Recently, we observed a backward THz wave by mixing the two infrared laser beams in GaSe [3].

Here, we report our new result on scaling-up the output power by using a much longer GaSe crystal with the improved optical quality. Furthermore, following our theoretical analysis, we show that the backward parametric oscillation is achievable by using a GaSe or $ZnGeP_2$ crystal.

In order to achieve the backward DFG, we used two pump beams. The first one is the output of a Nd:YAG laser (1.064 μm) with a pulse duration of 10 ns, a pulse energy of 3 mJ, and a repetition rate of 10 Hz, whereas the second one is from a tunable β-BaB$_2$O$_4$-based OPO pumped by the 355-nm beam, with a duration of 5 ns, a pulse energy of 3.5 mJ, and a repetition rate of 10 Hz. In order to allow the two pump beams to pass through a parabolic mirror used to collimate the generated backward THz wave, a hole with the diameter of about 1.5 mm was drilled through it. The backward THz wave was then focused onto a Si bolometer by the second parabolic mirror. Last year, using a 7-mm-long GaSe crystal, we generated an output wave with a tuning range of 172.7–1417 μm (0.212–1.74 THz) and the output peak power of 35.7 W at 193 μm [3]. Recently, we acquired a 47-mm-long GaSe crystal with an aperture of 15 mm in diameter. To the best of our knowledge, this is the longest GaSe crystal ever grown. Using this new crystal, we were able to generate a backward wave with a tuning range of 167.6–2060 μm, see Fig. 1. The highest output power is about 217 W at the wavelength of 199.8 μm. Therefore, the tuning range has been greatly improved over our previous result. In addition, the peak power is about a factor of 6.1 higher than the previous value. Based on the two measured peak powers, the output power is scaled up linearly with the propagation length, which is typical for a Gaussian beam.
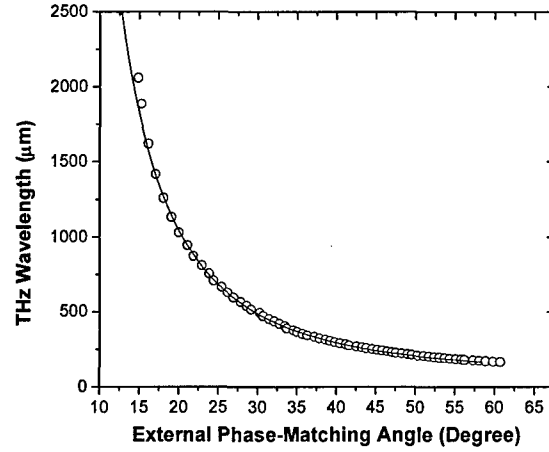
Fig. 1. The angle-tuning characteristics for the type-*eo-e* backward THz DFG in a GaSe crystal. The open circles correspond to our experimental results whereas the solid curve is produced based on the theoretical result obtained by using the phase-matching condition.

The type-*eo-e* backward DFG can be phase-matched in GaSe, where the 1.064-μm and OPO pump beams correspond to the extraordinary and ordinary waves inside the GaSe crystal (*eo*) whereas the generated THz beam is an extraordinary wave (*e*). For such a configuration, the phase-matching condition can be written as $k_p^{(e)} - k_i^{(o)} = -k_{THz}^{(e)}$, where $k_p^{(e)} = 2\pi n_p^{(e)} / \lambda_p$, $k_i^{(o)} = 2\pi n_i^{(o)} / \lambda_i$, and $k_{THz}^{(e)} = 2\pi n_{THz}^{(e)} / \lambda_{THz}$ are the wave vectors of the respective parametric waves with n's and λ's the indices of refraction and three parametric wavelengths: $\lambda_p < \lambda_i << \lambda_{THz}$, respectively. Based on the dispersion relations [4] and $\lambda_p^{-1} = \lambda_i^{-1} + \lambda_{THz}^{-1}$, we have plotted the tuning curve for the backward THz parametric processes in Fig. 1. Fig. 1 also shows the measured angle-tuning curve for the type-*eo-e* backward DFG. From Fig. 1, one can see that our experimental results are in an excellent agreement with our calculations. In order to verify that the above THz output is truly due to the backward parametric interaction, we measured the THz signal in the forward direction. A very weak THz signal was detected, which was just the THz wave generated from the non-phase-matched forward configuration.
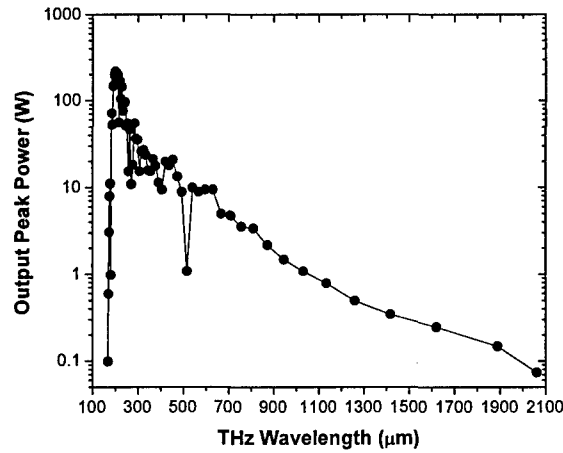

Fig. 2. The THz output peak power is measured vs. the output wavelength for the type *eo-e* phase-matched backward DFG in a GaSe crystal.

The backward output pulse energies were measured by using a Si bolometer calibrated by a pyroelectric detector. Fig. 2 illustrates the determined output peak power vs. the output wavelength for the type-*eo-e* backward DFG. A sudden drop of the output power at the short-wavelength side is due to the fact that there is a critical angle ($\approx$ 18° measured by us) above which the THz wave undergoes total internal reflection inside the GaSe crystal. The highest output peak power is measured to be 217 W at 199.8 μm, which corresponds to a conversion efficiency of 0.031% in terms of the powers from the OPO pump to the THz output. Neglecting the absorption for all three waves, based on Ref. [5] the output peak power can be determined by the following expression:

$$P_{THz} = \left(\frac{\pi^2}{4}\right)\left(\frac{\lambda_i}{\lambda_{THz}}\right)\frac{P_p P_i}{I_{th}\pi w_i^2} \tag{1}$$

where w_i is the beam radius for the OPO and P_p and P_i are the Nd:YAG and OPO peak powers, respectively. In Eq. (1), I_{th} is defined as the threshold intensity for achieving the backward OPO without considering the absorption of the three parametric waves, which is given by [1,5]:

$$I_{th} = \frac{\lambda_{THz}\lambda_i n_i^{(o)} n_{THz}^{(e)}(\theta) n_p^{(e)}(\theta)}{8\eta_0 d_{eff}^2 L^2} \tag{2}$$

Using Eq. (1), the highest output peak power is calculated to be 377 W, corresponding to the power conversion efficiency of 0.054%. These values are in good agreements with our measured ones.

The highest output power generated in our experiment can be dramatically scaled up. According to Eq. (1) with $I_p \approx I_i \approx I_{th} \approx 1.4\times10^8$ W/cm^2 at $\lambda_p \approx 2$ μm, the output peak power at $\lambda_{THz} \approx 450$ μm can be increased to 100 kW for a 5-cm-long GaSe crystal. Such a peak power can be focused down to produce a peak intensity of 67 MW/cm^2.

For each λ_p there is a critical angle, $\theta_{cr} = \theta_{PM} = sin^{-1}\left[1/n_{THz}^{(e)}(\theta_{PM})\right]$, where θ_{PM} is the phase-matching angle for the backward *eo-e* interaction, above which the total internal reflection for the generated THz wave takes place. Therefore, in Fig. 3 we have plotted the THz wavelength vs. the pump wavelength at such a critical condition. We have also plotted the corresponding threshold intensity vs. the pump wavelength in Fig. 3. For each pump wavelength, one can determine the threshold power: $P_{th} = I_{th}(\alpha)\pi w_p^2$, where w_p is the radius of the pump beam and $I_{th}(\alpha)$ is the threshold intensity in the presence of the absorption for the THz wave. For the optimum focusing, $\pi w_p^2 \approx L\lambda_{THz}/n_{THz}^{(e)}(\theta)$. As a result, one obtains each optimum output wavelength at which P_{th} reaches a minimum value, see Fig. 3. For example, at $\lambda_p \approx 1.86$ μm the optimum λ_{THz} is $\approx$ 211 μm for $L \approx 5$ cm. At $\lambda_p \approx 1.86$ μm one can completely eliminate three-photon absorption. The threshold intensity is calculated to be 116 MW/cm^2 for a 5-cm-long GaSe crystal at the critical output wavelength of 292 μm. This wavelength is quite close to the optimum value (i.e. 211 μm). When L is reduced to 1 cm, however, the threshold intensity is increased to 2.0 GW/cm^2. Such a threshold value is much below the damage threshold for this crystal. As the pump wavelength is increased, the critical THz wavelength linearly increases, see Fig. 3. At 10.6 μm it is increased to 1679 μm, see Fig. 3. This value is much longer than the optimum value (i.e. 403 μm). Consequently, the threshold intensity is significantly increased due to the wavelength scaling, as seen from Eq. (2). Indeed, for $L \approx 5$ cm the threshold intensity is calculated to 2.3 GW/cm^2. Based on Ref. [6], such a value is below the damage threshold for CO_2 laser pulses. Besides the GaSe crystal, $ZnGeP_2$ has the lowest absorption coefficients in the THz region. The

optimum performance corresponds to the *oe-o* interaction at $\lambda_p \approx 2.5$ μm. For $L \approx 5$ cm, we have calculated the threshold intensity to be ≈ 84 MW/cm^2 at $\lambda_{THz} \approx 422$ μm. This intensity is much lower than the damage threshold for a ZnGeP$_2$ crystal.
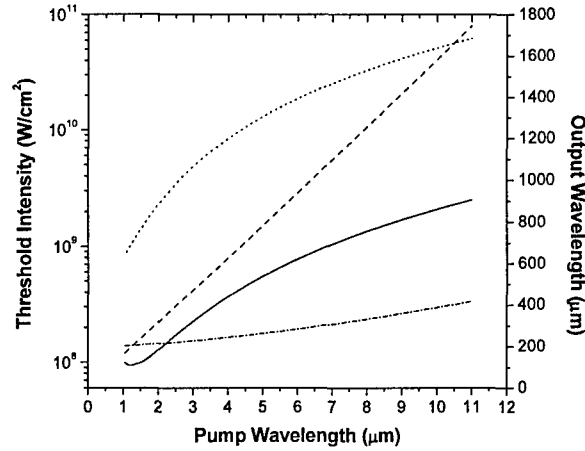

Fig. 3. When the phase-matching angle for the THz waves generated based on the backward TPO is equal to the total-internal-reflection angle, critical THz wavelength is plotted vs. pump wavelength (dashed curve). The corresponding threshold intensity is also plotted vs. pump wavelength for different lengths of a GaSe crystal: 1 cm (dotted curve) and 5 cm (solid curve). The dash-dotted curve corresponds to the optimum output wavelength at which the threshold power reaches a minimum value for each pump wavelength.

In summary, by using a 47-mm-long GaSe crystal, we efficiently generated a backward wave with a tuning range of 167.6-2060 μm. The highest output power is about 217 W at 199.8 μm. Compared with Ref. [3], the tuning range for the output has been greatly improved. In addition, the peak power is about a factor of 6.1 higher than our previous value. Such a peak power can be tightly focused to produce a peak intensity of about 700 kW/cm^2, which is sufficiently high to uncover a class of novel nonlinear effects in the THz domain. Based on our experimental results and calculations, we have found the optimized pumping conditions for achieving the backward parametric oscillation in the THz region and shown that such a process is indeed feasible in a GaSe or ZnGeP$_2$ crystal.

These results were published in Opt. Lett. (2005).

1. S.E. Harris, Appl. Phys. Lett. **9**, 114-116 (1966).
2. D. S. Chemla and E. Batifol, Opt. Commun. **11**, 57 (1974).
3. W. Shi and Y. J. Ding, IQEC 2004, Postdeadline Paper, IPDB6.
4. K. L. Vodopyanov and L. A. Kulevskii, Opt. Commun. **118**, 375 (1995).
5. Y. J. Ding and J. B. Khurgin, J. Opt. Soc. Am. B **15**, 1567 (1998).
6. G. B. Abdullaev, K. R. Allakhverdiev, M. E. Karasev, V. I. Konov, L. A. Kulevskii, N. B. Mustafaev, P. P. Pashinin, A. M. Prokhorov, Yu. M. Starodumov, and N. I. Chapliev, Sov. J. Quantum Electron. **19**, 494 (1989).

18. Observation of anomalously large band-filling effects in InAs/GaSb Type-II Superlattices: from 2-D to 3-D

It was predicted in 1981 that InAs/GaSb superlattices (SL's) exhibit wide minibands in the conduction band [1]. In the same year, a large miniband was confirmed in InAs/GaSb SL's [2]. It was demonstrated that InAs/GaSb SL's could be semimetallic [3] and be used for the detection of mid-infrared radiations [4]. InAs/GaSb SL's have peculiar band alignment: the bottom of the InAs conduction band is 143 meV below the top of the GaSb valence band. Therefore, electrons

and holes are always spatially separated (i.e. type II). Another inherent feature of this structure lies in the extremely light electron mass of InAs (0.026 m_0). Its de Broglie wavelength is so long that even for GaSb layer thickness in excess of 100 Å, there is considerable interaction between electrons in successive InAs layers, resulting in a substantially wide miniband [1]. Such a large width manifests the quasi-3D properties of the SL's. On the other hand, exciton banding energy is ≤ 1 meV. Therefore, exciton-related effects are negligible for most InAs/GaSb SL's. Due to these unique properties of the InAs/GaSb SL's intensive studies on these structures have been made recently. For example, negative luminescence was observed in InAs/GaSb SL photodiodes by extracting majority and minority carriers [5]. Recently, spectral blueshift and improved luminescence intensities with increasing GaSb layer thickness were also observed in InAs/GaSb SL's [6]. The InAs/GaSb SL's were used to implement a photovoltaic detector with a cut-off wavelength as long as 25 μm [7].

In this section, we report our results on detailed investigation of the InAs/GaSb SL's. For the first time, we have observed anomalously large band-filling effects. Moreover, we have systematically studied how the effects vary with the widths of the barrier and well layers from the 2-D quantum-well heterostructures to quasi-3D SL's.

Table 1. InAs/GaSb SL's used in our studies.
Letters h and l for K0291 and K0294 correspond to high and low defect densities, respectively.

Sample #	InAs Width (Å)	GaSb Width (Å)
K0202	24	100
K0203	24	75
K0204	24	50
K0205	24	25
K0288	22.5	100
K0290	40.3	100
K0291	45.2 (h)	100
K0294	45.2 (ℓ)	100

Before the deposition of the InAs/GaSb SL layers, a 5000-Å p-type GaSb buffer layer was grown on the top of the p-type GaSb (001) substrates in a MBE system. 50 periods of InAs/GaSb SL's were grown on the top of the buffer layer. A 300-Å-thick n-type InAs cap layer was then grown on the top of the SL's. The entire structure is effectively a pin photodiode structure. They are two series of the InAs/GaSb SL structures. In series #1, the width of the InAs well layer is always 24 Å while the width of the GaSb barrier layer changes from 100 Å (K0202), to 75 Å (K0203), 50 Å (K0204), and 25 Å (K0205). This series was designed to investigate the effects of the barrier width. In the second series, the barrier width is kept the same (100 Å) while the width of the well changes from 22.5 Å (K0288), to 40.3 Å (K0290), and to 45.2 Å (K0291 and K0294). The two samples having the same structure (K0291 and K0294) have high and low defect densities, respectively, see Table 1. Each of these eight samples was mounted on a cryostat with its temperature varying from liquid helium to room temperature. A CW Ti:Sapphire laser was used as a pump source with the output power up to 2 W and wavelength set to 7000 Å. An InSb detector and bolometer were used to measure the photoluminescence spectra after passing through a spectrometer.
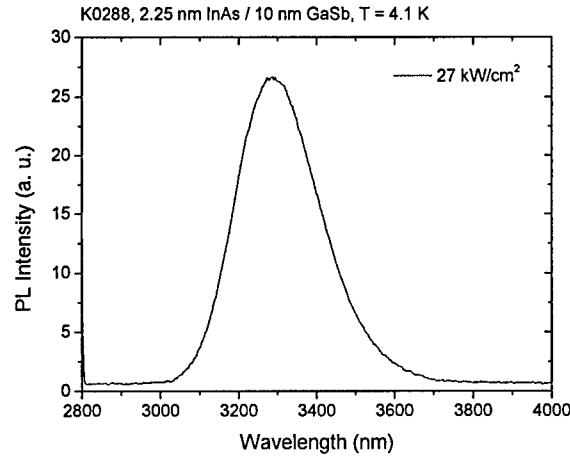
K0288, 2.25 nm InAs / 10 nm GaSb, T = 4.1 K

Fig. 1. Typical PL spectrum of type-II InAs/GaSb SL's.

Fig. 1 shows a typical PL spectrum measured by us for Sample K0288 at 4 K. For Series #1, as the barrier width is increased while the InAs well width is kept constant the PL peak is blueshifted. In addition, the linewidth is significantly decreased. Furthermore, the PL peak intensity is greatly enhanced. These results are consistent with the similar structures measured at 77 K [6]. As the barrier width is increased, the miniband width is significantly reduced. Therefore, the electrons behave as those closer to 2-D than 3-D in terms of the quantum confinement, which means that the electrons and holes are more separated in space. On the other hand, as the well width is increased while the barrier width is kept constant (Series #2) the PL peak is significantly redshifted. Such a shift is due to the reduction of the quantized energy for the electrons inside the InAs well. For all the structures in Series #2, the minibands are negligible.

K0202: 2.4 nm InAs/ 10 nm GaSb, T=4.3 K
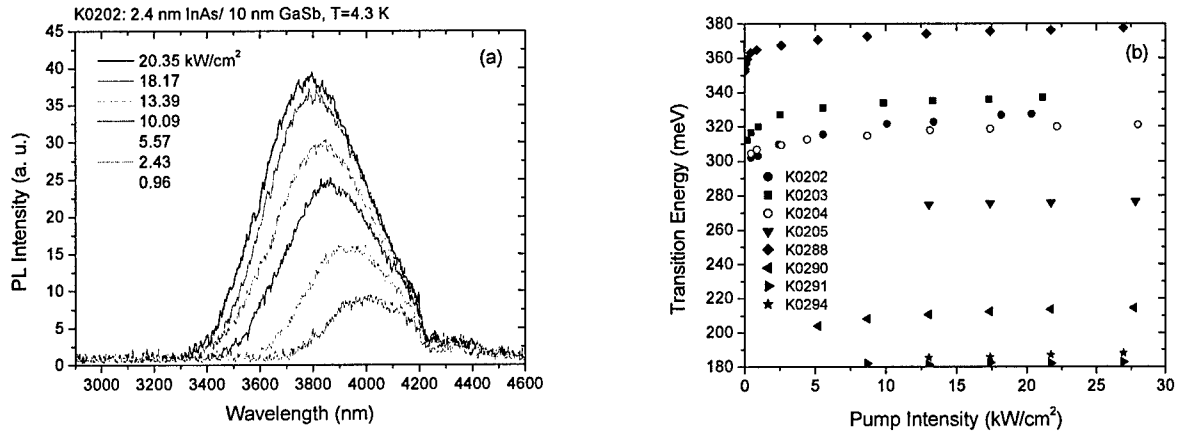
Fig. 2. (a) PL spectra are measured for different pump intensities at 4.3 K. (b) Transition energy vs. pump intensity for all eight structures based on the measurements of PL spectra at different pump intensities.

As the pump intensity is increased, we have observed strong band-filling effects for Samples K0202, K0203, and K0288, see Fig. 2(a). Therefore, in Fig. 2(b) we have plotted the transition energy vs. pump intensity for all eight samples. As one can see, the sample K0202 (2.4 nm InAs/10 nm GaSb) exhibits the strongest band-filling effect with the transition energy shift

by an amount of 25.4 meV from 435 W/cm^2 to 20.4 kW/cm^2. On the contrary for Sample K0205 (2.4 nm InAs/2.5 nm GaSb) the band-filling effect is the weakest with the transition-energy shift of 1.82 meV for the pump intensity increase from 13 kW/cm^2 to 27.8 kW/cm^2 whereas for a similar intensity range the shift for K0202 is about 5.73 meV. We believe that for K0202 the electrons are more or less confined inside the InAs wells (2-D). As a result, the density of states is independent of the electron energy. Compared with the GaAs/AlAs type-II SL's the density of states for the InAs/GaSb type-II SL's is a factor of 2.58 lower. Therefore, the band-filling effect is enhanced in K0202. On the other hand, for K0205 the electron wave function spreads over many periods of the InAs/GaSb type-II SL's. Such a structure has a wide miniband (about 190 meV) [1]. In such a case, the electrons behave just like those in the quasi-3D. Therefore, the density of states increases as the electron energy is increased (close to a parabolic dependence). In this case, the band-filling effect is reduced compared with K0202. However, compared with a bulk GaAs crystal, the density of states is reduced by a factor of 4.14 for the same electron energy. This means that even for K0205 the band-filling effect is quite strong. A detailed examination of the behaviors for all the eight samples reveals that there are the severe saturation of the energy shifts. As a matter of fact, the saturation for the shift is stronger than a parabolic dependence.
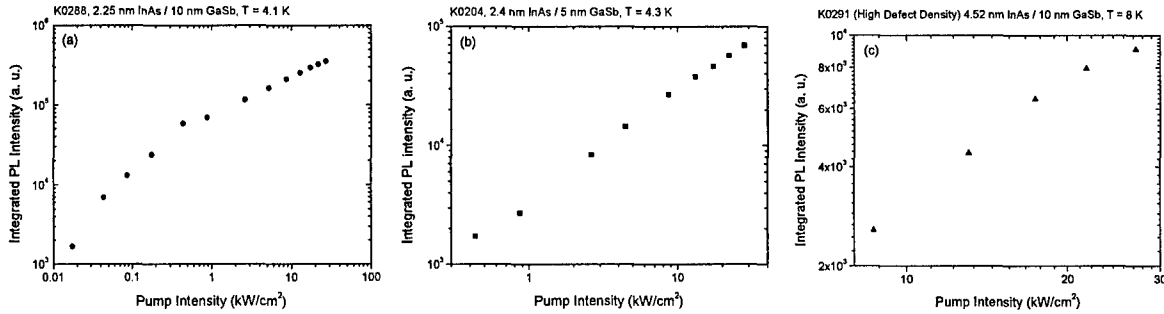

Fig. 3. Wavelength-integrated PL intensity is plotted vs. pump intensity for three different structures: (a) K0288, (b) K0204, and (c) K0291.

By investigating the dependence of the wavelength-integrated PL intensity vs. pump intensity, we have found out whether the nonradiative recombination is present. Fig. 3 shows the dependences of the integrated PL intensity on pump intensity for three samples: K0288, K0204, and K0291. One can see that for K0288 the dependence is linear at low pump intensities. However, for the high pump intensities, the dependence becomes sub-linear. On the other hand, for K0204 the sub-linear dependence is less obvious. Indeed, only the pump intensity is higher than 10 kW/cm^2 the dependence is slightly sub-linear. We believe these sub-linear dependences are due to Auger recombination at the high carrier densities, giving rise to the power index of 2/3 $\approx$ 0.67. Based on our result, we conclude that the Auger recombination rate dramatically increases as the transition energy is increased. This can be explained by the fact that for K0204 the overlap between the electron and hole wave functions is increased compared with that for K0288. As a result, the radiative recombination is enhanced for K0204, which means that the Auger recombination is less important. For K0291, due to the present of high-density defects, the nonraditive recombination becomes more important. If the nonraditive recombination at the interface and barrier traps is dominant, the dependence becomes a perfect square. One can see that the dependence is between square and linear. In comparison, the dependence of the integrated PL intensity on the pump intensity is more or less linear for K0294.

In summary, we have studied optical properties of InAs/GaSb type-II SL's for different well and barrier widths at different temperatures and/or pump intensities. We have observed an anomalously large blue shift of the transition energy in the amount as large as 25.4 meV for the 2.4 nm InAs/10 nm GaSb structure as the pump intensity is increased. However, when the coupling for the electrons among the different InAs wells becomes strong, the blue shift caused by band-filling effect is greatly reduced. We believe the enhanced band-filling effects are due to the extremely light electron mass of InAs. We have also demonstrated that by measuring the dependence of the wavelength-integrated PL intensity on pump intensity we can find out whether the nonradiative recombination for the electrons at the interface and barrier traps and the Auger recombination are present. Our results define the linear response range for mid-IR detectors and output powers for mid-IR emitters.

These results were presented at CLEO/QELS (2005).

1. G. Bastard, Phys. Rev. B **24**, 5693-5697 (1981).
2. P. Voisin, G. Bastard, C. E. T. Gonçalvès da Silva, M. Voos, L. L. Change, and L. Esaki, Sol. Stat. Commun. **39**, 79-82 (1981).
3. L. L. Chang, N. J. Kawai, E. E. Mendez, C.-A. Chang, and L. Esaki, Appl. Phys. Lett. **38**, 30-32 (1981).
4. M. J. Yang and B. R. Bennett, Electron. Lett. **30**, 1710-1711 (1994).
5. L. J. Olafsen, I. Vurgaftman, W. W. Bewley, C. L. Felix, E. H. Aifer, J. R. Meyer, J. R. Waterman, and W. Mason, Appl. Phys. Lett. **74**, 2681-2683 (1999).
6. A. P. Ongstad, R. Kaspi, C. E. Moeller, M. L. Tilton, D. M. Gianardi, J. R. Chavez, and G. C. Dente, J. Appl. Phys. **89**, 2185-2188 (2001).
7. Y. Wei, A. Gin, M. Razeghi, and G. J. Brown, Appl. Phys. Lett. **81**, 3675-3677 (2002).

19. Novel Approach to Efficient UV Emitters by Frequency-Doubling in Nitrides-Based Structures from Laser Diode

UV emitters have potential applications in lighting, display, and fluorescence studies. For example, they can be used as excitation sources in biosensors. Indeed, 260-280 nm excitation wavelengths with 300-400 nm emissions can used to detect micro-organisms, pollens, pollen allergens, fungal spores, organic pollutants whereas 340-360 nm excitations with 400-550 nm emissions can be used to monitor reduced nicotinamide adenine dinucleotide (NADH) in micro-organisms [1]. In the past, UV sources have been developed based on different schemes such as all-solid-state frequency converters and Argon ion lasers. Although these sources have high coherence, they are bulky, having short lifetimes, and having low conversion efficiencies. On the other hand, nitride-based semiconductor laser diodes emitting at 340 nm or shorter have not been achieved so far. Since these devices could be compact and driven by current, they are the ultimate UV emitters. An alternative approach is to combine a visible semiconductor UV laser diode with a frequency doubler made from nitrides-based multilayers. Such a UV emitter would have the same advantages as those nitrides-based coherent emitters which have not been implemented yet.

Here, we propose a novel approach to the coherent UV emitters. We take advantages of the semiconductor lasers in the visible region and large nonlinearities of the AlGaN layers. Moreover, we propose to use vertical and horizontal cavities to enhance the conversion efficiencies from the visible radiation of a laser diode to the UV beam. Our novel approach is built upon some recent work on nitrides-based vertical cavity surface-emitting lasers (VCSEL) [2], AlGaN/AlN Bragg reflectors [3], and second-order nonlinearities for GaN and AlGaN [4]. Using our approach, it is feasible to achieve the coherent emission at the wavelength as short as 240 nm for studying the Raman effects in bioagents.
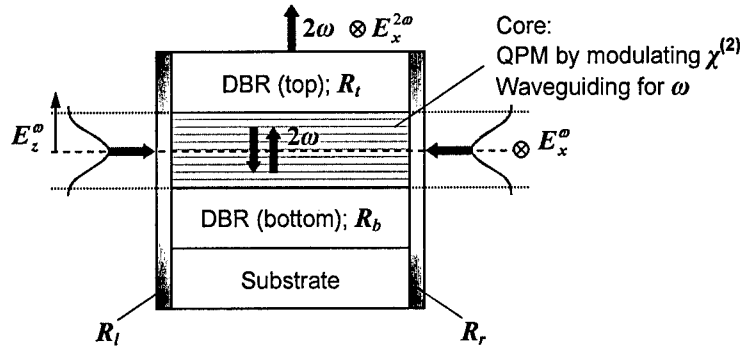
Fig. 1. A doubler used for the coherent UV generation from a visible laser beam and wave-propagation configuration. The TE and TM modes at the pump wavelength can be coupled by the two quarter-wave plates incorporated into the horizontal cavity.

Consider a structure for a frequency doubler, shown in Fig. 1. An edge-emitting laser diode in the visible range is used as a pump beam. The radiation from the laser diode resonates with the horizontal cavity formed by a pair of the mirrors, R_l and R_r. The visible radiation inside the horizontal cavity interacts with the alternating layers of $Al_xGa_{1-x}N/Al_yGa_{1-y}N$ ($x \neq y$) through the second-optical susceptibilities. As a result, the second-harmonic (i.e. UV) radiation is generated with its propagation direction parallel to the vertical (growth) axis. This UV beam is bounced back and forth between two vertical mirrors, R_t and R_b. We choose the two vertical mirrors in such a way that their effective indices of refraction are lower than that for the $Al_xGa_{1-x}N/Al_yGa_{1-y}N$ alternating layers used for doubling. As a result, the two fundamental beams counter-propagate as the guided modes in a waveguide. In order to achieve high conversion efficiencies, the scheme of quasi-phase-matching must be used, which can be achieved by using alternating $Al_xGa_{1-x}N/Al_yGa_{1-y}N$ layers. This is due to the fact that the second-order nonlinear coefficient for the $Al_xGa_{1-x}N$ layer depends on the aluminum concentration. The lower is the aluminum concentration the higher is the nonlinear coefficient. As a result, the second-order nonlinear coefficient can be spatially modulated by using alternating $Al_xGa_{1-x}N/Al_yGa_{1-y}N$ layers. The spatially modulated nonlinear coefficient compensates the spatial modulation of the standing-wave second-harmonic field inside the vertical cavity. The optimum thickness for each $Al_xGa_{1-x}N$ layer is given by $\lambda_{UV}/2n_{UV}$, where λ_{UV} and n_{UV} are the wavelength and refractive index for the UV beam, respectively. It is worth noting that the conversion efficiency is proportional to the spatial overlap among the spatially-modulated second-order nonlinear coefficient, the mode profiles for the two counter-propagating beams, and spatial component of the UV electric field, see below. As a result, we must add an extra layer next to the $Al_xGa_{1-x}N/Al_yGa_{1-y}N$ alternating layers such that the spatial overlap is maximized. The thickness of this extra layer is $\lambda_{UV}/4n_{UV}$.

According to Ref. [5], the conversion efficiency for the structure shown in Fig. 1 can be determined by the following equation:

$$\eta = \frac{2R_r}{1+R_r}[1-exp(-a)][1-R_lR_r\,exp(-a)] \tag{1}$$

where the parameter a is related to the normalized pump power ($\tilde{P}=P/P_s$, where P is the pump power and P_s is the saturation power) by

$$\tilde{P} = \frac{a[1-R_lR_r\,exp(-a)]}{1+R_r\,exp(-a)} \tag{2}$$

with the saturation power given by

$$P_s = \frac{\lambda^2 n^2 n_{UV}\left(1 - R_t R_b\right) w t_{eff}}{8\pi^2 \eta_0 (\Delta d)^2 L t} \tag{3}$$

where λ is the wavelength of the diode laser, n is the refractive index at λ, w, t, and L are the width, thickness, and length of the slab waveguide within which the two fundamental beams counter-propagate, and t_{eff} is the spatial overlap (in the unit of length) among the spatially-modulated second-order nonlinear coefficient, the mode profiles for the two counter-propagating beams, and spatial component of the UV electric field.
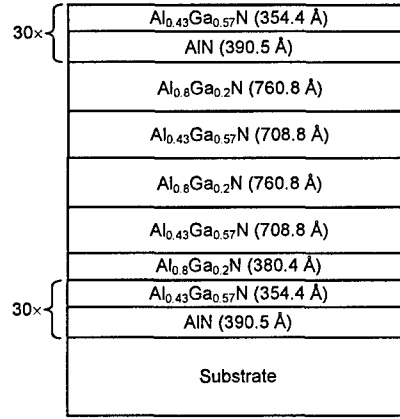

Fig. 2. An optimized structure for the coherent generation of the 340-nm radiation from a visible laser diode at 680 nm.

Obviously, the lower is the saturation power the more efficient is the frequency doubler. According to Eq. (3), P_s depends on the mirror reflectivities R_t and R_b. Let us consider the generation of the 340-nm UV beam from the 680-nm laser diode. Based on Ref. [3], the reflectivity as high as 99% at 340 nm can be achieved by using 30 pairs of $Al_{0.43}Ga_{0.57}N$ and AlN alternating layers. Using the dispersion relations obtained in Ref. [6], the thicknesses of these layers are calculated to be 354.4 Å and 390.5 Å, respectively. These values are quite close to those used in Ref. [3]. On the other hand, the alternating $Al_{0.43}Ga_{0.57}N$ and $Al_{0.8}Ga_{0.2}N$ can be used as a nonlinear medium for frequency doubling. The thicknesses of these layers are calculated to be 708.8 Å and 760.8 Å, respectively. In order to achieve strong waveguide confinement, 2 pairs of the alternating $Al_{0.43}Ga_{0.57}N/Al_{0.8}Ga_{0.2}N$ layers and an extra 380.4-Å-thick $Al_{0.8}Ga_{0.2}N$ layer are sufficient. The optimized structure is shown in Fig. 2. For the proposed surface-emitting geometry, the second-order optical susceptibility element d_{xzx} provides the nonlinear coefficient for frequency doubling. This coefficient requires that the two pump and UV beams have the polarizations parallel to z, x, and x, respectively, see Fig. 1. According to Ref. [4], the difference between the nonlinear coefficients of the $Al_{0.43}Ga_{0.57}N$ and $Al_{0.8}Ga_{0.2}N$ layers is calculated to be $\Delta d_{xzx} \approx 3.7$ pm/V. First, assuming that the reflectivities for the two horizontal mirrors based on the dielectric multilayers achieved by film evaporation are 99%, $w \approx 100$ μm, $L \approx 1$ cm, and $t_{eff}/t \approx 10$, we can estimate the pump power to be 50 mW for the conversion efficiency of 10%. Therefore, the output power at 340 nm is about 5 mW. For the second case, we assume $R_l \approx 0.14$ (Fresnel reflection), $R_r \approx 0.99$, $w \approx 25$ μm, and $L \approx 1$ cm. For the conversion efficiency of 10%, the output peak power is estimated to be 24 W for the pump power of 237 W. In this case, the pump beam is pulsed. For an average pump power of 237 mW,

the output power is about 24 mW. Although 340-nm emission was achieved from a nitride-based LED pumped by a fast pulsed current injection (subnanosecond time scale) with an output power of 1 mW [7], the linewidth was quite broad. In addition, the injection current was quite high. In comparison, our UV output has a linewidth which is a half of that for the pump laser. In addition, our nitride layers are not doped. Therefore, current injection is only required for the visible diode lasers.

It is possible for us to further improve the performance of the doubler. First of all, we can replace the $Al_{0.43}Ga_{0.57}N$ and $Al_{0.8}Ga_{0.2}N$ alternating layers by $Al_{0.8}Ga_{0.2}N$/GaN asymmetric-coupled quantum wells. They can lead to the reduction of the saturation power given in Eq. (3) by two orders of magnitude. According to Ref. [8], there exists a strong built-in field in these quantum-well structures, which can be used to further increase the effective nonlinear coefficient. Second, the channeled waveguide for the fundamental beams can reduce the saturation power by one order of magnitude. Third, the reflectivities of the vertical cavity can be increased to 99.9% by using dielectric multilayers via film evaporation to decrease the saturation power by one order of magnitude.

Our UV emitter can be implemented by a monolithic integration of a doubler with an edge-emitting laser. It is expected that the performance of our UV emitter is comparable with a regular semiconductor laser diode in the visible range in terms of current injection, size, power consumption, and lifetime. Moreover, the output wavelength from our UV emitter can be as short as 240 nm for investigating the Raman effects in bioagents.

In summary, we have made a feasibility study for the efficient generation of coherent UV radiation. Such a novel approach is made possible by taking advantage of edge-emitting lasers in the visible region and large second-order nonlinearities for the AlGaN layers. It is feasible for us to integrate an edge-emitting laser with a frequency doubler to implement a monolithic UV emitter driven by current injection. The output wavelength for our coherent UV emitter can be as short as 240 nm. The main advantage for this novel approach lies in the fact that p-type and n-type doping in the AlGaN layers can be avoided. As a result of this work, a simplified structure based on the AlGaN multilayers was recently grown. It will be characterized in July.

These results were presented at CLEO/QELS (2005).

1. A. P. Snyder, W. M. Maswadeh, A. Tripathi, J. Eversole, J. Ho, and M. Spence, Anal. Chim. Act. **513**, 365-377 (2004).
2. J. M. Redwing, D. A. S. Loeber, N. G. Anderson, M. A. Tischler, and J. S. Flynn, Appl. Phys. Lett. **69**, 1 (1996).
3. A. Bhattacharyya, S. Iyer, E. Iliopoulos, A. V. Sampath, J. Cabalu, T. D. Moustakas, and I. Friel, J. Vac. Sci. Technol. B **20**, 1229-1233 (2002).
4. T. Fujita, T. Hasegawa, M. Haraguchi, T. Okamoto, M. Fukui, and S. Nakamura, Jpn. J. Appl. Phys. **39**, 2610-2613 (2000); V. I. Gavrilenko and R. Q. Wu, Phys. Rev. B **61**, 2632-2642 (2000).
5. Y. J. Ding, J. B. Khurgin, and S.-J. Lee, J. Opt. Soc. Am. B **12**, 1586-1594 (1995).
6. Ü. Özgür, G. Webb-Wood, H. O. Everitt, F. Yun, and H. Morkoç, Appl. Phys. Lett. **79**, 4103-4105 (2001).
7. H. Peng, E. Makarona, Y. He, Y.-K. Song, A. V. Nurmikko, J. Su, Z. Ren, M. Gherasimova, S.-R. Jeon, G. Cui, and J. Han, Appl. Phys. Lett. **85**, 1436-1438 (2004).
8. G. Vaschenko, D. Patel, and C. S. Menoni, H. M. Ng, and A. Y. Cho, Appl. Phys. Lett. **80**, 4211-4213 (2002).

20. Extremely-wide, high-power, and coherent THz and microwave radiations by mixing two near-infrared frequencies in a 47-mm-long GaSe crystal

Tunable monochromatic microwave radiations have potential applications in high-resolution spectroscopy such as the identification of chemicals and proteins and DNA, active and passive imaging through atmosphere, and free-space communications. This electromagnetic

spectrum range has an attractive advantage over THz waves for imaging and communications through atmosphere. Indeed, the attenuation at 100 GHz in the atmosphere is 1dB/km whereas it is about 100,000 dB/km near the peaks of water lines around 1THz [1]. In the microwave region, the main absorption is originated from the two water lines at 22 GHz and 183 GHz as well as the 321 GHz and 325 GHz lines [2], and the peaks from O_2 in the range of 50-60 GHz [3]. There are several methods for the generation of coherent microwaves such as photoconductively-switched antennas and rectifications. However, these techniques can be used only to produce broadband pulses. Optical mixing in semiconductor optoelectronic and electronic devices such as photodiodes, MESFETs, HEMTs, HBTs, and Schottky diodes can be also used to generate the tunable outputs up to 100 GHz. All other sources such as klystrons and backward-wave oscillators are either bulky or they have rather short lifetimes.

In this section, by mixing two optical frequencies in a GaSe crystal based on the process of phase-matched difference-frequency generation, we have produced a monochromatic microwave radiation continuously tunable in a large range. As mentioned below, the output power can be dramatically scaled up by using a $ZnGeP_2$ waveguide and/or a cavity. This new technique can provide coherent links between optical and microwave frequency standards. Based on difference-frequency generation in the longest GaSe crystal to date, we were able to tune the output wavelength from 66.5 μm (150 cm^{-1}) to 5664 μm (1.77 cm^{-1}). Such a tuning range is the widest ever produced for a continuously-tunable and coherent tabletop THz source. In addition, the peak output power has reached 389 W. Such a record-high power corresponds to a conversion efficiency of ~ 0.1%. This conversion efficiency is also the highest ever achieved for a tabletop system. In this brief report, however, we will primarily focus on the microwave or millimeter region for our output.

In our experiment, the two mixing beams used for the microwave generation are the Nd:YAG beam at 1.0642 μm and the idler beam from a master oscillator/power oscillator (MOPO) pumped by a frequency-tripled Nd:YAG laser beam (with its wavelength tunable in the range of 1.0642-1.0653 μm). The Nd:YAG laser pulses have a duration of 10 ns and a repetition rate of 10 Hz. The Nd:YAG pump intensity used in our experiment is ~17 MW/cm^2 and idler pump energy is 3.5-4.5 mJ/pulse. The generated output signals were detected by a bolometer, which were then amplified and averaged in a boxcar integrator.

GaSe is a negative uniaxial crystal having a point group of $\bar{6}2m$. It has the lowest absorption coefficient in the microwave region among all the inorganic nonlinear crystals [4]. Furthermore, it has a large second-order nonlinear coefficient. However, GaSe has a layered structure. Since the forces between layers are of the weak van der Waals type, each layer can be sequentially peeled off from a GaSe crystal by using a scotch tape. Therefore, the input and output facets are always normal to the optic axis.

For the efficient conversion from the two optical waves to the microwave wave, two conditions must be satisfied, i.e. the conservations of the total photon energy and the total momentum (i.e. phase matching). The first condition is satisfied if the output frequency is the difference of the two optical frequencies. However, the second one requires that the nonlinear-optical crystal has a sufficiently large amount of the birefringence. In the other words, for a given amount of the birefringence for a crystal and crystal orientation only a particular output frequency may simultaneously satisfy these two conditions. The polarization for the microwave is the same as the second-order nonlinear polarization generated by mixing the two pump beams. By using a 47-mm-thick GaSe crystal, we have generated the coherent radiation continuously tunable from 1 mm to 5.66 mm (53-300 GHz) based on type-*oe-e* phase-matched DFG (see Fig.

1). In order to achieve phase-matching, the 1.0642-µm pump beam and idler beam from the MOPO system are ordinary and extraordinary waves (designated by *o* and *e*) whereas the microwave is an extraordinary wave (denoted by *e*). The solid curves correspond to the calculation made by using the phase-matched conditions and dispersion relations for GaSe [5]. The pump and output wavelengths have been verified by an infrared spectrometer and a scanning THz etalon consisting of a pair of the parallel Ge plates, respectively. The output wavelengths are consistent with those calculated from difference-frequency generation. One can see from Fig. 1 that the obtained output wavelengths cover a wide range.
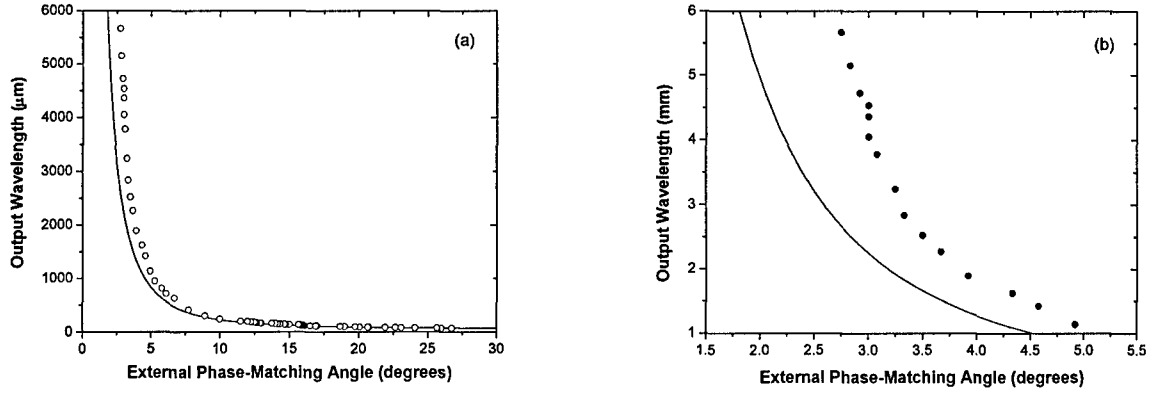
Fig. 1. Output wavelength vs. external phase-matching angle for the type-*oe-e* phase-matched interaction in (a) the entire tuning range and (b) the microwave or millimeter region.

Besides the tuning ranges, the output peak powers are also important for many applications, especially communications and imaging through the atmosphere. The generated output beams had pulse duration of 5 ns and a repetition rate of 10 Hz. Their pulse energies were measured by a calibrated bolometer. As a result, the peak output powers were determined, see Fig. 2. The highest output peak power is measured to be 4.7 W at the wavelength of 1 mm (300 GHz), see Fig. 2, corresponding to the conversion efficiency of 0.0012%.
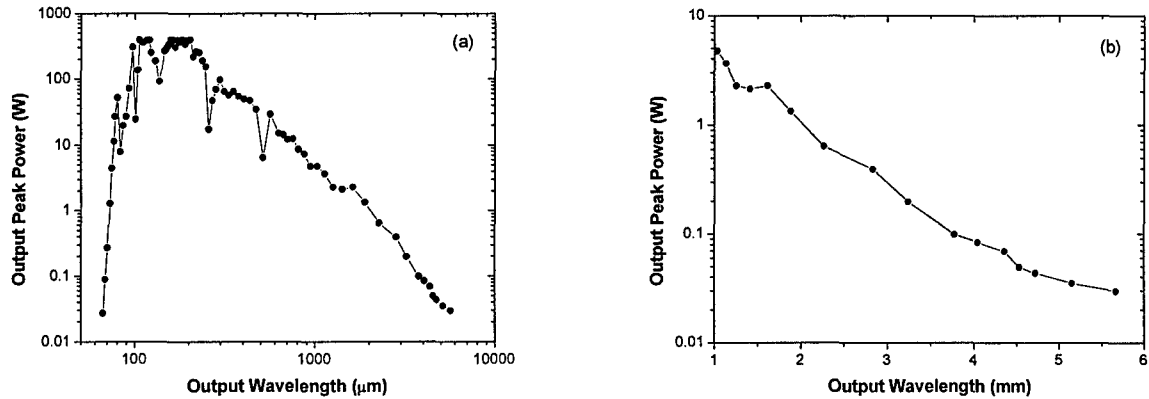
Fig. 2. Output peak power vs. output wavelength for phase-matched difference-frequency generation within (a) the entire tuning range and (b) the microwave or millimeter region.

Since the wavelengths for the microwave are much longer than the pump wavelengths, it is important for us to analyze the effect of the wavelength fluctuation on the output power. Assume

that the phase-mismatch is π/2 (the microwave power drops to 81% of the phase-matched value) due to the deviation of the frequency for the MOPO beam (idler), which is given by

$$\Delta v_i = \frac{c}{4L\left[n_{mm}^{(o)} - n_i^{(o)}\right]} \tag{1}$$

where $n_{mm}^{(o)}$ and $n_i^{(o)}$ are the indices of refraction for the ordinary microwave and idler beam, respectively, and L is the length of the nonlinear medium. For the MOPO wavelength of $\lambda_i \approx$ 1.0652 μm (the microwave wavelength of 1.134 mm) and $L \approx$ 4.7 cm, $\Delta v_i \approx$ 3.473 GHz (0.1158 cm⁻¹). On the other hand, the fluctuation of the incident angle for the pump beams can also decrease the microwave power. Assume again that the phase-mismatch is π/2 due to the deviation of the incident angle from the phase-matched value ($\theta_{ext}^{(PM)}$). One can find the expression for the angle deviation:

$$\Delta\theta_{ext} = \frac{\lambda_i n_i^{(o)} \left[n_i^{(e)}\right]^2}{4L\left\{\left[n_i^{(o)}\right]^2 - \left[n_i^{(e)}\right]^2\right\}\theta_{ext}^{(PM)}} \tag{2}$$

For $\lambda_i \approx$ 1.0652 μm, $\theta_{ext}^{(PM)} \approx 4.92°$. Based on Eq. (2), $\Delta\theta_{ext}$ is estimated to be 0.035°. Obviously, the diffraction angle for the idler beam must be larger than this value. However, in order to achieve the optimum conversion efficiency, the confocal beam parameter for the microwave should be about the half of the crystal length. Therefore, the diffraction for the MOPO beam should be

$$\theta_{diff} \approx \sqrt{\frac{\lambda_i^2 n_{mm}^{(o)}}{\pi\lambda_{mm}\left[n_i^{(o)}\right]^2 L}} \tag{3}$$

For $\lambda_i \approx$ 1.0652 μm and $L \approx$ 4.7 cm, we have determined $\theta_{diff} \approx$ 0.003044°. We can then estimate the beam radius for the MOPO to be 2.283 mm. All these important issues must be taken into consideration in order to optimize the conversion efficiency.

From the calculations made above, one can see that the beam diameter for the pump beams must be sufficiently large in order to achieve the optimum conversion in a bulk crystal. In order to further improve the conversion efficiency for the microwave generation, we must use a channel waveguide to strongly confine the microwaves. Since the wavelengths for the optical beams are much shorter than those of the microwave, the microwave waveguide has almost no confinement effect on the optical waves. However, due to the inherent softness of a GaSe crystal, we cannot process this crystal into a waveguide structure. Therefore, we need to search for an alternative material. Recently, we efficiently generated the coherent radiation tunable in the frequency range of 183 GHz-3.61 THz in a ZnGeP₂ crystal [6]. Unlike the GaSe crystal, this crystal can be easily fabricated into a waveguide to confine the microwaves. According to our calculations, the output peak power can be increased to 160 W at the output wavelength of 1 mm (300 GHz), for a pump power of 100 kW at ~ 3.1 μm (the conversion efficiency of 0.16%). Such a high conversion efficiency can be achieved by using a microwave waveguide and/or intracavity frequency mixing. The pump beams can be produced by down-converting a fiber-laser beam at 1.55 μm in a second-order nonlinear crystal such as periodically-poled $KTiOPO_4$ or $LiNbO_3$. Therefore, it is conceivable for us to construct a compact microwave emitter pumped by an erbium-doped fiber laser system. By modulating the erbium-doped fiber laser, one can transfer the signal carried by a fiber laser to the microwave antenna. If one uses an electro-optic traveling modulator built from a ZnGeP₂ crystal, the signal carried by a microwave antenna in the

frequency range from 53 GHz to 300 GHz can be readily converted back to the optical signal at 1.55 μm,. The main advantages for using GaSe and $ZnGeP_2$ crystals are the low absorption coefficients in the microwave region and large nonlinear (electro-optic) coefficients.

Coherent microwaves tunable continuously in the wide frequency range from 53 GHz to 300 GHz has been achieved by using the phase-matched DFG in a 47-mm-long GaSe crystal. The highest peak power achieved so far is measured to be 4.7 W at 1 mm (300 GHz). We can dramatically scale up the output power by confining the microwaves by a waveguide as well as by utilizing the scheme of intracavity frequency mixing. We have discussed how the fluctuations of the pump frequency and incident angle and the diffraction angle affect the microwave power. We have also discussed the possibility of constructing novel and compact systems for converting the optical signals at 1.55 μm to the microwaves and back to the optical signals. Such systems can provide coherent links between optical and microwave frequency standards.

These results were published in Intern. J. High Speed Electron Sys. (2006) and J. Nonlinear Opt. Phys. & Mats. (2006).

1. F. C. De Lucia, Opt. Photon. News **Aug**. 45-50, 2003.
2. F. C. De Lucia, P. Helminger, R. L. Cook, and W. Gordy, Phys. Rev. A **5**, 487 (1972).
3. R. W. Zimmerer and M. Mizushima, Phys. Rev. **121**, 152 (1961).
4. E. D. Palik, *Handbook of optical constants of solids III*, Academic, NY (1998), pp. 487 & 640.
5. K. L. Vodopyanov and L. A. Kulevskii, Opt. Commun. **118**, 375 (1995).
6. W. Shi, Y. J. Ding, and P. G. Schunemann, "Coherent terahertz waves based on difference-frequency generation in an annealed zinc-germanium phosphide crystal: Improvements on tuning ranges and peak powers," Opt. Commun. **233**, 183-189 (2004).

Since projects #21-23 listed in the section of Status of effort had been co-supported by the new AFOSR grant (FA9550-05-1-0480), the results obtained on these projects will be included in the progress reports on the new grant.

Personnel Supported

Yujie J. Ding
Wei Shi
Xiaodong Mu
Hongqian Sun
Roman S. Dubinkin

Publications

Refereed Journal Articles

1. Y. J. Ding and W. Shi, "Progress on widely-tunable monochromatic THz sources and room-temperature detections of THz waves," J. Nonlinear Opt. Phys. & Mats. vol. 15, no. 1, pp. 89-111 (2006).

2. Y. J. Ding and W. Shi, "Widely-tunable monochromatic THz sources based on phase-matched difference-frequency generation in nonlinear-optical crystals: A novel approach," Laser Phys. 2006, vol. 16, no. 4, pp. 562-570.

3. W. Shi and Y. J. Ding, "Tunable coherent radiation from terahertz to microwave by mixing two infrared frequencies in a 47-mm-long GaSe crystal," to appear in Intern. J. High Speed Electron. Sys. Mar./Apr. 2006 issue.

4. X. Mu, Y. J. Ding, Z. Wang, and G. J. Salamo, "Quantum-well dots based on InGaAs/GaAs quantum well strained by InAs quantum dots," Laser Phys. Lett. 1-6 (2005)/DOI 10.1002/lapl.200510037; vol. 2, no. 11, pp. 538-543 (2005).

5. W. Shi and Y. J. Ding, "Generation of backward THz waves in GaSe crystals," Opt. Lett., vol. 30, pp. 1861-1863, Jul. 15, 2005.

6. W. Shi and Y. J. Ding, "Tunable terahertz waves generated by mixing two copropagating infrared beams in GaP," Opt. Lett., vol. 30, 1030-1032, May 1, 2005; Virtual Journal of Ultrafast Science May 2005, Vol. 4, Issue 5 (Sources).

7. X. Mu, Y. J. Ding, Z. Wang, and G. J. Salamo, "Evidence of strong phonon-assisted resonant intervalley up-transfer for electrons in type-II GaAs/AlAs superlattices," IEEE J. Quantum Electron., vol. 41, pp. 337-343, Mar. 2005.

8. Y. J. Ding, "Quasi-Single-Cycle THz Pulses Based on Broadband-Phase-Matched Difference-Frequency Generation in Second-Order Nonlinear Medium: High Output Powers and Conversion Efficiencies," IEEE J. Sel. Top. Quantum Electron., vol. 10, pp. 1171-1179, Sep./Oct. 2004.

9. Y. J. Ding, "Efficient Generation of High-Power Quasi-Single-Cycle THz Pulses from Single Infrared Beam in Second-Order Nonlinear Medium," Opt. Lett., vol. 29, pp. 2650-2652, Nov. 15, 2004.

10. W. Shi and Y. J. Ding, "Chemical identification based on direct measurement of absorption spectrum by frequency-tuning monochromatic THz source," Laser Phys. Lett., vol. 1, no. 11, pp. 560-564 (2004).

11. W. Shi and Y. J. Ding, "A monochromatic and high-power THz source tunable in the ranges of 2.7-38.4 μm and 58.2-3540 μm for variety of potential applications," Appl. Phys. Lett., vol. 84, pp. 1635-1637, Mar. 8, 2004; Virtual Journal of Biological Physics Research-March 15, 2004, Vol. 7, Issue 6 (Instrumentation Development).

12. W. Shi, Y. J. Ding, and P. G. Schunemann, "Coherent terahertz waves based on difference-frequency generation in an annealed zinc-germanium phosphide crystal: Improvements on tuning ranges and peak powers," Opt. Commun., vol. 233, pp. 183-189, 2004.

13. W. Shi and Y. J. Ding, "Continuously-tunable and coherent terahertz radiation by means of phase-matched difference-frequency generation in zinc germanium phosphide," Appl. Phys. Lett., vol. 83, pp. 848-850, Aug. 4, 2003.

14. Y. J. Ding and W. Shi, "Widely-tunable, monochromatic, and high-power terahertz sources and their applications," J. Nonlinear Opt. Phys. & Mats. 12(4), pp. 557-585, Dec. 2003.

15. W. Shi and Y. J. Ding, "Designs of THz waveguides for efficient parametric THz generation," Appl. Phys. Lett., vol. 82, pp. 4435-4437, Jun. 23, 2003.

16. W. Shi and Y. J. Ding, "Coherent and widely-tunable THz and millimeter waves based on difference-frequency generation in GaSe and $ZnGeP_2$," Optics in 2002, Optics and Photonics News, Dec. 2002, p. 57.

17. X. Mu, Y. J. Ding, H. Yang, and G. J. Salamo, "Vertically stacking self-assembled quantum wires," Appl. Phys. Lett., vol. 81, pp. 1107-1109, Aug. 5, 2002.

18. W. Shi, Y. J. Ding, N. Fernelius, and K. L. Vodopyanov, "An efficient, tunable, and coherent 0.18–5.27 THz source based on GaSe crystal," Opt. Lett., vol. 27, pp. 1454-1456, Aug. 15, 2002.

Conference Proceedings
1. Y. J. Ding and W. Shi, "Widely-tunable monochromatic THz sources based on phase matched difference-frequency generation in nonlinear-optical crystals: A novel approach," Proceedings of LPHYS'05, Laser Phys. 2006.

2. Y. J. Ding and W. Shi, "Widely-Tunable Monochromatic Sources and Novel Detection Scheme for THz Imaging," in Technologies for Optical Countermeasures II; Femtosecond Phenomena II; and Passive Millimetre-Wave and Terahertz Imaging II, edited by D. H. Titterton, S. M. Kirkpatrick, R. Stoian, R. Appleby, J. M. Chamberlain, K. A. Krapels, Proceedings of SPIE Vol. 5989 (SPIE, Bellingham, WA, 2005) 59891B-1-10.

3. H. Sun, W. Shi, Z. Fu, and Y. J. Ding, and Y. B. Zotova, "Bragg reflectors and 2-D photonic crystals in the THz region," in *Terahertz for Military and Security Applications III*, edited by R. Jennifer Hwu, Dwight L. Woolard, Mark J. Rosker, Proceedings of SPIE Vol. 5790 (SPIE, Bellingham, WA, 2005) 104-115.

4. Y. J. Ding, "Investigation of limits on peak powers and conversion efficiencies for quasi-single-cycle THz pulses based on phase-matched difference-frequency generation," in *Terahertz and Gigahertz Electronics and Photonics IV*, edited by R. Jennifer Hwu, Kurt J. Linden, Proceeding of SPIE Vol. 5727 (SPIE, Bellingham, WA, 2005) 32-43.

5. X. Mu and Y. J. Ding, Z. Wang and G. J. Salamo, and J. Little, "InAs Quantum Dots Coupled with Strained InGaAs/GaAs Coupled Quantum-Wells," Proceedings of SPIE Photonic West'05, Conference on "Quantum Dots, Nanoparticles, and Nanoclusters II", San Jose, CA, Jan. 22-27, 2005, Paper 5734-5.

6. W. Shi and Y. J. Ding, "Identification of chemicals in the vapor phase by directly measuring absorption spectra through frequency-tuning a monochromatic THz source," SPIE Proceedings of Chemical and Biological Standoff Detection II, Optics East 2004, Philadelphia, PA, Paper 5584-2.

7. X. Mu, Y. J. Ding, Z. Wang, and G. J. Salamo, "Phonon-assisted up-transfer for electrons in type-II GaAs/AlAs superlattices," Proceedings of LPHYS'04, Laser Phys., vol. 15, no. 2, pp. 225-232 (2005).

8. X. Mu, Y. J. Ding, Z. Wang, and G. J. Salamo, "Evidence of strong phonon-assisted resonant intervalley up-transfer for electrons in type-II GaAs/AlAs superlattices," Proceedings of SPIE Vol. 5352 (2004).

9. Y. J. Ding, "THz oscillators based on bulk GaAs crystal", *Ultrafast phenomena in semiconductors VI*, Kong Thon Tsen, Jin-Joo Song, and Hongxing Jian, Editors, Proceedings of SPIE Vol. 4643 (2002).

10. X. Mu and Y. J. Ding, J. B. Khurgin, X. Wang, J. Zhang and F. Choa, "Design, growth, and characterization of GaAs/AlAs type-II superlattices", *Quantum Dot Sources and Detectors*, James A. Lott, Nikolai N. Ledentsov, and Kevin J. Malloy, Editors, Proceedings of SPIE Vol. 4656 (2002).

11. X. Mu, Y. J. Ding, I. B. Zotova, H. Yang, and G. J. Salamo "Growth and characterization of single and stacked InP/InAs/InP quantum wires", *Quantum Dot Sources and Detectors*, James A. Lott, Nikolai N. Ledentsov, and Kevin J. Malloy, Editors, Proceedings of SPIE Vol. 4656 (2002).

Interactions/Transitions

1. **(Refereed)** H. Sun and Y. J. Ding, "Transmission spectra of diatomic and triatomic molecules at high pressures in the mid-infrared and THz regions," Laser Applications to

Chemical, Security, and Environmental Analysis Meeting, LACSEA 2006, Incline Village, NV, Feb. 5-9, 2006.

2. **(Invited)** Y. J. Ding, "A novel scheme for THz detection at room temperature," SPIE Photonics West'06, Conference on "Terahertz and Gigahertz Electronics and Photonics V", San Jose, CA, Jan. 21-26, 2006.

3. **(Invited)** Y. J. Ding, "Backward parametric interactions," SPIE Photonics West'06, Conference on "Nonlinear Frequency Generation and Conversion: Materials, Devices, and Applications V", San Jose, CA, Jan. 21-26, 2006.

4. X. Mu, Y. J. Ding, and J. Little, "Investigation of anomalously large band-filling effect in type-II InAs/GaSb superlattices," SPIE Photonics West'06, Conference on "Physics and Simulation of Optoelectronic Devices XIV", San Jose, CA, Jan. 21-26, 2006.

5. **(Refereed)** Y. J. Ding and W. Shi, "Novel approaches to THz sources and detectors at room temperature for imaging," Opt. Solutions for Homeland & National Security, Hyatt Regency Washington DC, Dec. 15-16, 2005.

6. **(Refereed)** Y. J. Ding and W. Shi, "An efficient THz source with a tuning range of 71.1–2830 μm (0.106–4.22 THz) based on frequency mixing in a GaP crystal," 2005 Intern. Semi. Dev. Res. Symp., ISDRS, Holiday Inn Select, Bethesda, MD, Dec. 7-9, 2005.

7. **(Invited)** Y. J. Ding, "Widely-tunable, monochromatic, and high-power THz sources," Symposium on Infrared Materials and Technologies, Nov. 21/22, 2005, Penn State Univ.

8. **(Invited)** Y. J. Ding, "Novel approaches to THz sources and detectors at room temperature," LEOS 2005, Paper WN1, Oct. 23-27, 2005, Hilton Sydney, Australia.

9. **(Refereed)** H. Sun, W. Shi, Y. J. Ding, and Y. B. Zotova, "Investigation of Bragg Reflectors and 2-D Photonic Crystals in THz Domain," LEOS 2005, Paper TuI2, Oct. 23-27, 2005, Hilton Sydney, Australia.

10. W. Shi and Y. J. Ding, "Widely-tunable monochromatic sources and novel detection scheme for THz imaging," SPIE Europe Symp. Optics/Photon. Security & Defence, Conference of Passive millimeter-wave and terahertz imaging and technology II, Bruges, Belgium, Sep. 26-29, 2005, Paper 5989C-49.

11. **(Invited)** Y. J. Ding, "Novel approaches to high-power THz sources from single cycles to monochromatic waves," LPHYS'05, Kyoto, Japan, July 4-8, 2005.

12. **(Invited)** Y. J. Ding, "Progress on widely-tunable monochromatic THz sources and room-temperature detections of THz waves," 7th Mediterranean Workshop and Topical Meeting, "Novel Optical Materials and Applications", NOMA, May 29-June 4, 2005, Cetraro, Italy.

13. **(Refereed)** W. Shi and Y. J. Ding, "Backward parametric oscillation in second-order nonlinear medium," QTuF7, CLEO/QELS, May 22-27, 2005, Baltimore, MD.

14. **(Refereed)** W. Shi and Y. J. Ding, "Fingerprinting molecules based on direct measurement of absorption spectrum by frequency-tuning monochromatic THz source," CTuGG6, CLEO/QELS, May 22-27, 2005, Baltimore, MD.

15. **(Refereed)** X. Mu, Y. J. Ding, and J. Little, "Observation of anomalously large band-filling effects in InAs/GaSb type-II superlattices: from 2-D to 3-D," CFE1, CLEO/QELS, May 22-27, 2005, Baltimore, MD.

16. **(Refereed)** Y. J. Ding, "Generation of quasi-single-cycle THz pulses based on broadband-phase-matched difference frequency generation: high conversion efficiencies and output powers," CWM2, CLEO/QELS, May 22-27, 2005, Baltimore, MD.

17. **(Refereed)** W. Shi, Y. J. Ding, N. Fernelius, and F. K. Hopkins, "A novel detection scheme for THz waves based on upconversion at room temperature," CWM5, CLEO/QELS, May 22-27, 2005, Baltimore, MD.

18. **(Refereed)** W. Shi and Y. J. Ding, "Tunable coherent microwave radiation by mixing two optical frequencies in a 47-mm-long GaSe crystal," JWB7, CLEO/QELS, May 22-27, 2005, Baltimore, MD.

19. **(Refereed)** Y. J. Ding, "Novel approach to efficient UV emitters by frequency-doubling in nitride-based structures from laser diodes," JWB71, CLEO/QELS, May 22-27, 2005, Baltimore, MD.

20. H. Sun, F. Zhan, W. Shi, Y. J. Ding, and Y. B. Zotova, "1D and 2D photonic bandgap crystals in the THz domain," Terahertz for military and security applications III, SPIE Defense and security symposium, Orlando, FL, Mar. 28 – Apr. 1, 2005, 5790-12.

21. **(Invited)** Y. J. Ding, "Pushing limits on THz sources from single cycles to monochromatic waves," SPIE Photonics West'05, Conference on "Ultrafast Phenomena in Semiconductors and Nanostructure Materials IX", San Jose, CA, Jan. 22-27, 2005, 5725-6.

22. Y. J. Ding, "Investigation of limits on peak powers and conversion efficiencies for quasi-single-cycle THz pulses based on phase-matched difference-frequency generation," SPIE Photonics West'05, Conference on "Terahertz and Gigahertz Electronics and Photonics IV", San Jose, CA, Jan. 22-27, 2005, 5727-7.

23. X. Mu and Y. J. Ding, Z. Wang and G. J. Salamo, and J. Little, "InAs Quantum Dots Coupled with Strained InGaAs/GaAs Coupled Quantum-Wells," SPIE Photonics West'05, Conference on "Quantum Dots, Nanoparticles, and Nanoclusters II", San Jose, CA, Jan. 22-27, 2005, 5734-5.

24. **(Invited)** Y. J. Ding and W. Shi, "Backward THz parametric oscillator without cavity," WOFE 2004, Wyndham Aruba Beach Resort, Aruba, Dec. 18-22, 2004.

25. **(Refereed)** Y. J. Ding, "Efficient Generation of High-Power Single-Cycle THz Pulses from Single Optical Beam in Second-Order Nonlinear Medium," LEOS Ann. Meet. 2004, Nov. 7-11, Puerto Rico.

26. W. Shi and Y. J. Ding, "Identification of chemicals in the vapor phase by directly measuring absorption spectra through frequency-tuning a monochromatic THz source," OpticsEast 2004, Philadelphia, PA, Paper 5584-2.

27. **(Refereed)** W. Shi and Y. J. Ding, "Observation of strong backward THz wave by mixing two infrared laser beams in GaSe," IQEC 2004, May 16-21, San Francisco, CA, Postdeadline Paper IPDB6.

28. **(Refereed)** W. Shi and Y. J. Ding, "Observation of efficient THz generation with a tuning range of 84–1134 μm based on quasi-phase-matched difference-frequency generation in a cubic crystal," CLEO 2004, May 16-21, San Francisco, CA, Session CMI5.

29. **(Refereed)** R. S. Dubinkin, X. Mu, and Y. J. Ding, "Spectrum of two-photon absorption coefficients for $ZnGeP_2$," IQEC 2004, May 16-21, San Francisco, CA, Session IMD6.

30. **(Refereed)** X. Mu and Y. J. Ding, Z. Wang, and G. J. Salamo, "Observation of stimulated emission in short-period quasi-indirect type-II GaAs/AlAs superlattices," CLEO 2004, May 16-21, San Francisco, CA, Session CFM4.

31. **(Refereed)** H. Sun, W. Shi, and Y. J. Ding, "Design, Fabrication, and Characterization of THz Bragg Reflectors," CLEO 2004, May 16-21, San Francisco, CA, Session CThAA2.

32. **(Refereed)** W. Shi and Y. J. Ding, "Direct measurement of resonant frequencies for H_2O in the range of 0.2-4.2 THz by frequency-tuning monochromatic THz source," CLEO 2004, May 16-21, San Francisco, CA, Session CMG2.

33. **(Refereed)** X. Mu, Y. J. Ding, Z. Wang, G. J. Salamo, and J. Little, "Coupling between InAs Quantum Dots and Strained InGaAs/GaAs Coupled Quantum-Wells: A Novel Type of Quantum Dots," IQEC 2004, May 16-21, San Francisco, CA, Session IWA35.

34. **(Refereed)** W. Shi and Y. J. Ding, "Determination of resonant frequencies for DNA and protein by directly measuring absorption spectra," CLEO 2004, May 16-21, San Francisco, CA, Session CThDD.

35. **(Invited)** Y. J. Ding, X. Mu, Z. Wang, and G. J. Salamo, "Phonon-assisted up-transfer of electrons in type-II superlattices," LPHYS'04, Trieste, Italy, July 12-16, 2004.

36. W. Shi and Y. J. Ding, "Chemical identification using widely-tunable monochromatic THz sources," Terahertz for Military and Security Applications II, International Symposium on Defense and Security, Apr. 12-16, 2004, Orlando, FL.

37. **(Refereed)** W. Shi and Y. J. Ding, "Chemical identification based on absorption spectroscopy by using widely-tunable monochromatic THz source," LACEA 2004, Annapolis, MD, Feb. 9-11, 2004.

38. **(Refereed)** R. Song, W. Shi, and Y. J. Ding, "THz absorption of DNA's and proteins by using widely-tunable monochromatic THz source," LEOS 2003 Ann. Meet., Oct. 26-30, 2003, Tucson, AZ.

39. **(Refereed)** H. Sun, W. Shi, and Y. J. Ding, "Design and characterization of THz photonic bandgap crystals," LEOS 2003 Ann. Meet., Oct. 26-30, 2003, Tucson, AZ.

40. **(Invited)** Y. J. Ding, "Observation of strong phonon-assisted resonant intervalley up-transfer for electrons in type-II GaAs/AlAs superlattices," Ultrafast Phenomena in Semiconductors and Nanostructure Materials VIII (OE05), SPIE's International Symposium on Integrated Optoelectronic Devices 2004, Jan. 26-29, 2004, San Jose, CA.

41. W. Shi and Y. J. Ding, "Efficient generation of coherent and widely-tunable THz and millimeter waves by using GaSe and $ZnGeP_2$ crystals," Terahertz for Military and Security Applications, AeroSense, SPIE, Apr. 21-15, 2003, Orland, FL.

42. **(Invited)** Y. J. Ding, "Investigation of type-II superlattices for efficient amplification of radiation," LEOS 2003 Ann. Meet., Oct. 26-30, 2003, Tucson, AZ.

43. **(Invited)** Y. J. Ding, "Efficient generation of tunable and coherent THz waves based on parametric processes," 12th Intern. Laser Phys. Workshop, LPHYS'2003, Aug. 25-29, 2003, Hamburg, Germany.

44. **(Invited)** Y. J. Ding, "Coherent, efficient, and widely-tunable THz sources," 6th Mediterranean workshop and topical meeting, "Novel optical materials and applications", Jun. 8 – 13, 2003, Cetraro, Italy.

45. **(Invited)** Y. J. Ding and W. Shi, "Coherent THz waves based on difference-frequency generation," CLEO/PR'03.

46. **(Refereed)** I. B. Zotova and Y. J. Ding, "Spectral two-photon absorption in the range of 1.3 – 1.75 μm for GaAs," CLEO'03.

47. **(Refereed)** W. Shi and Y. J. Ding, "THz waveguides for efficient THz parametric conversion," CLEO'03.

48. **(Refereed)** W. Shi and Y. J. Ding, and N. Fernelius "Improvement on tuning ranges and output powers of THz waves based difference-frequency generation in GaSe," CLEO'03.

49. **(Refereed)** W. Shi, Y. J. Ding, and P. G. Schunemann, "Tunable and coherent THz source using $ZnGeP_2$," CLEO'03.

50. **(Refereed)** X. Mu, Y. J. Ding, Z. Wang, and G. J. Salamo, "Formation of InGaAs/GaAs quantum-well dots by using self-assembled InAs quantum dots as stressors," CLEO'03.

51. **(Refereed)** X. Mu, Y. J. Ding, Z. Wang, G. J. Salamo, and J. B. Khurgin, "Resonant phonon-assisted electron intervalley up-transfer in type-II GaAs/AlAs superlattices," CLEO'03.

52. **(Invited)** Y. J. Ding, "Efficient generation of coherent and tunable THz waves," CLEO'03.

53. **(Refereed)** W. Shi and Y. J. Ding, "Coherent mid-IR wave tunable in the range of 15–28 µm in CdSe," Adv. Solid-State Photon., Feb. 2-5, 2003, San Antonio, TX, Paper MC5.

54. **(Invited)** Y. J. Ding, "Efficient laser amplifiers based on quasi-indirect-bandgap GaAs/AlAs nanostructures," Nanoscience and nano-optics, 33rd Winter Colloquium on the Physics of Quantum Electronics, Jan. 5-9, 2003, Snowbird, UT.

55. **(Refereed)** W. Shi, X. Mu, and Y. J. Ding, and N. Fernelius, "Coherent radiation tunable in the range of 2.7–29 µm based on phase-matched difference-frequency generation in GaSe," 5th Intern. Conf. Mid-IR Optoelectron. Materials and Devices, Sep. 8-11, 2002, Annapolis, MD.

56. I. B. Zotova, X. Mu, and Y. J. Ding, "Spectrum of two-photon absorption coefficient for GaAs," OSA Ann. Meet. 2002.

- Session chair for Nano & molecular nonlinear optics and Raman & fiber lasers at LEOS'05, 18th Ann. Meet.

- Session chair for Second Harmonic Generation, CLEO'05; Harmonic Generation and Down-Conversion, QELS'05

- Session chair for Ultrafast Lasers, Ultrafast Phenomena in Semiconductors and Nanostructures Materials IX, Photonics West 2005 (Jan. 24th)

- Session chair for Nonlinear Optics in Fibers, LEOS Ann. Meet. 2004

- Session chair for LPHYS 2004.

- Session chair for 2003 CLEO/QELS.

- Session chair for 2002 CLEO/QELS (2 sessions).

- Session chair for 2001 OSA Ann. Meet.

- Topical Editor for J. Opt. Soc. Am. B. (2001-05).

- Member of The American Physical Society and The Optical Society of America.

- Field Reviewer for NRL Postdoctoral Fellowship Application Review (ASEE), Aug. 2005

- Referee for Phys. Rev. Lett.; Opt. Lett.; Appl. Phys. Lett.; Phys. Rev.;
- J. Appl. Phys.; IEEE J. Quantum Electron.; IEEE Photon. Tech. Lett.;
- Optics Express; Appl. Opt.; J. Nonl. Opt. Phys. & Mats.; J. Mod. Opt.

- Member of Subcommittees for Solid-State Lasers for LEOS 2005.

- Member of Subcommittee for Applications of Nonlinear Optics, CLEO 2005 & 2006.

- Member of Subcommittees for Nonlinear Optics and Solid-State Lasers for LEOS 2004.

- Member of QELS 2002 Program Committee for Nonlinear Optics.

- Member of program committee for SPIE Photonic West '99, '00, '01, '02, '03, '04, '05, and '06 Int. Sym. on "Ultrafast Phenomena in Semiconductors III, IV, V, VI, and VII", and "Ultrafast Phenomena in Semiconductors and Nanostructure Materials VIII (OE05), IX, X, and XI (OE04)".

- NSF Panelist (2003-05).

- Panelist for Electronics, Optoelectronics, and Data Storage of PA Nanotechnology 2002, Oct. 4, 2002.

New discoveries, inventions, or patent disclosures
- None.

Honors/Awards

- Recipient for Class of 1961 Professorship, 2003-2005 Academic Years, Lehigh University.
- Senior member of IEEE.